Università degli studi di Padova

**Dipartimento di Fisica e Astronomia "Galileo Galilei"**

**Corso di Laurea Magistrale in Fisica**


**Tesi di Laurea Magistrale**

# Heavy Stable Charged Particles at LHC with the CMS detector: search and results for a trigger implementation


Laureando: Giovanni Mocellin, matricola 1123103

*Università degli studi di Padova, Padua, Italy*

Relatore: Prof. Anna Teresa Meneguzzo

*Università degli studi di Padova & INFN sez. Padova, Via Marzolo 8, Padova, Italy*

Correlatore: Dott. Luigi Guiducci

*Università degli studi di Bologna & INFN sez. Bologna, Viale Berti Pichat, 6/2, Bologna, Italy*



Anno Accademico 2016/2017

# Contents

# List of Figures

# List of Tables

# Introduction

In 2011 and 2012, the Large Hadron Collider produced proton-proton interactions at a center of mass energy of 7 and 8 $TeV$ and the CMS experiment collected an integrated luminosity of $\sim 5$ e $\sim 20$ $fb^{-1}$ respectively for the two energies; these data allowed to verify for the first time the existence of the boson expected from the Higgs theory and to perform many analysis to search for physic beyond the Standard Model. LHC restarted in 2015 at a center of mass energy of 13 $TeV$ and with an increased luminosity; the new data allowed to verify the properties of the new boson, to test with high precision the expectations for the Standard Model processes, even the very rare ones and to improve the searches for new physics. In the next years, in order to increase the statistics, and improve the sensibility to low cross-sections processes, the instantaneous luminosity of LHC will be increased to reach the values of $5 \times 10^{34}$ $cm^{-2}s^{-1}$ in the High-Luminosity LHC project, beginning in 2025. With a final integrated luminosity of 3000 $fb^{-1}$, a factor $10\times$ with respect to the dose for which the detectors of the LHC experiments were built, the longevity and the performance of the subdetectors have to be verified.

This thesis is related to the search of Long Lived Particles (LLP) and specifically of Heavy Stable Charged Particles (HSCP) as a signature of new physics. The two main characteristics of HSCP are a high ionization and a large time of flight with respect to Standard Model particles.

In the 2012 data taking, it was possible to implement a specific trigger for the search for massive particles with the CMS detector. It identified candidates crossing the entire detector with velocities lower than the speed of light, taking a time of flight up to 50 $ns$ larger than muons, since the inter-bunch time was 50 $ns$, allowing no overlaps with the following proton-proton produced standard model particles. No signal was identified but new lower mass limits for these particles were set.

Starting from 2015, the LHC interaction frequency was doubled, reducing the time between two following bunch crossings to 25 $ns$, and the specific HSCP trigger used up to 2012 could not be employed any more.

In the thesis the aspects related to the new 40 $MHz$ frequency and to the foreseen integrated luminosity have been considered regarding two aspects of the HSCP searches: from one side defining, developing and testing online on proton-proton interactions a possible specific trigger for HSCP particles and, on the other hand, studying the current performance and the expected aging effects of the Drift Tubes chambers, part of the muon system detector. The information of the Drift Tubes chambers are indeed used both by the muon trigger and by the muon and HSCP track measurements. Their performance on next years of LHC and HL-LHC will be crucial for the CMS physics searches.

In chapter 1, the theoretical motivations and the searches for the HSCP are discussed.

In chapter 2, the structure and the principles of function of LHC and the CMS detector are presented.

In chapter 3, the HSCP searches and the measurements of the properties performed with the CMS detector are explained.

In chapter 4, possible optimizations of the Level 1 Muon Trigger for slow-moving particles are described and the obtained results from the simulations are shown.

In chapter 5, the firmware simulation and the final hardware implementation of the 2BX trigger algorithm are presented.

In chapter 6, the conclusions on the 2BX trigger implementations and the future perspectives on the trigger are reported.

In chapter 7, the aging studies are described for the muon DT chambers and the bicells.

# Chapter 1

# Theoretical motivations for HSCP

Since the discovery of nucleus in 1911 by Ernest Rutherford, many studies and experiments have been done to find out the structure of the matter which composes and surrounds us. In 1932 James Chadwick demonstrated that the foreseen neutral particles in the nuclei could be found with energetic alpha particles produced in polonium decay directed on light element targets. During the same decades, studying the cosmic rays, it was found that the primary rays were made of energetic known particles, such as protons and helium nuclei, but secondary ones contained also different unstable particles and some of them, namely the pions and the muons, were never observed before. All these pioneering works were the beginning of the modern and contemporary particle physics.

During the 1960s and 70s, with the help of particle accelerators and performant detectors, a large number of particles were discovered and studied. Initially, the idea was that all of them could have been fundamental particles, but soon turned out that they were constituted by smaller subtle particles, labeled in the beginning as partons and later as quarks.

## 1.1 The Standard Model

The model proposed in 1961 and 1967 by Sheldon Glashow, Steven Weinberg and Abdus Salam tried to insert within a single unique frame all the particles discovered up to that time, and the result was the Standard Model (SM).

Like a puzzle, every fundamental particle takes its place and is linked to the others. The real power of the model is that, within that frame, theoretical prediction could have been made. Two of the most important ones are the predictions of the electro-weak mediators, W

and Z bosons, confirmed in 1983 at the UA1 and UA2 experiments with the Super Proton Synchrotron accelerator at CERN (Geneva).
The most recent and revolutionary discovery was the key element of the SM, the Higgs boson, which was theorized in 1964 without specific mass value constraints. Only in 2012, it was announced the discovery of the last unknown Standard Model particle with a mass approximately of 125 GeV by the CMS and ATLAS collaborations, the two all-purpose experiments installed at the CERN Large Hadron Collider (LHC) [1].

The elementary particles of the Standard Model are shown in figure 1.1 and can be divided into two families, fermions and bosons, characterized by the values of the quantum numbers. Fermions and their anti-particles compose matter and anti-matter like fundamental bricks; on the contrary, gauge bosons are the mediators of the interactions among them. The substantial difference between these two families is the spin; fermions have half-integer spin which makes them obey Pauli exclusion principle due to the spin-statistic theorem. Conversely, bosons have integer spin and Bose-Einstein statistic, which let them condensate. This means that while different bosons can have the same quantum numbers, it is not possible for the fermions, which can only occupy one quantum state each.

### 1.1.1 Fermions

Fermions can be divided into two categories: quarks and leptons. Quarks can interact through strong force, whose charge is the color quantum number (blue, green, red), and are organized in isospin doublets according to the generation. This gives an $SU(3)_C$ symmetry group for the strong force. Quarks have fractional electrical charge, $2/3\ e$[1] for the up component of the doublet and $-1/3\ e$ for the down component; anti-quarks have opposite signs for electrical charge. Owing to the fact that the measured particles in nature are colorless (color confinement), quarks cannot exist by their own, thus it is necessary for them to undergo the hadronization process creating composed particles called hadrons. The number of constituents gives the name of the hadron family; two quarks of a color and the same anti-color form a meson, three quarks of different colors or anti-colors create a baryon.
Contrarily to the quarks, leptons cannot interact via strong force, so they are colorless. Due to the weak interactions which involves only the left chiral component of the particles,

[1] $e$ refers to the elementary electric charge, which has a value of $e = 1.6 \times 10^{-19}\ C$

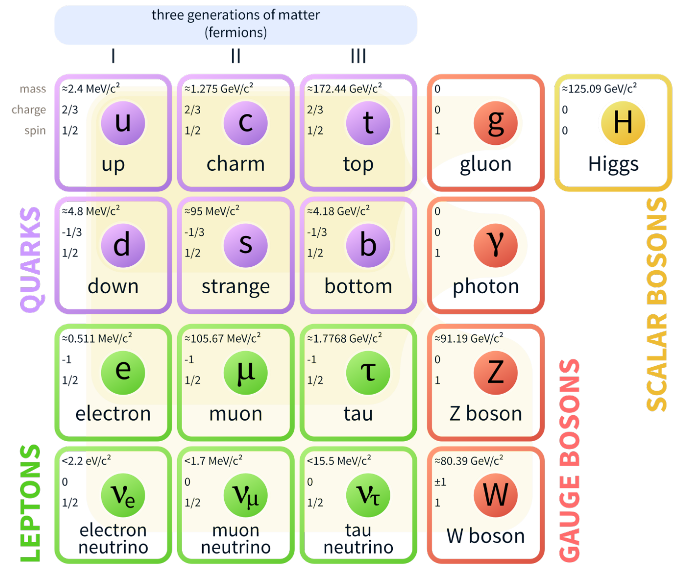


Figure 1.1: Elementary particles in the Standard Model. In violet and green are depicted the three generations of quarks and leptons respectively. In red are represented the gauge bosons of the Strong, Electro-Magnetic and Weak force and in yellow the Higgs boson responsible for the mass of the other fundamental particles

they are divided in doublets of the same specie; lepton neutrinos with zero electrical charge as the up component and leptons with $-1$ $e$ charge as down component. Therefore, the resulting symmetry group for the lagrangian of the weak interaction is $SU(2)_L$.

### 1.1.2 Bosons

Bosons are the fundamental particles with integer spin responsible for the interactions. The spin-1 vectors are the mediators of the three main interactions. Eight different colored gluons carry the strong force and have zero mass as well as zero electric charge. The massless photon and the two massive $W^{\pm}$ and $Z^0$ are the bosons responsible for the electromagnetic (EM) and weak interactions respectively. Glashow, Weinberg and Salam proposed in the '70 the ElectroWeak (EW) theory, combining together the electromagnetism and the weak interactions. To unify the two theories it is necessary to introduce the group symmetry $SU(2)\times U(1)$ for the lagrangian, with the corresponding massless gauge bosons $W_1, W_2, W_3$ of the weak isospin and the $B$ boson for the weak hypercharge interaction. $W^{\pm}$ are defined by the relation 1.1.

$$W^{\pm} = \frac{1}{\sqrt{2}} (W_1 \mp iW_2) \tag{1.1}$$

while, consequently to a symmetry breaking (EWSB) from $SU(2)_L \times U(1)_Y$ to $U(1)_{EM}$, the two remaining bosons become the observed $\gamma$ and $Z$, via a rotation of angle $\theta_W$ (1.2).

$$\begin{pmatrix} \gamma \\ Z^0 \end{pmatrix} = \begin{pmatrix} cos(\theta_W) & sin(\theta_W) \\ -sin(\theta_W) & cos(\theta_W) \end{pmatrix} \begin{pmatrix} B \\ W_3 \end{pmatrix} \tag{1.2}$$

This unification introduces a new quantum number for the particles, Y, which is related to the others by $Q = \frac{Y}{2} + T_3$, where $Q$ is the electric charge and $T_3$ is the third component of the weak isospin.
The last remaining problem to solve was the mass of the gauge bosons. Indeed, if the mass is introduced with a standard mass term in the lagrangian (for instance, $mA_\mu A^\mu$), it is not symmetry invariant. Thus, a new mechanism has been proposed by Brout, Englert and Higgs in 1964. It consist in a complex scalar field ($\phi$) with a potential of the form $V = \mu^2\phi\phi^* + \lambda(\phi\phi^*)^2$. The mass is introduced through a spontaneous symmetry breaking of the $U(1)$ group due to the "mexican hat" shape of $V$, given $\mu^2 < 0$. This generates a massive boson, also known as the Higgs scalar boson, and gives mass to the gauge bosons W and Z, leaving the photon massless.

The total group of symmetry resulting for the Standard Model lagrangian is therefore $SU(3)_C \times SU(2)_L \times U(1)_Y$.

## 1.2 Necessity of Beyond Standard Model theories

Although the Standard Model had several confirmations from the measurements carried out in the last 50 years, some aspects of the theory compared to the experiments can't be explained in this framework [2].
For instance, neutrinos in the SM are considered massless because the mass term need to embody both the left and right chiral components, but the right handed neutrino is sterile. Despite this fact, the flavour oscillation of neutrinos can be explained only in the case they are massive particles.

Other critical aspects of the SM are the impossibility to include the gravity as a renormalizable theory and the absence of a single meeting point in the strenght of the fundamental four forces at any energy, which could lead to the Grand Unification Theory (GUT).
Finally, one of the main problems, which became relevant in 2012 with the discovery of the Higgs boson with a mass of 125 GeV, is the hierarchy problem. It consists in the quadratic divergence in the propagator of fermionic and bosonic loops coupled with the Higgs boson (equation 1.3 for fermions, similar for bosons), leading to a huge correction on the mass ($\delta m_H$) depending on the energy scale in the integration ($\Lambda_{cut} \sim m_{Plank} \sim 10^{19}\ GeV$) and independent from the mass itself ($m_H$) (equation 1.4 for bosonic scalar field $S$).

$$\pi^f_{HH}(0) \propto \int \frac{d^4k}{(2\pi)^4}\left[\frac{1}{k^2-m_f^2} - \frac{2m_f^2}{\left(k^2-m_f^2\right)^2}\right] \tag{1.3}$$

$$\delta m_H \propto \Lambda^2_{cut} - 2m_S^2 log\frac{\Lambda_{cut}}{m_S} \tag{1.4}$$

## 1.3 Supersymmetry

Noticing that the divergence in the correction to the mass of the Higgs has opposite signs for fermions and bosons, a properly tuned symmetry between the two classes of particles was introduced in the '70, the so-called Supersymmetry theory (SUSY), allowing to overcome the hierarchy problem. This particular symmetry assigns to every SM particle a super-partner of the opposite type, correlating half-integer spin particles to integer spin particles. If the symmetry was still unbroken at low energy scales, two partners would have the same mass. Owing to the fact that no super-particles have ever been observed in the past or current experiments, the symmetry results necessarily spontaneously broken.
The algebra of this symmetry group is given by the equation 1.5,

$$\left\{Q_\alpha, \bar{Q}_{\dot{\beta}}\right\} = 2\left(\sigma^\mu\right)_{\alpha\dot{\beta}} P_\mu \tag{1.5}$$

where Q is the operator transforming a boson ($\phi$) into a fermion ($\psi$) and vice-versa ($Q|\phi\rangle = |\psi\rangle$, $Q|\psi\rangle = |\phi\rangle$), $\sigma^\mu$ are the pauli matrices and $P_\mu$ is the momentum operator $P_\mu = -i\partial_\mu$.

### 1.3.1 Minimal SuperSymmetric Model

The simplest model in which the supersymmetry realizes consistently with the SM is the Minimal SuperSymmetric Model (MSSM) [3],[4]. As SUSY it consists in having for each SM particle a super-partner or s-particle; s-fermion if the SM particle is a fermion or bosino in case of bosons. The five main classes of s-particles are squarks, gluinos, charginos, neutralinos and sleptons. All these s-particles can interact with SM particles, which can also be part of the decay products.
To provide the proton stability a new quantum number must be added, the R-parity, which gives the conservation of the baryonic (B) and the leptonic (L) numbers. It is given by $P_R = (-1)^{3(B-L)+2s}$, where $s$ is the spin of the (s-)particle and for SM particles it is equal to 1 and for the s-particles is -1. This implies two main features. The first one is that the final products of the decay chain of an s-particle must contain an odd number of lightest supersymmetric particles (LSP), usually the weakly interacting neutralinos ($\tilde{\chi}^0$), candidates for dark matter, or charginos ($\tilde{\chi}^{\pm}$), both mixtures of gauginos and higgsinos states. The other characteristic is that in a SM particle collider, s-particles are always produced in pairs.

### 1.3.2 Searches for specific supersymmetric particles: Heavy Stable Charged Particles

Searches for the supersymmetric particles have been carried out since the CDF and D0 experiments at Tevatron (Fermilab, USA) and are going on in the two main-purpose experiments of the LHC accelerator CMS and ATLAS. Up to now, no signals of discovery has been obtained in the analysis, however lower mass limits and upper cross-section limits have been put.
Among all the different scenarios that are theorized for the realization of the supersymmetry, the class of particles considered in the thesis work are the Heavy Stable Charged Particles. They are characterized by having lifetimes longer than a few nanoseconds, thus they can travel through all the detector before decaying and they can leave ionization signals in the subdetectors because of the $non-zero$ electric charge. The possible masses foreseen for this kind of s-particles range from 100 $GeV/c^2$ up to the $TeV/c^2$ scale.
The two main signatures for the HSCP when interacting with the detectors are an anomalous energy loss per unit length $\left(-\langle\frac{dE}{dx}\rangle\right)$ in the tracking system and a longer Time of Flight (ToF) in the muon system with relation to the SM particles.

# Chapter 2

# The experimental apparatus

## 2.1 The LHC project

The Large Hadron Collider [5], based at CERN in Geneva, is the largest proton-proton and heavy ion accelerator ever built. Designed to study the physics at the $TeV$ scale, it can collide protons up to a center of mass energy of $\sqrt{s} = 14\ TeV$ at an instantaneous luminosity of $L = 10^{34}\ cm^{-2}s^{-1}$ and lead ions up to 2.76 $TeV$ with a luminosity $L = 10^{31}$ $cm^{-2}s^{-1}$. The parameter values obtained in the first runs in 2017 have been a standard center of mass proton-proton energy fixed at $\sqrt{s} = 13\ TeV$ and a peak luminosity above the design limit at $1.68 \times 10^{34}\ cm^{-2}s^{-1}$. LHC is operating effectively since fall 2010 and will continue to provide collisions to the experiments with the present conditions until 2022 and, after a technical long shutdown, in 2025 will begin the High Luminosity LHC (HL-LHC) project to push the limit of the luminosity up to a value of $5 \times 10^{34}\ cm^{-2}s^{-1}$ and the integrated luminosity to 3000 $fb^{-1}$ at the end of 2035. This will give the possibility to test the SM predictions with high precision measurements to find potential inconsistencies and to investigate the scenarios beyond the SM.

### 2.1.1 The Large Hadron Collider machine

The LHC machine is a circular collider installed in a 26.66 $km$ tunnel at an average depth of 100 $m$, previously used for the Large Electron Positron accelerator (LEP), which was shut down in 2000. It consists in 8 arcs, each $\sim 3\ km$ long, kept at a working temperature of $1.9°K$ using superfluid helium to ensure the superconducting regime for the magnets located inside the beam pipe. The two beams, circulating around the ring in opposite directions, cross in 4 interaction points where are installed the four LHC experiments. ATLAS (A Toroidal LHC Apparatus) and CMS (Compact Muon Solenoid) are general-purpose experiments to study the SM and the physics BSM, while LHCb (LHC beauty experiment) is focused on the beauty quark physics to investigate the CP violation mechanism and ALICE (A Large Ion Collider Experiment) on quark-gluon plasma physics using heavy ion collisions.

Profiting of the accelerator chain present at CERN (figure 2.1), the two proton beams circulating in the LHC are injected in $2 \times 2808$ bunches with $1.15 \times 10^{11}$ particles each by the Super Proton Synchroton (SPS) accelerator at an energy of 450 $GeV$. While in the Run1 (until 2012) the bunches were spaced by 50 ns, in the current Run 2 they are spaced by 25 ns equivalent to a frequency of 40 $MHz$, which is the repetition rate of the collisions in the interaction points. This time unit is crucial to the experiments and is identified as "bunch crossing" (1BX= 25 $ns$).

The final acceleration in the LHC to reach the collision energy is provided by the RF stations, composed of superconducting Radio-Frequency cavities. To bend the trajectory of the beams along the ring, superconducting $Nb - Ti$ dipole magnets are needed. For 7 $TeV$ protons circulating in a of 27 $km$ circumference, equivalent to a radius $\rho \sim 4.3$ $km$, the intensity of the magnetic field needed, obtained with a circulating current of 11.8 $kA$, is 8.3 $T$ and can be calculated with the equation 2.1, with some corrections due to the impossibility to have bending magnets all over the beam pipe.

$$p\,[GeV] = \frac{q}{e} \cdot 0.3 \cdot B\,[Tesla] \cdot \rho\,[km] \tag{2.1}$$

Finally, 23 superconducting $Nb - Ti$ quadrupoles FODO cells, sextupoles and octupoles are necessary to reduce the cross section of the beam along the trajectory of the particles and especially in proximity of the experiments to increase the luminosity, which can be computed with the equation 2.2

$$\mathcal{L} = \frac{N_1 N_2 k_b f}{4\pi \sigma_x \sigma_y} \cdot F \tag{2.2}$$

where $N_1$ and $N_2$ are the number of particles in each bunch, $k_b$ the number of bunches, $f$ the revolution frequency, $\sigma_x = \sigma_y$ the radius of the distribution of the particles in the transverse plane of the beam and $F$ a correction factor for the non-zero crossing angle.

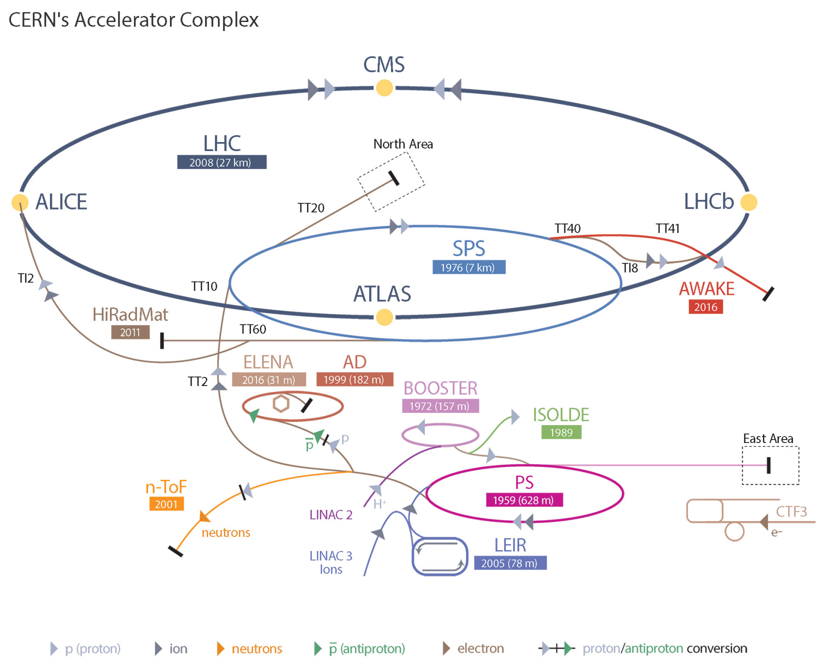


Figure 2.1: CERN accelerator complex. The proton beams for LHC start from the protons source with an energy of 750 $keV$, they are accelerated and organized in bunches in the LINAC2 and in the BOOSTER up to 1.1 $GeV$. Finally through the Proton Synchrotron and the Super Proton Synchrotron they reach the injection energy for LHC, fixed at 450 $GeV$.

From the equation 2.2, it can be inferred that the role of focusing quadrupoles is essential; decreasing the spread of the particles of the beams leads to an increase of the luminosity. The rate of events in the experiments is calculated with the formula 2.3

$$R = \sigma \cdot \mathcal{L} \tag{2.3}$$

where $\sigma$ is the cross section for the process. Given the total cross section for proton-proton interaction $\sigma_{tot} \approx 80\, mbarn$ at $\sqrt{s} = 13\, TeV$, the rate with the 2017 peak luminosity results $1.34 \times 10^9\ events/s$, corresponding to 33.5 events per bunch crossing (pile-up events). The total number of events in a period of time from 0 to $T$ can be calculated with the integrated luminosity $L$, usually measured in multiples and submultiples of $barn^{-1}$, through the equation 2.4.

$$N = \sigma \cdot L = \sigma \int_0^T \mathcal{L} dt \tag{2.4}$$

| Machine parameters | | |
|---|---|---|
| Parameter | Value | M.U. |
| Circumference | 26.66 | $km$ |
| Radius | $\sim 4.3$ | $km$ |
| Dipole magnetic field | 8.3 | $T$ |
| Dipole magnets | 1232 | |
| Quadrupole magnets | 392 | |
| Sextupole magnets | $2 \times 1232$ | |
| Octupole magnets | 1232 | |
| Beam parameters | | |
| Parameter | Value | M.U. |
| Energy per beam | 7 | $TeV$ |
| Design luminosity | $10^{34}$ | $cm^{-2}s^{-1}$ |
| Luminosity in 2017 | $1.68 \times 10^{34}$ | $cm^{-2}s^{-1}$ |
| Luminosity lifetime $\tau$ | 15 | $h$ |
| Number of bunches | 2808 | |
| Particles per bunch | $1.15 \times 10^{11}$ | |
| Bunch separation | 25 | $ns$ |
| Beam radius ($\sigma_{x,y}$) | 16.6 | $\mu m$ |
| Crossing angle | 285 | $\mu rad$ |
| Design Pile-up (collisions/BX) | $\sim 20$ | |
| Pile-up (collisions/BX) in 2017 | $\sim 40$ | |
| Energy stored per beam | 360 | $MJ$ |

Table 2.1: LHC proton-proton parameters summary

### 2.1.2 LHC developements: High Luminosity LHC

At the end of 2023, a 2.5 years long technical stop will occur to permit the installation of the new components in the beam pipe for the High Luminosity LHC project [6]. New cavities and collimators will be used for the beam cleaning and $11 \div 12$ $T$ $Nb_3Sn$ triplets of magnets will replace the original 8.3 $T$ $Nb - Ti$ ones. The pre-acceleration system will be also upgraded to obtain injected beams with twice the numbers of particles per bunch

in the same volume.
This improvements will lead to increase the luminosity by a factor 5 with respect to the design luminosity, reaching the value of 3000 $fb^{-1}$ of integrated luminosity during the 10 years of Phase 2 from 2025 to 2035.
This operating conditions will impose stringent restrictions on the radiation resistance of the experiment installed and specific solutions for each type of detector have to be studied and implemented.

## 2.2 The CMS experiment

The Compact Muon Solenoid experiment is one of the two multi-purpose detectors at the Large Hadron Collider devoted to the search for new physics mainly using $p-p$ collisions [7]. It is located in a cavern 100 $m$ under the surface of Cessy, France, in the so-called Point5 (P5) LHC experimental area. Composed by several layers of high granularity synchronized detectors, each one specific for measuring different properties of the particles generated in the collisions, and a 4 $T$ solenoidal magnetic field for bending the trajectories, it is designed to provide high precision measurements for the stable[1] particles crossing the detector and for the reconstruction of the decay vertexes. The performance of the CMS detector allows to identify the particles and to measure their trajectories, the energy and the momentum, including the missing energy.

### 2.2.1 CMS design and characteristics

The CMS detector, as shown in figure 2.2, has a cylindrical shape with total dimensions of 21.6 $m$ in length and 15 $m$ in diameter and a weight of 12500 $tons$. Due to the high symmetry of the collision topology, this particular shape grants to cover the largest variety of trajectory directions of the particles generated in the collisions or in the subsequent decays. The entire structure is divided into three main blocks, the central Barrel, composed by 5 slices (wheels), and the two Endcaps.
The natural coordinate system for CMS and for most of the multi-purpose detectors in high energy physics is a right-handed system with the center in the nominal collision point. The x-axis points radially to the center of LHC, the y-axis is normal to the ground plane

[1] 'Stable' here refers to particles which don't decay before crossing the entire detector or before being completely stopped inside the volume

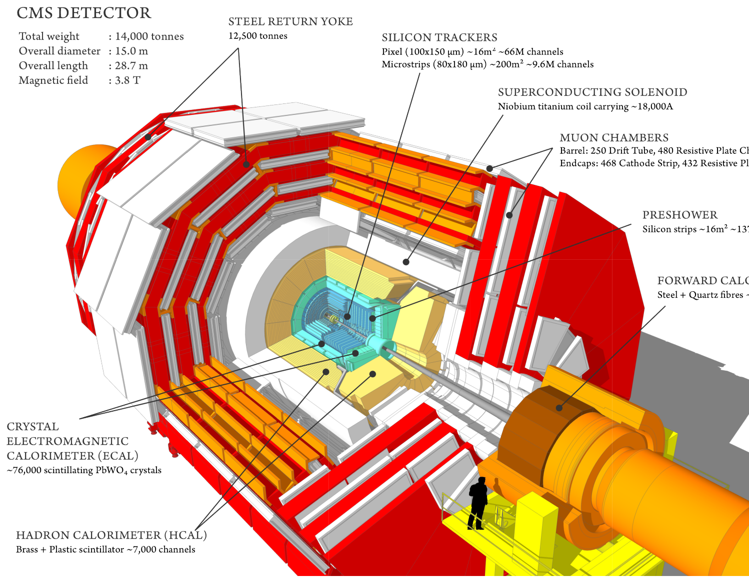


Figure 2.2: Overview of the CMS detector

directed upwards and the z-axis is along the beam pipe. The x-y plane is usually referred as the transverse plane and the projection of the particles energy and momentum in that plane are indicated as $E_T$ and $p_T$. An alternative set of coordinates are the azimuthal angle $\phi$ in the x-y plane measured from the x-axis and the polar $\theta$ angle. A more common way to represent the polar angle is through the pseudorapidity $\eta$, calculated with the equation 2.5, which becomes equal to the rapidity $y$ in the ultra-relativistic limit (equation 2.6).

$$\eta = -ln\left(tan\left(\frac{\theta}{2}\right)\right) \tag{2.5}$$

$$y = \frac{1}{2}ln\left(\frac{E+p_z}{E-p_z}\right) \approx \frac{1}{2}ln\left(\frac{p+p_z}{p-p_z}\right) = -ln\left(tan\left(\frac{\theta}{2}\right)\right) \tag{2.6}$$

Each part of CMS is composed by several layers of detectors with specific roles in measuring the particle properties. The inner part of the solenoid contains the silicon tracker system for measuring the tracks of charged particles (starting point, direction and momentum) and for identifying vertexes. At larger radius, still inside the solenoid, in the electromagnetic calorimeter electrons and photons are identified, while the hadronic particles and the jet properties are measured in the hadron calorimeter. The muons are identified and their tracks are measured with gaseous subdetectors placed outside the solenoid and sandwiched in the magnetic field yoke. In the barrel region, $\eta < 1.2$, the muon system is composed by Drift Tubes Chambers and Resistive Plates Chambers. In the Endcaps, RPCs and Cathode Strips Chambers are employed for their radiation resistance.

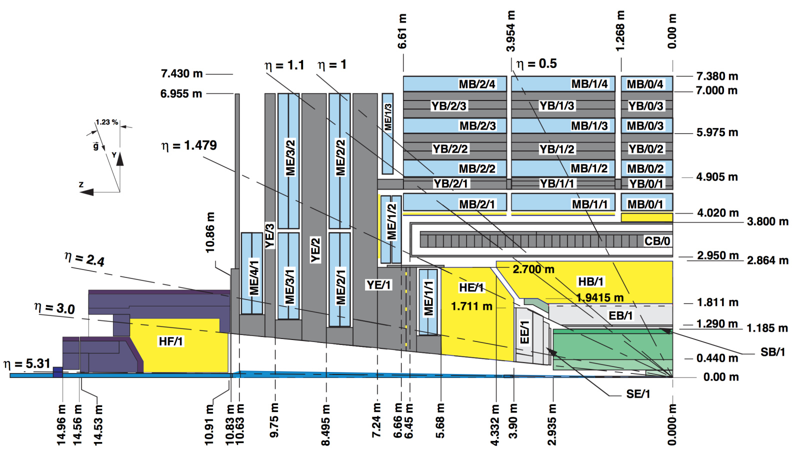


Figure 2.3: CMS detector longitudinal view. Subdetectors highlighted in different colors with $\eta$ ranges.

### 2.2.2 The silicon tracker

The innermost subdetector of the CMS experiment, is the silicon tracker. It has a total length of 5.8 $m$ and a diameter of 2.5 $m$, covering a pseudorapidity $|\eta| < 2.5$ and radii between 0.2 and 1.2 $m$. To cope with high particle fluxes during the beam interactions, a high granularity is required to reduce the occupancy and improve the spatial resolution. In the barrel, pixel detectors (changed just before the 2017 data taking to recover from aging effects) are used in the first four layers close to the beam pipe and strips in the four inner and six outer layers. In the endcaps, three layers of pixels and two inner and two outer layers of strips are employed to track the paths of the particles generated in the interactions and the decay vertexes. All the system is composed by 65 million channels for pixels and 10 million for strips and must be kept at a temperature of $-10°C$ to preserve the integrity of the electronics and ensure good performance.

For low energy or low transverse momentum ($p_T$) hadrons ($1GeV/c < p_T < 10GeV/c$) the reconstruction efficiency is 85%, while for higher energies ($p_T > 10GeV/c$) it becomes 95%. For electrons is estimated to be around 90% and 98% for muons. The $\delta p_T/p_T$ in the region $|\eta| < 1.6$ is lower than the 2%.

### 2.2.3 The Electromagnetic Calorimeter

The electromagnetic calorimeter (ECAL) was designed to perform measurements of energy with precision up to 1% for electrons and photons and, working in team with the hadronic calorimeter, for hadronic jets. A segmented homogeneous and hermetic scintillation detector has been chosen to address these requirements, using $PbWO_4$ crystals. This material has been selected because of the small Molière radius (22 $mm$), the short radiation length ($X_0 = 8.9$ $mm$), its radiation-hardness and the very short scintillation-decay time, which ensure to collect the $\sim 85\%$ of the light emitted inside the crystal in the 25 $ns$ between two following bunch crossings. The trapezoidal shape that characterizes the crystals has dimensions for the squared basis of $22 \times 22$ $cm^2$ and $28.6 \times 28.6$ $cm^2$ respectively for the barrel and the endcaps, with lengths corresponding to 25.8 and 24.7 $X_0$. $61200 + 7324$ crystals for the two constituent blocks cover the $|\eta| < 3.0$ region. To collect and read the scintillation light produced, Vacuum Photodiodes, Avalanche Photodiodes and Silicon PhotoMultipliers for working in a magnetic field of 4 $T$ were preferred because of the high intrinsic gain able to match the low light output given by the $PbWO_4$ crystals, 4.5 $\gamma/MeV$ at the controlled temperature of $18°C$ to keep them stable.
The ECAL energy resolution is given by the equation 2.7, where $S = 0.028$ $GeV^{\frac{1}{2}}$ is the *stochastic* term, $N = 0.12$ $GeV$ the contribution from the *noise* and $C = 0.003$ contains all the other *constant* uncertainties, given for instance by the calibrations. Accurate calibration is continuously performed during the data taking.

$$\left(\frac{\sigma_E}{E}\right) = \frac{S}{\sqrt{E}} \oplus \frac{N}{E} \oplus C = \frac{2.8\%}{\sqrt{E[GeV]}} \oplus \frac{12\%}{E[GeV]} \oplus 0.3\% \tag{2.7}$$

### 2.2.4 The Hadronic Calorimeter

The hadronic calorimeter (HCAL) is used to determine the energy of the hadronic jets and to take into account of the missing transverse energy $E_T^{miss}$ in the event. Thus a hermetic detector with high granularity is needed, with compact dimensions to fit the reduced space imposed by the solenoidal magnet. A sampling calorimeter has been chosen

to fulfill these requirements, composed by alternated layers of brass absorber and active plastic scintillator.The scintillation light is carried out from wavelength shifting fibers and wave-guides towards hybrid photodiodes for the photon detection. To absorb high energy hadrons generated in the 14 $TeV$ collisions in 11.8 interaction lengths, it has been necessary to place the HCAL not only inside the magnet (HB and HE), but also to have other layers outside (HO), covering pseudorapidities of $|\eta| < 3.2$, and in the forward directions (HF) to extend the angular acceptance up to $|\eta| < 5.2$. Owing to the severe conditions of operation in the high pseudorapidity regions, for the forward hadronic calorimeter steel slabs have been used as absorber and quartz fibers as active layers, detecting the Cerenkov light produced by the crossing particles.
The HCAL energy resolution is given by the equation 2.8, where $S = 1\ GeV^{\frac{1}{2}}$ and $C = 0.45$.

$$\left(\frac{\sigma_E}{E}\right) = \frac{S}{\sqrt{E}} \oplus C = \frac{100\%}{\sqrt{E[GeV]}} \oplus 45\% \tag{2.8}$$

### 2.2.5 The solenoid magnet

With dimensions of 12.9 $m$ in length, an inner diameter of 5.9 $m$ and a magnetic field of 4 $T$ in the inner part and residual 2 $T$ in the returning iron yoke, the CMS superconducting magnet is the most powerful solenoid in the world. It provides bending of particle trajectories in the transverse plane, obtaining less than 5% charge misidentification for muons of transverse momenta less than 200 $GeV$, $\delta p/p \approx 1\%$ for $p_T = 100\ GeV$ and less than 10% for transverse momenta up to 1 $TeV$. This performance is obtained with a current of 19.14 $kA$ in 2168 turns, requiring a temperature of $4.5°K$ to keep the system in superconducting conditions.

### 2.2.6 The muon system

The particles that are enough energetic to traverse all the electromagnetic and the hadronic calorimeters, such as muons with $p_T > 3GeV$ are measured in the outermost group of subdetectors of the CMS experiment, the muon system, constituted by four stations in the barrel and four disks in the endcaps, covering an angular range of $|\eta| < 2.4$ (figure 2.5) . It is a robust and redundant muon spectrometer that can provide precise muon identification and high resolution $p_T$ measurements.
The muon spectrometer consists in three different types of gaseous detectors; 250 Drift Tubes Chambers (DTs) are used in the barrel region ($|\eta| < 1.2$) where the occupancy

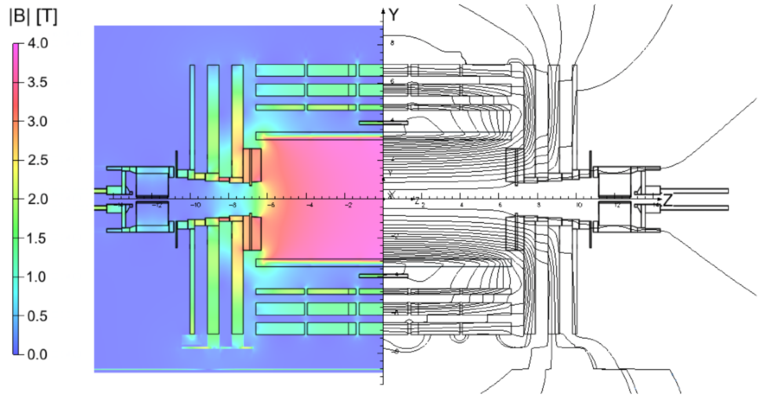


Figure 2.4: Map of the magnetic field generated by the superconducting solenoid in the CMS detector

is lower and there is a very low residual magnetic field, while faster and more radiation resistant 540 Cathode Strip Chambers (CSCs) have been chosen for the two endcaps (0.8 $< |\eta| < 2.4$) to cope with higher particle fluxes and non uniformities in the magnetic field. 610 Resistive Plate Chambers (RPCs) complement the DTs and the CSCs in both regions up to $|\eta| < 2.1$, because of their fast response and excellent time resolution, to improve the precision in the muon trigger on the determination of the bunch crossing (BX) in which the muon has been created.
As shown in figure 2.6, for muons with $p_T < 200\ GeV$, the tracker precision is the most relevant because of the multiple scattering occurring when crossing the calorimeters, the coil and the iron yoke of the muon part. For muons with higher transverse momenta, the full system resolution takes advantages of the inclusion of the track points in the muon system, improving the tracker resolution.

### 2.2.7 Drift Tube Chambers

The muon barrel region outside the solenoid is characterized by a low residual magnetic field, low occupancy and a large area to be covered. Because of those reasons, in the barrel region, Drift Tube chambers have been employed [8],[9]. The DTs are gaseous detectors fitting into the the iron yoke structure, which consists in 5 wheels, referred as Wheel$-2$ to Wheel$+2$, and 12 azimuthal sectors, labeled with numbers $1 \div 12$ starting from the x-axis (figure 2.7). For each wheel, 4 concentric rings (stations) of DT chambers are installed,

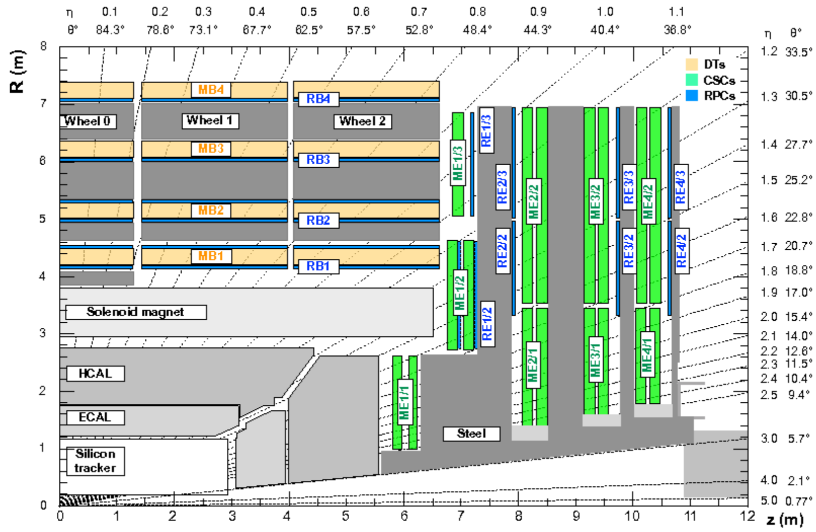


Figure 2.5: CMS muon system longitudinal view. The muon subdetectors are highlighted in different colors.

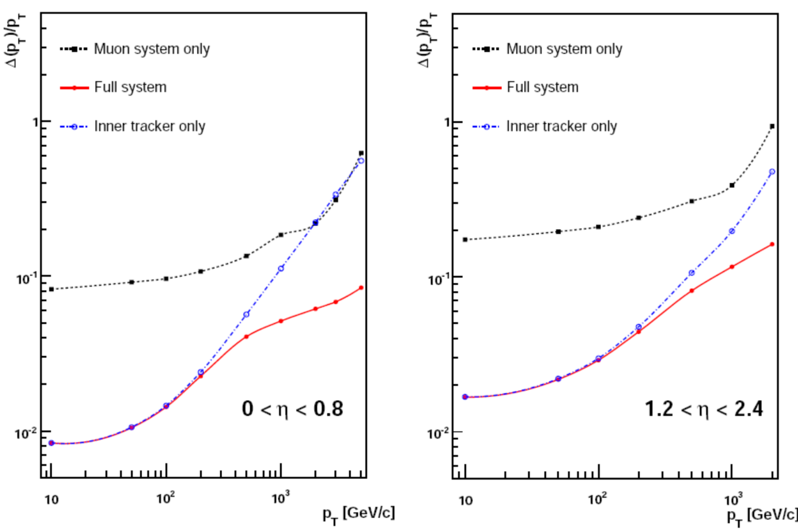


Figure 2.6: Muon transverse momentum resolution as a function of $p_T$ for the inner tracker only, the muon system only and the two systems combined. On the left the results for the barrel are shown and on the right for the endcap.

named MB1, MB2, MB3, MB4 respectively from the inner to the outer part. Each station in a sector is constituted by one DT chamber, except in sector 4 and in sector 10 where the MB4 are made by two DT chambers.

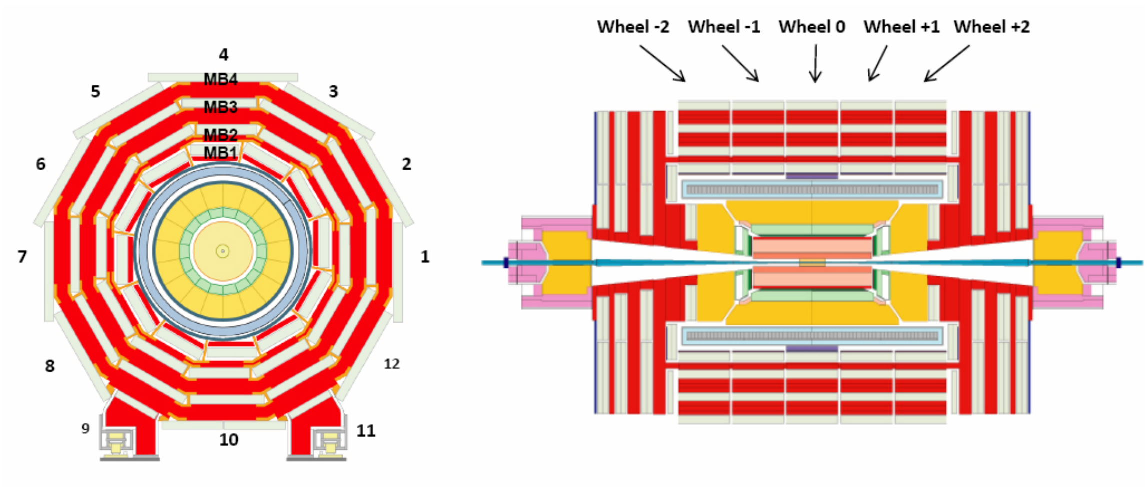


Figure 2.7: Drift Tubes Chambers in CMS: disposition of wheels, sectors and stations in the CMS detector.

The basic element of the DT system is the drift cell (figure 2.8). The cell has a transverse size of $42 \times 13$ $mm^2$ with a 50 $\mu m$-diameter gold-plated stainless-steel wire at the center. The cell design makes use of 5 electrodes to shape the effective drift field: the anode wire, 2 cathode strips on the side walls of the tube, 2 strips above and below the wire on the ground planes between the layers. Up to now, they have been operating at +3600 V, −1200 V and +1800 V respectively, generating a uniform electric field along the cell. A gas mixture of Ar/$CO_2$ (85%/15%) is used; it provides good quenching properties and, in the constant electric field of the cell, a saturated drift velocity for the electrons of 55 $\mu m/ns$, corresponding to a maximum drift time faround 385 $ns$. The front end (FE) electronics and the high voltage (HV) connections are placed at opposite side of the wires inside the gas flux.

Four staggered layers of parallel cells form a superlayer (SL). A DT chamber consists of 2 SLs that measure the $r - \phi$ coordinates with wires parallel to the CMS beam line, and an orthogonal SL that measures the $r - z$ coordinate (being r the nominal radial distance from the beam collision point). The DT chambers are 2.5 $m$ in depth and their length varies, ranging from 1.9 $m$ to 4.1 $m$ [10],[11].

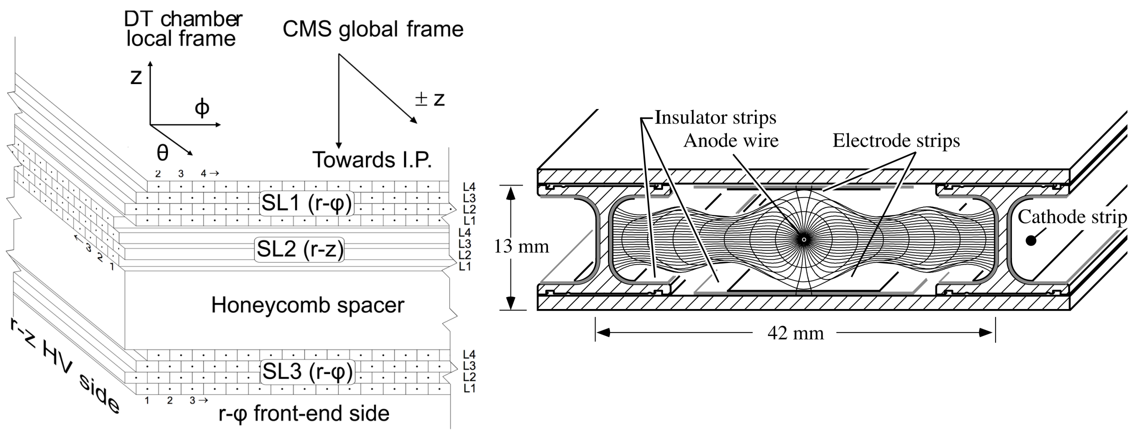


(a) Schematic view of a DT chamber

(b) Section of a drift tube cell showing the drift lines and isochrones

Figure 2.8: DT chamber and DT cell schematics

The CMS Drift Tube Chambers are the only drift detector which is capable to auto-trigger. Indeed, thanks to the constant drift velocity and to the half-cell staggering between two consecutive layers, the measurement of the arrival time at the anode wire, whichever the used reference time, allow to identify the time of a track crossing the cells in this reference. Given a straight trajectory of the particle inside the superlayer and a constant distance among the wire planes, the relation among the real drift times (schematically depicted in figure 2.9) is:

$$T_{max} = \frac{T_d(1) + T_d(3)}{2} + T_d(2) \tag{2.9}$$

which is independent from the angle of the track ($\Psi$) and the position along the plane of the cells ($d_0$).
The key element of the algorithm is called "mean timer technique" [12], which is applied at any combination of three layers of a superlayer and relies on the fact that the drift velocity $v_d$ is constant along the cells. A hardware comparison of the four combinations gives the absolute crossing time, the position along the layer plane and the direction of the track in the superlayer.
Up to now, single DT cells had an efficiency greater than 98% (chapter 7) and a spatial resolution of $\sim$ 200 $\mu m$, once all the relevant systematics have been taken into account

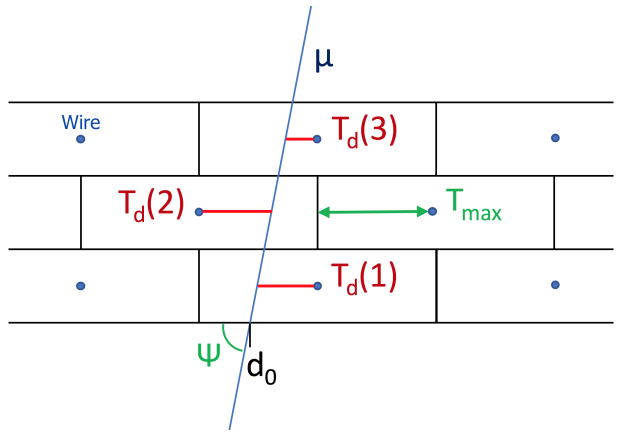


Figure 2.9: DT mean timer technique for the absolute particle crossing time determination, given the incoming $d_0$ position and the angle $\Psi$ of the muon track with relation to the chamber. The $T_d$ are the real drift times.

[13],[14],[15]. In the $\theta$ projection, the resolution of $\sim$ 200 $\mu m$ in the wheel 0 becomes 600 $\mu m$ in the external wheels. Given the 4+4 layers of the 2 $\phi$ superlayers and their disposition, the offline reconstruction code achieves a resolution of 100 $\mu m$ for the measured $\phi$-position.

### 2.2.8 Cathode Strip Chambers

The solution adopted for the muon system in the endcaps to deal with high magnetic field and particle rate are the Cathode Strip Chambers. The CSCs are gaseous trapezoidal Multiwire Proportional Chambers (MWPC), characterized by a short drift length which leads to fast signal collection. They are arranged in four disks (stations), each one made of three concentric rings of chambers. Each chamber is composed by 6 layers of anode wires enclosed between two planes of finely segmented cathode strips for the collection of the ionization signal produced in the 30%/50%/20% $Ar/CO_2/CF_4$ gas mixture. The wires give information about $r$ coordinate and the strips are used to determine the polar angle. To increase the precision in the $\phi$ measurement, a weighted mean is performed with the charge in neighbor strips. The position resolution measured with the strips varies in the range $70 \div 150$ $\mu m$ depending on the station, while $r$-position can be determined with a precision of 0.5 $cm$.

### 2.2.9 Resistive Plate Chambers

Used as complement detector for both the DTs and the CSCs, with 6 layers in the barrel and 3 in the endcap regions (2.5), the Resistive Plate Chambers ensure redundancy to the muon spectrometer and improve the time resolution of the system. RPCs are gaseous detectors with a coarse spatial resolution (1-2 $cm$) that can perform precise time measurements with an intrinsic resolution of $\sim 1\ ns$, once the geometrical position systematics are considered. CMS uses double-gap RPC chambers composed by 4 bachelite planes forming two 2 $mm$ gaps where the crossing particles ionize the 90%/5% freon-isobutane gas mixture and the electrons are multiplied in avalanche mode. The electrodes, set at a potential of 9.5 $kV$, are constituted by graphite coating the bachelite planes and insulated aluminium strips are used to collect the signal.
The digitized RPC information - hit strip numbers - are stored in the readout data at each BX. Up to 2015, the signals of the strips of different RPC chambers were connected to an independent muon hardware trigger (PAattern Correlator Trigger) able to identify tracks and classify their $p_T$ at each BX. From 2016, the hardware of the PACT was replaced by an entirely redesigned trigger chain which uses the RPC readout data (section 2.4).

## 2.3 Local and global muon reconstruction

Muons and other charged particles, traversing a muon subdetector, ionize the gas in the chambers. The produced electrons, after a multiplication, induce signals on strips or wires. These signals are read out by electronics and are associated with well-defined locations, generically called hits, in the detector. From the reconstructed hits of the multiple layers of the chambers, straight track "segments" are built for each station in the two projections. This first stage of reconstruction is, therefore, called local segment reconstruction. Combining segments from multiple chambers or stations and their positions, standalone muon tracks are reconstructed. The global reconstruction, instead, matches tracks identified with the inner tracker with the standalone tracks. For the different analyses performed in CMS, a variety of algorithms has been developed to accommodate both the different combinations of detectors and the physics requirements for muon identification.

### 2.3.1 Local segment reconstruction in the DT chambers

Local hit reconstruction in a DT layer measures the distance of the crossing muon from the anode wire, registering the signal arrival time with a Time to Digital Converter (TDC) [16]. The position of a DT hit is computed using the trigger time ($t_{Trig}$) and the electron drift velocity ($v_d$): $pos = (t_{TDC} - t_{Trig}) \cdot v_d$. $t_{Trig}$ is due to the time of propagation of a trigger decision through the system; the calibration is done considering tracks passing close to the wires, for which $t_{Trig}$ must be equal to $t_{TDC}$, and assuming an equal time for the muons to reach a given layer from the interaction point. However, this assumption is not exactly true because of intrinsic time-of-flight spread due to the momentum and velocity distributions of the particles generated in the interactions. In order to take into account the possible time shifts, segment reconstruction in the DTs is performed as a three-parameter fit, including the muon crossing time ($t_0$) besides the transverse position along the chamber and slope. This procedure optimizes the hit time alignment improving the spatial resolution and the precision on the muon crossing time [17],[18].

## 2.4 The CMS trigger system

The LHC collisions have a rate of 40 MHz (20 $MHz$ up to 2012), which means that two proton bunches intersect in the collision points where the experiments are placed every 25 ns = 1 BX (50 ns = 2 BX). Owing to the fact that in the two main purpose experiments ATLAS and CMS each event has a size of 1 MB, given the actual Data Storing capability, the rate of events that can be stored for offline analysis has been fixed up to now to $\sim 100$ $Hz$.

The task of this dramatic reduction is demanded to the on-line trigger chain of the experiments: the selections are based on tuned identification of specific objects and properties and event topologies. In CMS it is performed in two steps, nominally the Level1 Trigger (L1T) and the High Level Trigger (HLT). The L1T reduces the rate by a factor 400 elaborating signals from the muon detectors and the calorimeters. It is built as a pipeline using custom hardware, taking decisions every bunch crossing with a fixed latency. The remaining selection is done by HLT algorithms, equivalent to offline ones, running on a large computer farm with commercial processors.

### 2.4.1 The muon L1 Trigger

Designed to take decisions to accept or reject events at a 40 $MHz$ rate (every BX), the L1 trigger is implemented in a pipeline mode using custom developed programmable hardware. Field Programmable Gate Arrays (FPGA), Application Specific Integrated Circuits (ASICs) and programmable Lookup Tables (LUTs) are programmed to complete every processing step in less than 25 $ns$. Due to the maximum length for the pipeline buffers fixed at 128 BX (3.2 $\mu s$), taking into account the signal propagation time and the subdetectors latencies, the effective decision operation time for the L1T is less than 2 $\mu s$.
The Level 1 Muon Trigger of the CMS detector consists in the Global Trigger receiving candidates from the Calorimeter Trigger (electrons, photons and jets) and the Muon Trigger (isolated and non-isolated muons).

### 2.4.2 Legacy muon L1 Trigger

Until 2016, the Muon Trigger had three components for the three muon subdetectors (DT, CSC and RPC) and each one was linked to the Global Muon Trigger (GMT). The GMT received 16 muon candidates in total, 4 for DTs, 4 for CSCs and 8 for RPCs and chose the best 4 muon candidates, with their position, $p_T$ and quality, to be sent to the L1 Global Trigger (GT).
The L1 Muon Trigger, therefore, is not aimed to take decisions, but to identify and perform a sorting of the different trigger objects (electrons, photons, jets and muons) and forward them to the Global Trigger.

### 2.4.3 Upgraded muon L1 Trigger

The solution chosen for the upgrade of the L1 Muon Trigger and applied since 2016 was to create an integration between the different muon subdetectors belonging to the same regions of CMS [19]. The result is the division in three pseudo-rapidity zones: the Barrel covering the values of $|\eta| < 0.8$ with DTs and RPCs, the two Overlaps with $0.8 < |\eta| < 1.2$ (DTs, CSCs and RPCs) and Endcap regions ($1.2 < |\eta| < 2.4$), with CSCs and RPCs. With this configuration, the different performance in term of time and spatial resolution of the subdetectors in each region are better combined to obtain improved and refined trigger candidates to be sent to the GMT.

Every step described in the following lines is performed at each BX (40 $MHz$). As before, each DT chamber produces up to two primary trigger information "local trigger primitives" in the on-board hardware modules placed in its "minicrate" identifying the tracks crossing the chamber, as shown in figure 2.10.

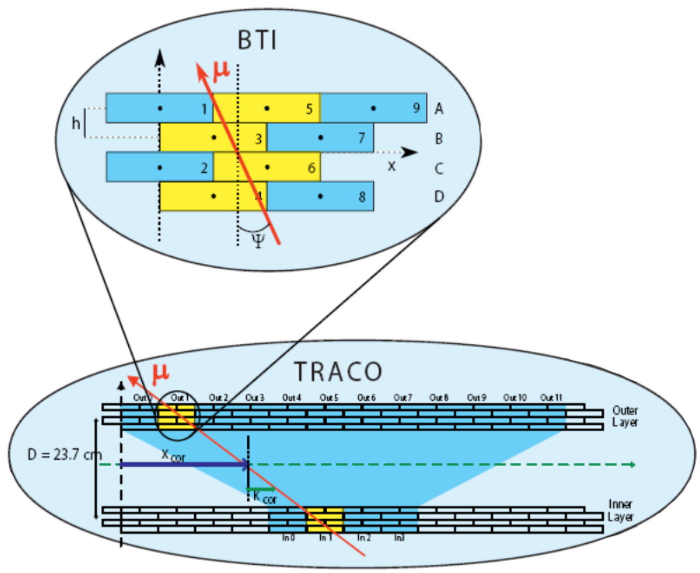


Figure 2.10: Primitive generation in the on-board hardware of the DT Local Trigger system from the hits of the inner and outer $\phi$ superlayers.

In the upgraded barrel muon L1 trigger, these trigger primitives are sent with optical fibers to the TwinMux boards, which play the role of the trigger data concentrator for each sector [20]. Each TwinMux receives also the information of the RPCs installed in the muon stations of the sector and elaborates them producing the equivalent local trigger primitives. After a comparison of the DT and RPC local trigger primitives, the generated "superprimitives" are forwarded to the Barrel Muon Track Finder (BMTF) [21].
Each BMTF module accepts superprimitives coming from 3 neighbor wedges (5 sectors in 5 wheels with the same label). It identifies muon tracks if at least two superprimitives in two different stations can be correlated, producing a trigger candidate with information about $p_T$, $\phi$, $\eta$ and quality. Finally the candidates are sent to the GMT, which sorts and selects

the best muon track candidates before forwarding them to the GT.
Similarly to the barrel region, a L1 trigger structure has been created comparing CSC and RPC primitives in the Concentrator and PreProcessor Fan-out (CPPF) board and reconstructing the tracks in the Endcap Muon Track Finder (EMTF).
In the overlap regions, the Overlap Muon Track Finder reconstructs trigger candidates receiving superprimitives from the TwinMux and the CPPF and send them to the GMT.

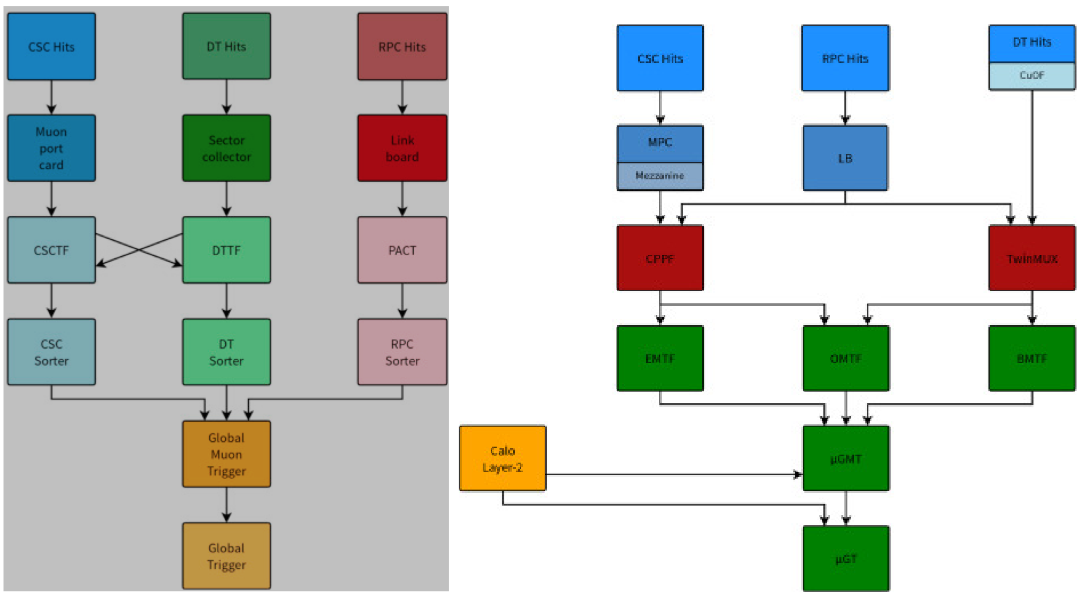


(a) Legacy muon L1 trigger chain (old) (b) 2016 upgraded muon L1 trigger chain

Figure 2.11: Block diagrams of legacy and upgraded L1 muon trigger.

In the thesis work, the tests and the implementations have been done at the TwinMux stage of the trigger chain, thus a short description of the TwinMux system is given.

### The TwinMux

As reported above, the TwinMux is the data concentrator of the L1 barrel muon trigger chain within a sector. Its main role is to compare, for the $\phi$ projection, the DT trigger primitives with the RPC ones correcting or confirming the BX assignment according to their coordinate and in case the difference of their BX is less than 1. The DT BX assignment

have, indeed, have a non null probability to pre-trigger[2] due to $\delta$-electrons. The TwinMux can also add a RPConly candidate if there are no DT primitives in the first or second stations, where there are 2 RPCs (inner and outer).
From the hardware point-of-view, TwinMux is a $\mu$TCA board, based around a XILINX Virtex-7 FPGA and equipped with optical connections for high speed data transmission up to 13 Gbps (figure 2.12). To cover the full barrel, 60 TwinMux are hosted in 5 TCA dual star crates with more than 3000 optical fibre cables for the input and output connections.

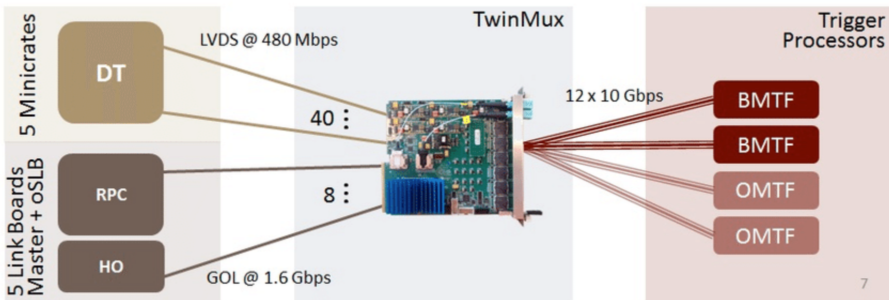


Figure 2.12: TwinMux board with input and output details.

Every BX, it receives up to 10 DT trigger primitives from the Front-End electronics (minicrates) installed in the muon DT chambers and up to 26 from the RPCs and is connected in output to the Barrel Muon Track Finder. The trigger primitive information contained in the input bitstream are:

- $\phi$, corresponding to the azimuthal coordinate relative to the point where the segment connecting the center of CMS to the DT chamber is normal to the surface

- $\phi_b$, representing the inclination of the trigger primitive in one DT chamber with relation to the straight line connecting the proton-proton interaction region to the crossing point of the particle in the chamber

- $\phi$ quality, ranging from 0 to 6 corresponding to the codes $L_{i,o}$,$H_{i,o}$,LL,HL,HH, where L = 3 hits (number of layers with a signal) and H = 4 hits in the inner and outer $\phi$ superlayers (figure 2.10)

[2] A pre-trigger is defined as a time identification of the primitive at the previous BX than the correct one.

- $\theta$, corresponding to the polar angle
- $\theta$ quality, only L or H because of the only one $\theta$-superlayer
- $1^{st}/2^{nd}$ track in the same chamber

In this way, the trigger superprimitives embed both the good spatial resolution of the DTs ($100 \div 200$ $\mu m$) and the BX assignment reliability of the RPCs. Indeed, the DTs miss the BX assignment in the 5% of the primitives, while the RPCs only the 0.5% of the times [22]. This changes introduced with the TwinMux improved the efficiency of 1.5% with relation to the previous trigger chain.

# Chapter 3

# HSCP searches with the CMS detector

Two main signatures can be used to select HSCP candidates at collider experiments such as CMS and ATLAS: an anomalous energy loss per unit length an anomalous energy loss per unit length $\left(-\langle\frac{dE}{dx}\rangle\right)$ in the inner tracker and a longer Time of Flight (ToF) in the muon system, both related to the low speed of high mass and relatively low momentum particles. Indeed, three types of analysis can be conducted, depending on the nature of the HSCP particle. Tracker-only analysis is focused on hadronic-like particles (R-hadrons) which, interacting with the detector, become neutral before reaching the muon system; the Tracker+ToF analysis investigates the case of R-hadrons or muon-like HSCP which stay charged during all the path inside the detector; the Muon-only analysis is applied for identifying R-hadrons generated as neutral particles that become charged after the tracker. The three possible analyses are schematically summarized in figure 3.1 as performed in CMS.

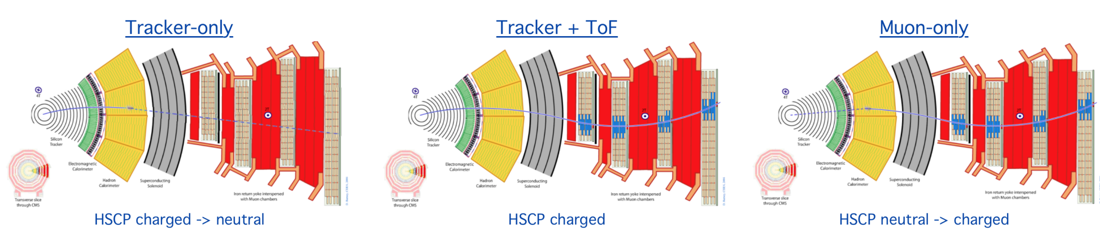


Figure 3.1: Tracker-only, Tracker+ToF and Muon-only HSCP possible analysis.

The event selection for the three analyses requires either a single muon with high transverse momentum ($p_T > 50\ GeV$) trigger or a large missing energy ($E_T^{miss} > 170\ GeV$) trigger. $E_T^{miss}$ is defined by the opposite of the vector sum over the transverse momenta of all final-state particles in the events. The $E_T^{miss}$ trigger is used for increasing sensitivity for HSCP candidates that arrive in the muon system very late and then are triggered eventually as a muon at the following BX (missing the tracker information), as well as for hadron-like HSCPs, which can be charged only in the tracker.

The muon and the missing energy trigger efficiencies for all HSCP models are presented in figure 3.2, showing a dramatic decreasing of the efficiency for the muon trigger below $\beta = 0.6$.

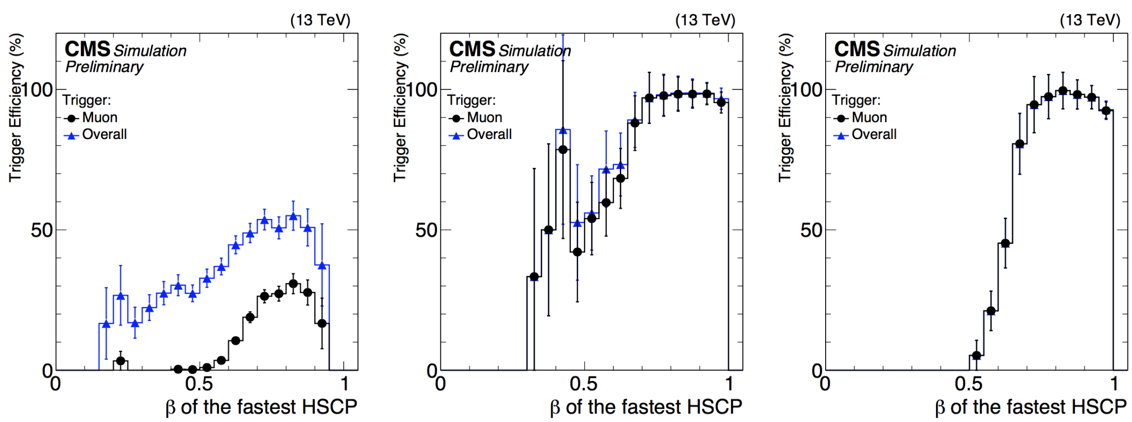


Figure 3.2: Trigger efficiency as a function of the $\beta$ of the fastest HSCP reconstructed in the event for gluino of 1600 $GeV$ (left), GMSB stau of 308 $GeV$ (middle), and paired-produced stau of 308 $GeV$ (right) samples.

The track-only analysis isolates HSCP candidates by selecting tracks reconstructed in the inner tracker detector with high ionization energy loss and high transverse momentum. The tracker+ToF selection additionally requires that the tracks are loosely identified as muons. The third one requires a track reconstructed at least in the muon system. The mass of the HSCP candidates are reconstructed from the track momentum and the beta of the particle measured with the ionization loss or computed from the ToF.

A counting experiment is performed to search for excess in data compatible with an HSCP signal. The estimation of the background is done exploiting the absence of significant correlation between the $p_T$ and a specific ionization measurement and between the $p_T$ and the $\beta$ from the ToF. A data-driven method that exploits this lack of correlation among the considered observables is used to estimate the background from SM particles, MIPs traveling at the speed of light.

The current limits by the CMS collaboration [23] for gluinos, stop and staus are summarized in table 3.1 and in figure 3.3.

| Model | Analysis | Mass Limits |
|---|---|---|
| Gluino $f$=0.1 | Tracker-only | $M > 1850(1850)$ GeV |
| | Tracker + ToF | $M > 1810(1810)$ GeV |
| Gluino $f$=0.1 CS | Tracker-only | $M > 1840(1840)$ GeV |
| Gluino $f$=0.5 | Tracker-only | $M > 1760(1760)$ GeV |
| | Tracker + ToF | $M > 1720(1720)$ GeV |
| Gluino $f$=0.5 CS | racker-only | $M > 1800(1800)$ GeV |
| Stop | Tracker-only | $M > 1250(1250)$ GeV |
| | Tracker + ToF | $M > 1200(1200)$ GeV |
| Stop CS | Tracker-only | $M > 1220(1220)$ GeV |
| GMSB Stau | Tracker-only | $M > 660(660)$ GeV |
| | Tracker + ToF | $M > 660(660)$ GeV |
| Pair prod. Stau | Tracker-only | $M > 170(170)$ GeV |
| | Tracker + ToF | $M > 360(360)$ GeV |

Table 3.1: Supersymmetric particles candidates: lower mass limits using CMS 2016 data. Expected values are shown in parenthesis. 'CS' in the model name stands for Charge Suppressed interaction model. Tracker analysis are done with data from the inner silicon detectors, time of flight (ToF) analysis with data from the muon spectrometers

## 3.1 Measurements of the properties of HSCP

Both tracker and muon system can measure the $p_T$ of the particle from the bending of the trajectories due to the magnetic field generated by the CMS solenoid. The information on the $\beta$ is computed with the energy loss $\left(-\langle\frac{dE}{dx}\rangle\right)$ in silicon detectors via the formula 3.1, which is valid for velocities much lower than the speed of light,

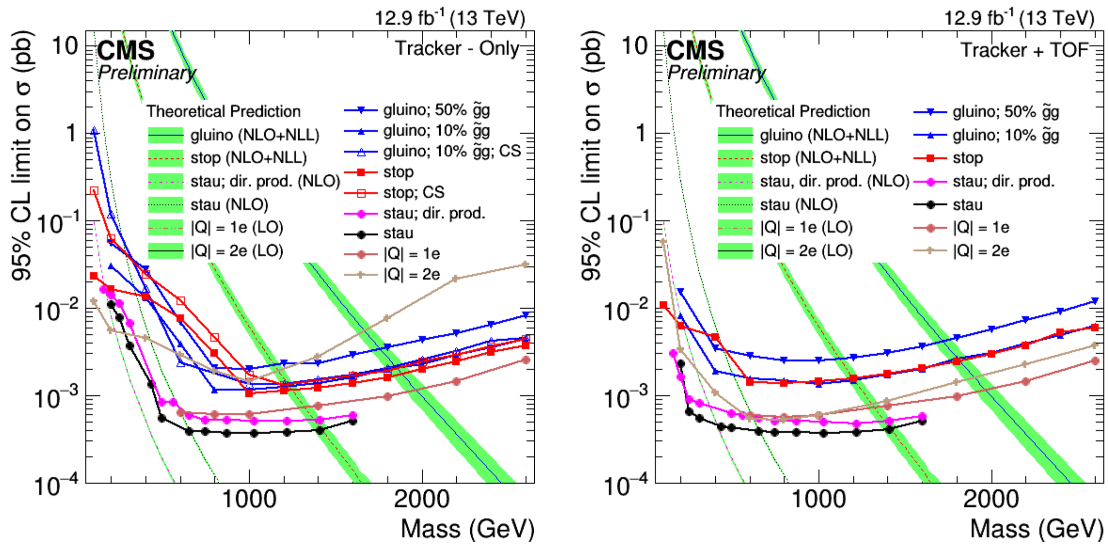


(a) Tracker-only analysis (b) Tracker + TOF analysis

Figure 3.3: Supersymmetric particle candidates: upper cross-section limits using CMS 2016 data. Theoretical predictions are shown in solid and dashed lines with green uncertainties. Points connected with lines represent the results obtained from the data analysis

$$-\langle\frac{dE}{dx}\rangle = Q^2\left(\frac{A}{\beta^2}+B\right) \tag{3.1}$$

where Q is the charge of the particle and A,B are parameters depending, for instance, on the material of the detector. The ToF information in the muon system gives an independent way to calculate the speed information with the equation 3.2, which depends on the time delays with respect to a particle traveling at the speed $c$ when crossing the muon subdetectors ($t_0$) and the track length ($L$).

$$\beta^{-1} = 1 + \frac{ct_0}{L} \tag{3.2}$$

Even if the three analysis are very different, they require high precision measurements in both the inner and the outer detectors, and the highest achievable number of collected events (see chapters 4,5 for a possible muon trigger improvement).
In the barrel region, the precision on the computation of beta depends strongly on the performance of the DT chambers.Therefore, it is essential to control and preserve the performance in terms of efficiency of the cells. This issue is critical especially for the future

upgrade of the LHC accelerator with the High Luminosity LHC project, when the dose absorbed by the DTs will be 10 times larger than considered in the initial design. All the final part of the thesis work will deal with this problem (see Chapter 7).

# Chapter 4

# The 2BX L1 Trigger for slow-moving particles

As shown in figure 3.2, the efficiency of the muon trigger is significant only for tracks with $\beta >\sim 0.6$. Indeed, for lower $\beta$ the delay of such tracks in the muon system becomes larger than 25 $ns$: the CMS muon trigger, tuned for prompt muons, identifies such tracks as originated at the subsequent BX and not at the correct one. In this case, the recorded event will not contain the information coming from the inner tracker[1] and will be rejected by the HLT. For R-hadron and gluinos the muon inefficiency at low beta is recovered with the missing energy. However, for stau pairs this specific trigger is not applicable and a different solution is needed.

In 2012 data taking, a specific muon trigger was implemented for searches of massive particles which considered two following BXs at a time. This was possible because the proton-proton interactions occurred every 50 $ns$. Since 2015, the LHC interaction frequency was doubled, reducing the time between two following bunch crossings to 25 $ns$, and the trigger used up to 2012 could not be employed any more.

Inspired by the solution of considering two BXs at a time, adopted in 2012, one of the two main topics of this thesis work has been focused on the study and the implementation of a new 2BX trigger algorithm for the CMS Level-1 Muon Barrel Trigger trying to extend the acceptance for slow-moving particles and in particular for Heavy Stable Charged Particles.

[1]For the tracker, only the data of the triggered BX are read out.

First, the performance of the DTs and the current L1 trigger chain for muons is considered, using di-muon final states coming from $Z^0$ boson decays. Than, an overview of the possible measurements for HSCPs with the CMS detector are shown, focusing on the triggers involving the muon spectrometer of the barrel in CMS. The performance of the current L1 muon trigger for slow-particles is considered to demonstrate the necessity for a new trigger algorithm, explaining how a 2BX Trigger works. The possible improvements in terms of number of triggered HSCP particles and the drawbacks for muons have been studied, using the CMS software for simulation and analysis (CMSSW).

## 4.1 The Muon Barrel performance with muons

All the muon barrel system with DT and RPC subdetectors is synchronized for muons originated in the interaction region and traveling through the detector at the speed of light. This means that a muon track should cross the four DT and RPC stations of the barrel at a relative $t_0 = 0\ ns$ time and the spread of the $t_0$ distribution around the zero value is defined as the resolution of the time identification. From the Time of Flight (ToF) measurements with the $t_0$ values, it is possible to calculate the speed of the particle ($\beta = v/c$) which has to be around $\beta = 1$ for muons. With the information about the $p_T$ from the offline reconstruction of the events, it is possible to find out all the main properties of the muons traversing the detector.

For the analysis of the performance of the DTs and the L1 muon barrel trigger for muons, the 2016 era H Z$\mu\mu$ sample has been selected. Since 2016, indeed, the TwinMux system began its operations, thus the new trigger chain was completed. The $Z^0 \rightarrow \mu\mu$ data sample contains offline reconstructed muons produced in pairs by the decay of the $Z^0$ boson. Their $p_T$ distribution is shown in figure 4.1.

After a selection of muons with $p_T > 20\ GeV/c$, the offline segments (tracks built from hits found in a single station) are associated to the reconstructed muons. Only segments with a valid $\phi$ coordinate and with at least 5 $\phi$ hits are considered. Subsequently, only muons with at least 3 segments are taken into account for the rest of the analysis. These requirements are necessary to have muons which can cross all the detector, giving good signal information and, also, these are the same properties that the trigger candidates must satisfy in order to be considered by the new 2BX trigger algorithm. Then the trigger superprimitives coming from the output of the TwinMux are associated to the segments to compare the time measurement provided by the two objects: BX and $t_0$ (2.3.1).

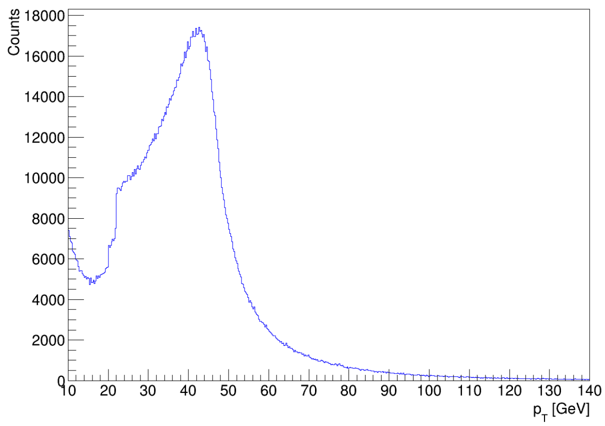


Figure 4.1: $p_T$ distributions for muons coming from a $Z^0$ decay in the 2016H LHC era.

The $t_0$ distribution is shown in figure 4.2 with a gaussian fit, which gives the spread of the distribution. The standard deviation of the gaussian ($\sigma$) is defined as the offline time resolution of the DT chambers and is equal to 2.1 $ns$, while online it amounts to one BX (25 $ns$). The comparison between online and offline can be seen in the plot in figure 4.3.

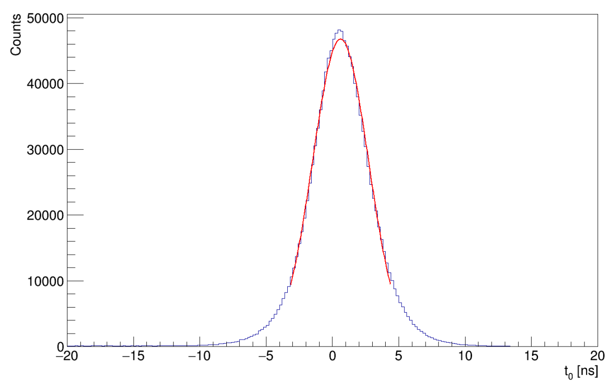


Figure 4.2: $t_0$ distributions and gaussian fit for $Z^0 \rightarrow \mu\mu$ muons with $p_T > 20\ GeV/c$. The standard deviation of the distribution is equal to equal to 2.1 $ns$ and it is defined as the offline time resolution of the DT chambers.

Using the ToF technique, knowing the distances among the stations and the $t_0$ times of the $\phi$ segments, the inverse of the velocities ($\beta^{-1} = c/v$) of the particles can be calculated through the equations 4.1 and 4.2.

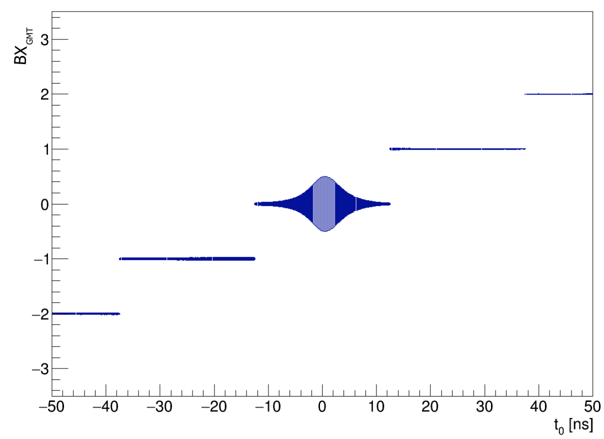


Figure 4.3: Trigger primitive BX compared to segment $t_0$ in a ROOT "BOX" plot for $Z^0 \rightarrow \mu\mu$ muons with $p_T > 20\ GeV/c$. (Each box size is proportional to the number of events in that bin.)

$$\beta^{-1} = \frac{\sum\limits_{i=1}^{4} (1 + ct_{0_i}/L_i) \cdot w_i}{\sum\limits_{i=1}^{4} w_i} \tag{4.1}$$

$$w_i = \left( \frac{\#\phi hits - 2}{\#\phi hits} \right) \cdot L_i^2 \tag{4.2}$$

where the sums go from the first to the last station providing valid segments, $L_i$ is the length of the trajectory before reaching the $i-th$ station and $w$ is the weight, in which the numerator $(\#\phi hits - 2)$ takes into account the 2 needed degrees of freedom to compute the fitting $\phi$ segment parameters.

The calculation of the inverse of beta is preferred to beta because the error propagation from the $t_0$ uncertainties is linear. For ultra-relativistic muons the inverse of beta is distributed around the value $\beta^{-1} = 1$, as shown in the plot in figure 4.4. The standard deviation of the distribution, computed as the $\sigma$ of the gaussian fit, representing the resolution in $\beta^{-1} = 1$ of the DT chambers results $0.0646 \pm 0.0003$, in agreement with the value 0.065 obtained in [23].

In figures 4.5a and 4.5b, the plots of $t_0$ and $\beta^{-1}$ as a function of $\eta$ are presented. From these plots it is clear that the calibration of the $t_0$ is not perfectly computed and it propagates

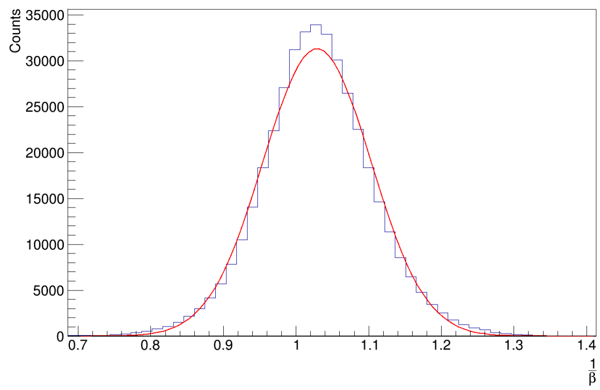


Figure 4.4: Inverse of beta distribution for $Z^0 \rightarrow \mu\mu$ muons with $p_T > 20$ $GeV/c$.

to the $\beta^{-1}$ calculation. This small issue has been reported to the CMSDToffline team.

## 4.2 The muon system performance with simulated HSCP events

In section 4.1, an overview has been given on the performance of the CMS barrel muon detectors for muons. In this section the performance will be studied using MonteCarlo samples of Heavy Stable Charged Particles, showing the present L1 trigger chain shortcomings with slow-moving particles. All the progresses done in the study and the implementation of the new 2BX Trigger will be described.

### 4.2.1 HSCP samples for the analysis

To study the present L1 trigger chain performance with HSCP, it was not possible to use the available samples for the HSCP analysis, because the emulation of the latest L1 trigger hardware developments was not included.
With the help of Luigi Guiducci, Carlo Battilana and Federica Primavera (University and INFN Bologna), the emulated trigger algorithms in CMSSW 8_0_21 were updated to the hardware configuration installed since 2016. The components that were modified are highlighted in red boxes in figure 4.6. The most important intervention was the substitution of the old simulator for the TwinMux with a new emulator, created by Giannis Flouris, which was meant only for private tests and now it is working with all the rest of the trigger chain.

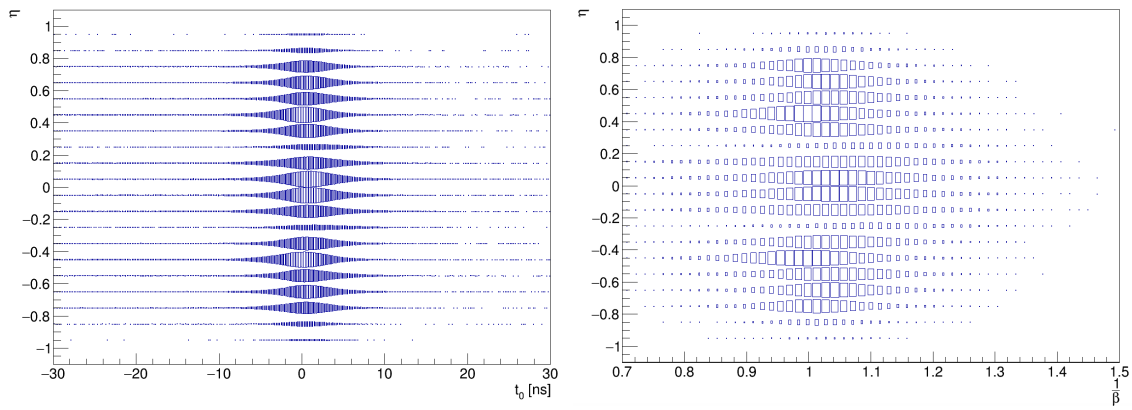


(a) Reconstructed muon $\eta$ position versus $t_0$ of the associated segments.

(b) Reconstructed muon $\eta$ position versus $\beta^{-1}$.

Figure 4.5: "BOX" plots of the muon properties as a function of the $\eta$ position in the DT subdetectors. The interval $[-0.9; 0.9]$ in the $\eta$-axis corresponds to the $\eta$ range covered by at least three the DT stations.

Two samples, the Pair Produced staus with masses of 651 and 1599 $GeV/c^2$, were produced simulating the updated trigger chain. The choice of the staus was motivated by the reason that the particles had to be lepton-like to be sure that they were charged for the entire path in crossing the CMS detector to leave ionization signals in the gaseous muon detectors. The two values for the masses have been opted to compare the results and the improvements brought by the new trigger algorithm for particles with different velocities; the heavier they are, the slower they travel through the detector (figure 4.7a). Moreover, for larger masses, they are produced in $\eta$ regions around the transverse plane ($\eta$ closer to 0), so the probability to cross the detector in the barrel region is higher (figure 4.7b).

The main properties of the two samples of M $=$ 651 $GeV/c^2$ and M $=$ 1599 $GeV/c^2$ stau particles, selected for the analysis and the evaluation of the new trigger algorithm, are shown in figure 4.8. The samples, each containing 30 thousand events corresponding to 60 thousand stau or anti-stau particles, have been produced with a personal modified version of CMSSW 8_0_21 obtaining as output a ROOT file (usually known as Root-ple). The analysis has been conducted using ROOT macros in the CERN ROOT data analysis framework.

From the relativistic formula of the momentum $|\vec{p}| = m\gamma|\vec{v}| = m\gamma\beta c$, the mass formula can be obtained, resulting the equation 4.3. The distribution of the masses calculated with $p_T$,

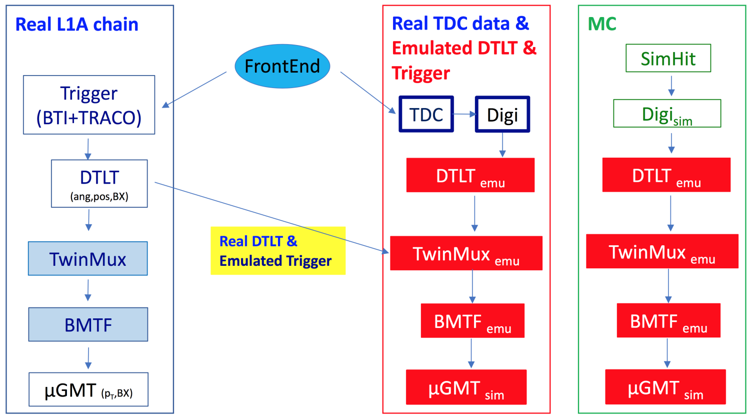


Figure 4.6: Block diagrams of real and emulated L1 Muon Barrel Trigger chain for the Drift Tube Chambers. Components in red boxes have been updated to the present hardware configuration (since October 2016). Real signals from the FrontEnd of the detectors or simulated hits are sent to the Drift Tubes Local Trigger (DTLT), which reconstructs roughly the track segments and delivers the trigger primitives to theTwinMux. In the TwinMux the primitives are compared with the ones coming from the RPCs and the result is given to the Barrel Muon Track Finder (BMTF). After the online reconstruction of the track, the muon candidate is sent to the Global Muon Trigger for the final sorting before being forwarded to the Global Trigger.

$p_z$ and $\beta^{-1}$ is shown in figure 4.9. The width of the distribution depends on the uncertainties on the components of $\vec{p}$ and on the time resolution($\sigma_{t_0}$). The relative uncertainty for the mass results $\sigma_m/m \approx 10\%$.

$$m = \sqrt{(p_T^2 + p_z^2)\left(\frac{1}{\beta^2} - 1\right)} \tag{4.3}$$

### 4.2.2 Present L1 Trigger performance

The present L1 Trigger performance has been analyzed for the two samples of M = 651 $GeV/c^2$ and M = 1599 $GeV/c^2$ stau particles produced. Starting from reconstructed muons in the barrel region, the tracks have been selected requiring at least 3 valid segments with more than 5 hits each. The Global Muon Trigger candidate has been associated to the reconstructed muon geometrically, matching the $\phi$ coordinate ($\Delta\phi < 10°$). As described

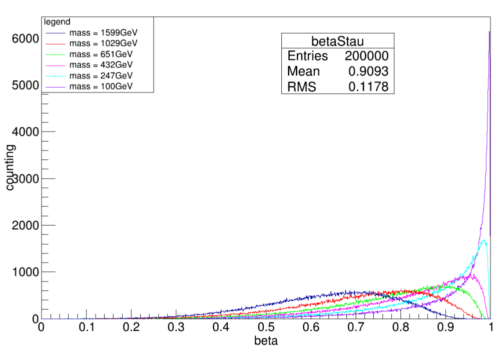


(a) stau and anti-stau $\beta$ distribution for different mass samples.

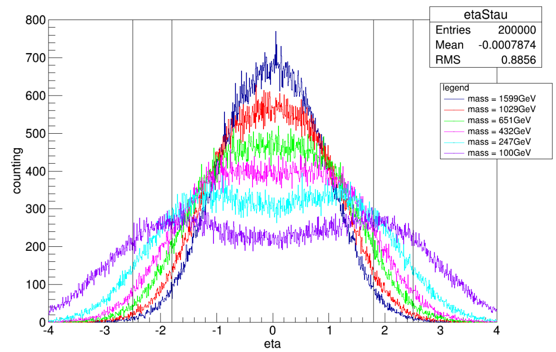


(b) stau and anti-stau $\eta$ distribution for different mass samples.

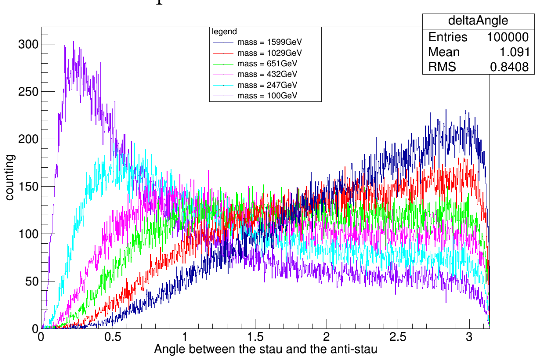


(c) Angle between the two pair-produced stau and anti-stau for different mass samples.

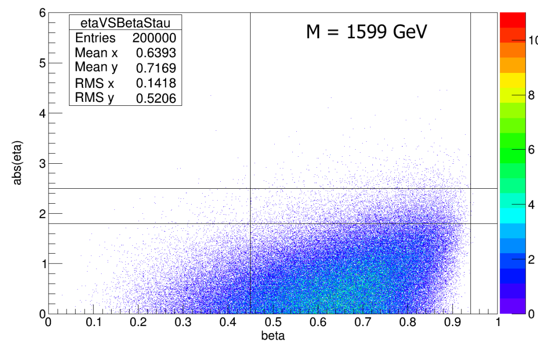


(d) $\eta$ vs $\beta$ distribution for stau and anti-stau particles with a mass of 1599 $GeV/c^2$.

Figure 4.7: Velocity and angular distributions for pair-produced stau and anti-stau particles of different masses. Plots from [24].

in the section dedicated to the CMS muon trigger (section 2.4), the GMT BX is given to the trigger candidate when at least 2 associated TwinMux superprimitives are found at the same BX. The distribution of the GMT BX as a function of the $\beta$ of the muon are shown in figure 4.10. From these distributions for the two different masses of staus, it can be inferred that heavier is the particle, more probable is to be triggered at higher BXs. Indeed, the population of tracks with a BX = 1 for the 1599 $GeV/c^2$ stau sample is much larger than the one corresponding to the mass equal to 651 $GeV/c^2$.

At the HLT level, the final part of the trigger chain, the muon tracks cannot be reconstructed starting from the inner tracks if the BX information doesn't corresponds in all the different parts of the detector. Indeed, due to the fact that the distance of the inner tracker is

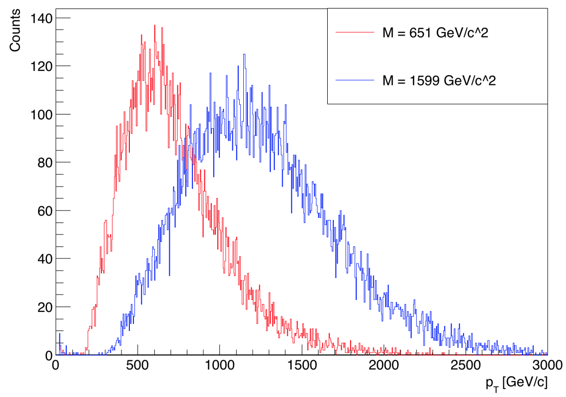


(a) $p_T$ distribution for samples of masses 651 $GeV/c^2$ (red) and 1599 $GeV/c^2$ (blue).

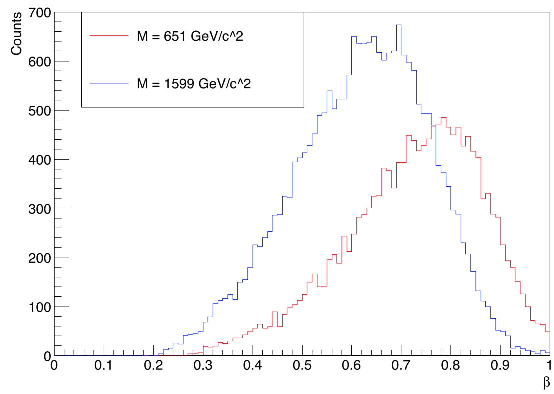


(b) $\beta$ distribution for samples of masses 651 $GeV/c^2$ (red) and 1599 $GeV/c^2$ (blue).

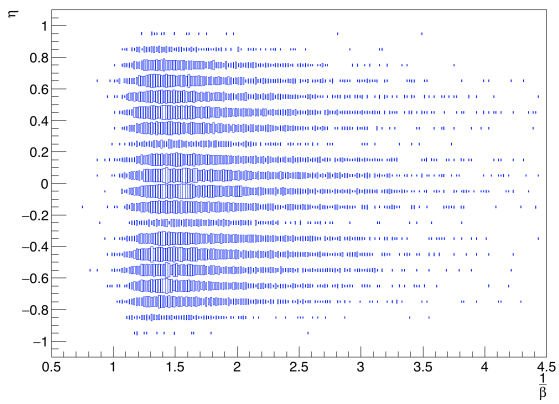


(c) $\eta$ vs $\beta^{-1}$ distribution for samples of mass 1599 $GeV/c^2$.

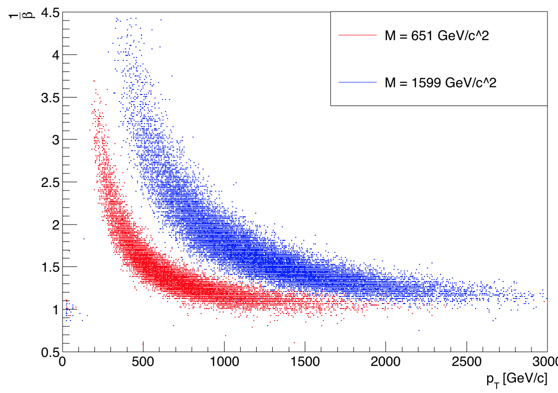


(d) $\beta^{-1}$ vs $p_T$ distribution for samples of masses 651 $GeV/c^2$ (red) and 1599 $GeV/c^2$ (blue).

Figure 4.8: Velocity and angular distributions for pair-produced stau and anti-stau particles of different masses. Plots from [24].

significantly lower than the one of the outer gaseous detectors, in the core part the HSCP track is detected at BX=0, while in the muon part it can generate a L1 trigger at the following BX (BX=1). This situation leads to the rejection of the event by the HLT, with the loss of the HSCP candidate.

As a result, the only tracks, that can be triggered by the L1 chain, are those identified at the BX = 0 in every part of the detector. The efficiency of triggering the candidates at a BX = 0 as a function of the $\beta$ of the particle is presented in figure 4.11, for the two stau

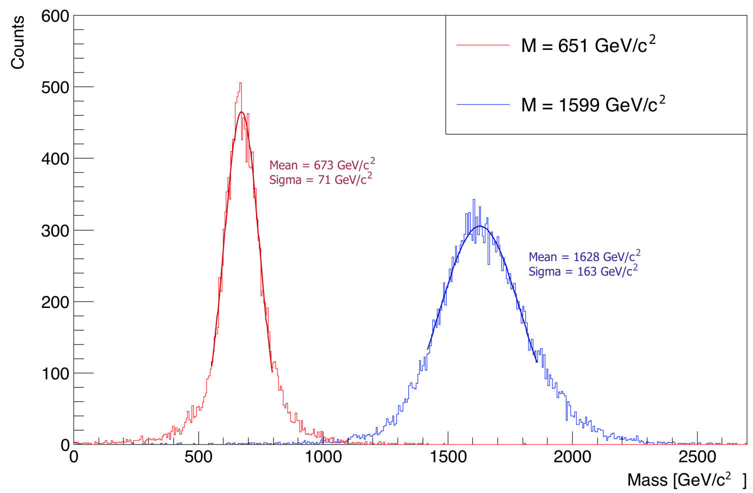


Figure 4.9: Mass distribution with variables from the muon reconstruction for stau samples of masses 651 $GeV/c^2$ (red) and 1599 $GeV/c^2$ (blue).

samples, with superimposed BX distribution. Interval of $\beta = 0.01$ have been considered for the computation of the efficiency, which is defined by the ratio between the number of candidates with BX $= 0$ and the total number if candidates in the same interval.
From the two plots, it is observed that the efficiency plateau with a value of 100% starts at $\beta = 0.7$, while under $\beta = 0.5$ the efficiency is less than 10%; it goes to 0 for $\beta < 0.45$.
Trigger efficiency as a function of the $\eta$ coordinate is shown in 4.12, where the two empty spaces for the cables and the equipments ("cracks") between the wheel 0 and the wheels $\pm 1$ ($0.25 < |\eta| < 0.45$) appear as a moderately lower efficiency with respect to the almost constant value for the other $\eta$ intervals.
From a fit with a constant function in the efficiency vs $\eta$ plot, the total efficiency of the present L1 trigger for slow-moving particles results $82.3 \pm 0.3$ % for staus with a mass of 651 $GeV/c^2$ and $59.2 \pm 0.3$ % for a mass of 1599 $GeV/c^2$.

## 4.3 The 2BX L1 Trigger

In this section, the algorithm aimed at recovering the muon trigger candidates with trigger primitives at a late BX in outer stations to identify slow-moving particles is described, and tested, to check the possible improvements on the trigger efficiency.

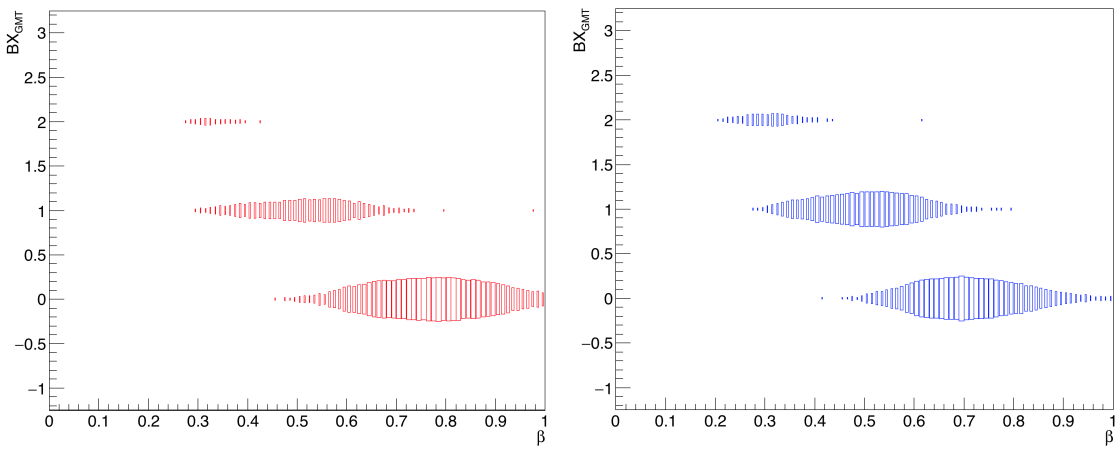


(a) M = 651 $GeV/c^2$ stau sample. (b) M = 1599 $GeV/c^2$ stau sample.

Figure 4.10: "BOX" plots of the BX distribution of the trigger candidates as a function of the calculated $\beta$ from the reconstructed HSCP tracks.

### 4.3.1 2BX trigger: working principles

The muons or the charged particles crossing the muon detectors leave ionization signals in the stations. For each DT and RPC station, the primitives are sent to the TwinMux where the superprimitives are created. The main properties of the superprimitives are the numbers for the chamber identification, the $\phi$ position, the $\phi_B$ angle, the BX, the $\phi$ quality and the RPCbit. The $\phi$ quality ranges from 0 to 7, where 6 represents the 8 $\phi$ hits (HH). At the beginning of the thesis work, the RPCbit was set to 0 if the DT superprimitive was left untouched, and to 1 when its BX was shifted by the check with the RPC primitive. For this analysis it is not important to know whether the DT and RPC objects forming the superprimitives were at the same BX or at a different one, but rather to select the class of superprimitive that can ensure a high BX identification capability. So, we only need to check if the superprimitive BX corresponds to the BX of a RPC hit; while, if no RPC match was found, and the superprimitive is simply a DT trigger segment, we request that this segment has the maximum DT quality, HH. Thus, the behavior of the RPCbit was changed in a new firmware, in which the value 1 is set for all DT-RPC matches, regardless of the possible time shift applied to the DT.

Focusing on the candidate superprimitives, output of the TwinMux, there are various possible BX-schemes, formed by the BX on the 4 muon barrel stations. Some examples are given

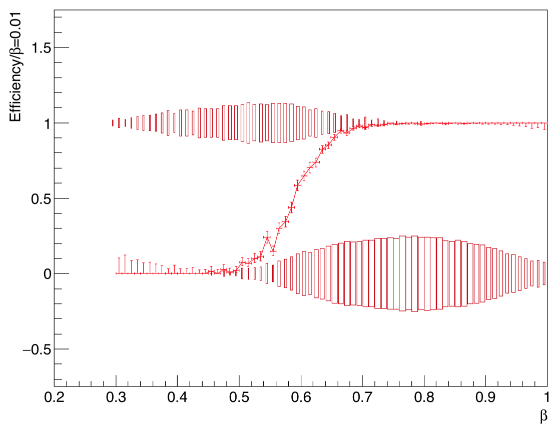


(a) M = 651 $GeV/c^2$ stau sample.

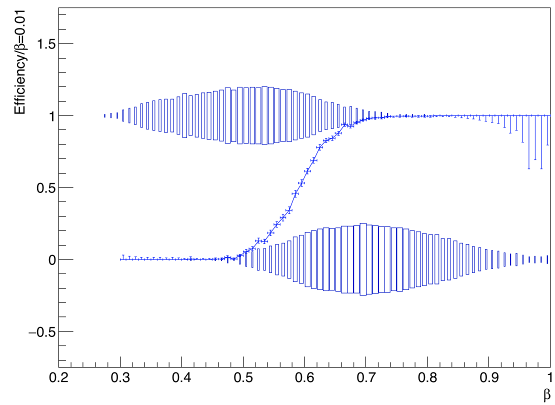


(b) M = 1599 $GeV/c^2$ stau sample.

Figure 4.11: Plots of the present L1 trigger efficiency for BX = 0 candidates with superimposed BX distributions as a function of the calculated $\beta$ for the respective reconstructed HSCP tracks.

in figure 4.13, where the green highlights refers to the superprimitives which contribute to the candidate BX given by the GMT, represented by the blue arrows on the top of the schemes.

While all the present L1 trigger chain considers only one BX at a time, the new 2BX trigger algorithm checks at 2 consecutive BXs, looking for the BX-schemes which have the first valid superprimitive at the BX = X and the other ones at the BX = X+1 as shown in figure 4.14. The condition required for the superprimitive in the first station is either to have a HH $\phi$ quality or the RPCbit= 1. This ensures with a large probability (99.5%) that the BX information is correct and not given by a possible pre-trigger.

For the special BX-schemes, the 2BX trigger algorithm acts shifting the BX of all the superprimitives belonging to a trigger candidate to BX = X. The result is the increasing of the number of HSCP candidates accepted by the L1 trigger chain, moving their BX from 1 to 0. A potential side effect can arise when a prompt muon results in a pre-trigger (trigger primitive at BX = $-1$) in the first station, with a probability of 2% [13]. In such a case, the prompt muon would activate the 2BX algorithm, generating a muon trigger candidate at the wrong BX and resulting in the the loss of the event at the HLT. To reduce this unwanted drawback of the algorithm, a selection on the $\phi_B$ of the superprimitives is done. Indeed, muons usually have a lower $p_T$ than the HSCP particles, producing a larger $\phi_B$ in

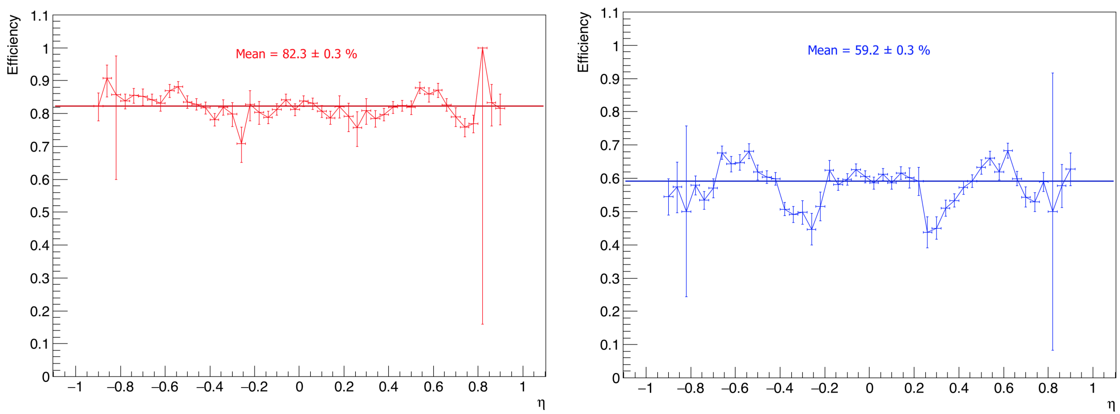


(a) M = 651 $GeV/c^2$ stau sample. (b) M = 1599 $GeV/c^2$ stau sample.

Figure 4.12: Plots of the present L1 trigger efficiency for BX = 0 candidates with superimposed BX distributions as a function of $\eta$ coordinate for the respective reconstructed HSCP tracks.

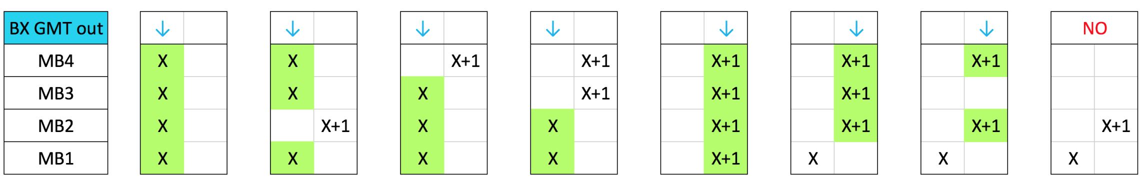


Figure 4.13: Examples of possible superprimitive BX schemes. Blue arrows represent the BX of the candidate at the output of the GMT. The green boxes are the superprimitives contributing to the assignment of the BX to the track. The last example is given to show that when there are only two superprimitives with different BXs, the particle track is not triggered.

the muon station due to the fact that the radius of curvature of the trajectory is proportional to momentum of the particle, expressed by the formula $\rho = \frac{p}{qB}$. The maximum value for the $\phi_B$ angle of the superprimitive to be taken into account by the algorithm has been fixed to 3°, maximizing the benefits for HSCP and minimizing the interventions on muon candidates with pre-triggers.

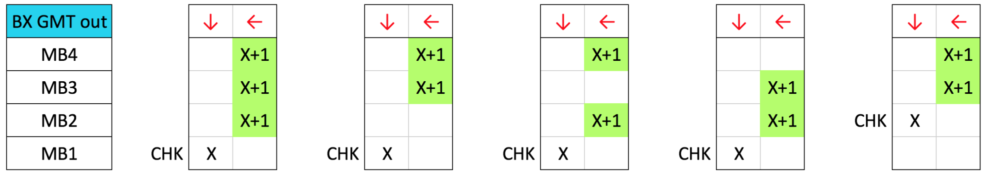


Figure 4.14: Special superprimitive BX schemes considered by the new 2BX trigger algorithm. The first station with a valid superprimitive has BX = X and an HH quality or a RPCbit = 1 (CHK → conditions) and the others are at BX = X+1. The red arrows indicate the shift of all the superprimitives to BX = X.

### 4.3.2 Results from analysis and simulation

#### Improvements for HSCP analyzing the MC samples

As a first analysis, the 2BX trigger has been implemented using reconstructed tracks (offline point of view) an the possible improvement in the selection of HSCP candidates has been estimated. The number of the total tracks has been computed along with the ones having at least three valid segments and finally the ones with a special BX-scheme that would activate the new algorithm. The results for the two stau samples are shown in the histograms in figure 4.15.

For the M = 651 $GeV/c^2$ particles, the number of special BX-schemes related to the total number of reconstructed tracks is 1.1%, while compared to the tracks with at least 3 segments, the ratio is 2.7%. For the mass 1599 $GeV/c^2$, the two ratios become respectively 2.1% and 4.7%.

To conduct a more unbiased analysis due to the selections and correlations between trigger primitives and reconstructed tracks, the improvements with the 2BX algorithm have been tested starting from the superprimitives recorded in the events. An additional advantage of this analysis is the online trigger point of view, which is more close to the subsequent hardware simulation and implementation that work only with input information given by the TwinMux. The trigger candidates have been composed event by event with coherent superprimitives and the BX scheme of each candidate has been checked for the 2BX trigger requirements. In figure 4.16 the number of candidates that would activate the dedicated algorithm is shown.

For the M = 651 $GeV/c^2$ stau particles, the ratio between the number of special BX-schemes and the candidates with at least 3 superprimitives is 3%. For the mass 1599

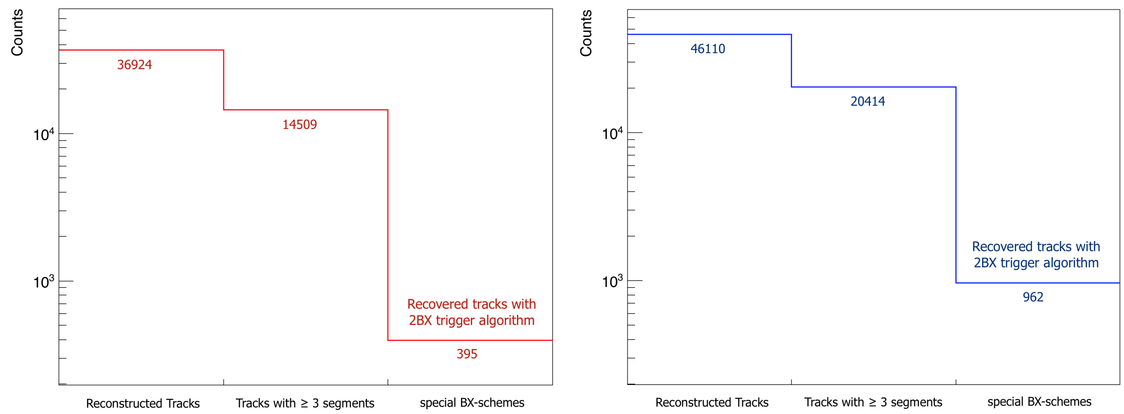


(a) M = 651 $GeV/c^2$ stau sample.

(b) M = 1599 $GeV/c^2$ stau sample.

Figure 4.15: Number of reconstructed tracks recovered with the introduction of 2BX trigger. The first bin represents the total number of valid reconstructed tracks, the second one contains the number of tracks with at least 3 valid segments and the last bin is the number of special BX-schemes that would activate the new algorithm.

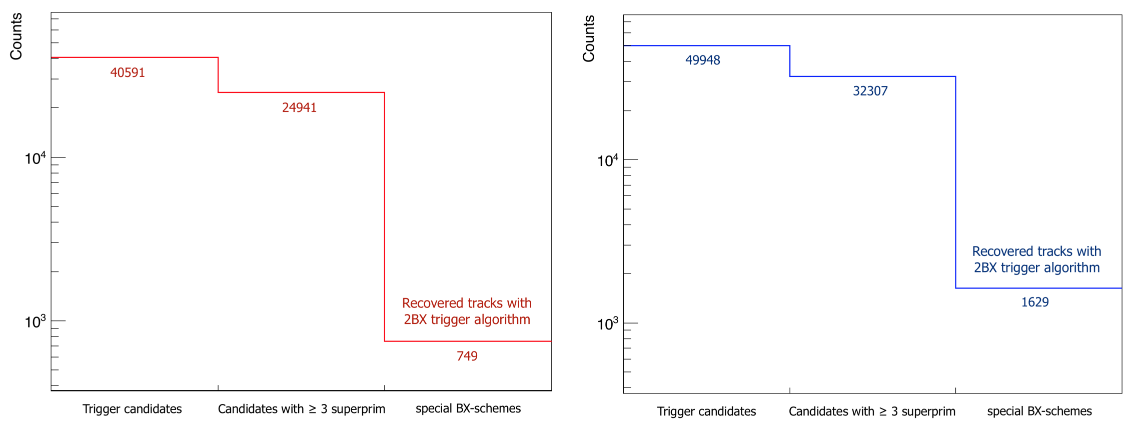


(a) M = 651 $GeV/c^2$ stau sample.

(b) M = 1599 $GeV/c^2$ stau sample.

Figure 4.16: Number of trigger candidates recovered with the introduction of 2BX trigger. The first bin represents the total number of candidates, the second one contains the number of candidates with at least 3 valid superprimitives and the last bin is the number of special BX-schemes that would activate the new algorithm.

$GeV/c^2$, the ratio becomes 5%. These results are slightly higher than the ones obtained with the analysis considering the reconstructed tracks, mainly because of the selections in all the trigger chain and in the reconstruction which are not present in this particular study.

Considering the reconstructed tracks, for which all the offline properties are available ($t_0$, $\eta$, etc.), the same plots as in subsection 4.2.2 have been produced, considering the action of the 2BX trigger in moving the $\mathrm{BX}_{GMT} = 1$ to 0 for the special BX-schemes. The comparison of the results and the improvement introduced are shown in figures 4.17 and 4.18. The $\beta$ interval where is located the improvement is the transition region between $\mathrm{BX}_{GMT} = 0$ and $\mathrm{BX}_{GMT} = 1$, corresponding to $0.45 < \beta < 0.7$, as it was expected. In $\eta$ coordinate, the efficiency gain is almost uniformly distributed.

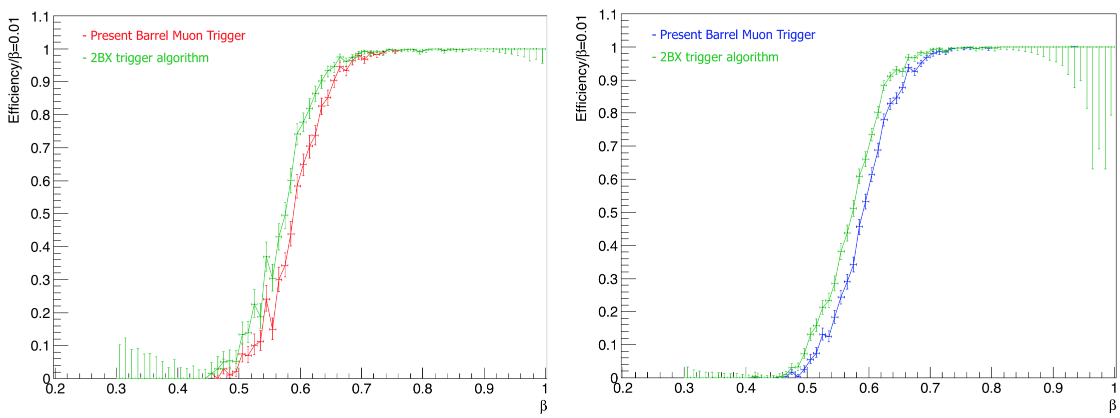


(a) M = 651 $GeV/c^2$ stau sample.

(b) M = 1599 $GeV/c^2$ stau sample.

Figure 4.17: Trigger efficiency as a function of $\beta$ for reconstructed tracks of simulated stau particles. Comparison between present L1 trigger efficiency and efficiency with the implementation of the new 2BX trigger algorithm for two different mass samples.

The absolute improvements for the tracks with $\geq 3$ segments are 2.7% and 4.8% for the samples with masses 651 $GeV/c^2$ and 1599 $GeV/c^2$ respectively, which means a relative improvement with respect to the present trigger performance of 3.3% and 8.1%.

## Results of the emulations of the 2BX trigger in CMSSW

The following step, after the evaluation of the possible improvements when introducing the 2BX trigger, is the implementation of the algorithm in a private version of the CMSSW 8_0_21 software. The code has been inserted into the TwinMux emulator considering as input the output of this component of the L1 barrel muon trigger chain. A brief scheme

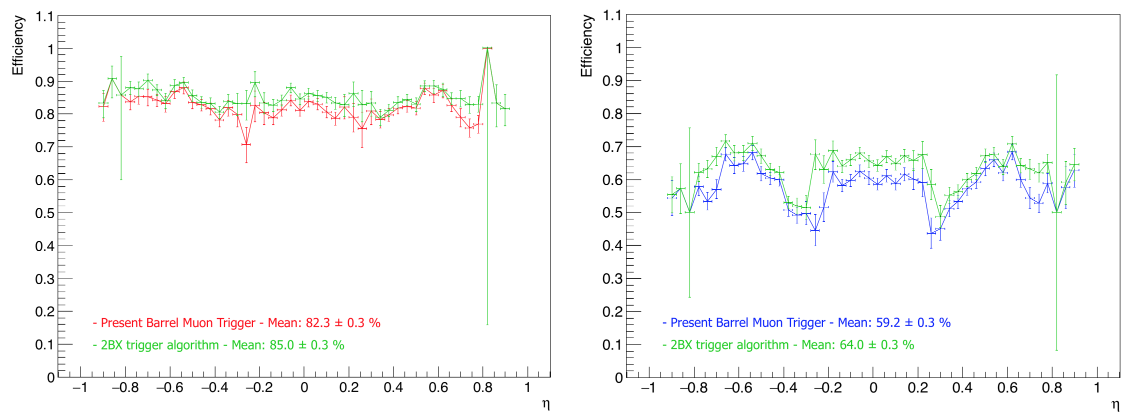


(a) M = 651 $GeV/c^2$ stau sample. (b) M = 1599 $GeV/c^2$ stau sample.

Figure 4.18: Trigger efficiency as a function of $\eta$ for reconstructed tracks of simulated stau particles. Comparison between present L1 trigger efficiency and efficiency with the implementation of the new 2BX trigger algorithm for two different mass samples.

of the implemented algorithm in the simulation is depicted in figure 4.19. First, the 8 primitives (Higher Quality and Lower Quality) from the front-end (minicrates) of 4 stations of a single sector are sent to the TwinMux and are compared with the RPC primitives of the barrel region. Then a check on the $\phi_B$ is performed to select the superprimitives with an angle less than 3°. The $i-th$ and $j-th$ superprimitives are correlated with a condition on the $\phi$ position ($|\Delta\phi_{ij}| < 2.5°$) and "candidates" are obtained. The BX-schemes of the candidates are compared to the special BX-schemes and if the conditions required for the first superprimitive (HH quality or RPCbit = 1) are satisfied the BXs of all the superprimitives belonging to the candidate are shifted to the BX of the first candidate. Finally all the superprimitives modified or untouched are sent to the input of the Barrel Muon Track Finder.

To check the results of such implementation, the two HSCP samples used for the initial production for the analysis have been simulated another time with the modification of the TwinMux algorithm. The same 30 thousand events for each of the stau sample with mass M = 651 $GeV/c^2$ and M = 1599 $GeV/c^2$ have been generated and analyzed with the same programs as for the present trigger performance. The results of the analysis considering the offline reconstructed tracks are shown in figures 4.20 and 4.21.

The weighted mean values for the trigger efficiency for tracks with at least three segments of the two stau samples of masses 651 $GeV/c^2$ and 1599 $GeV/c^2$ are respectively $84.8 \pm 0.3\%$

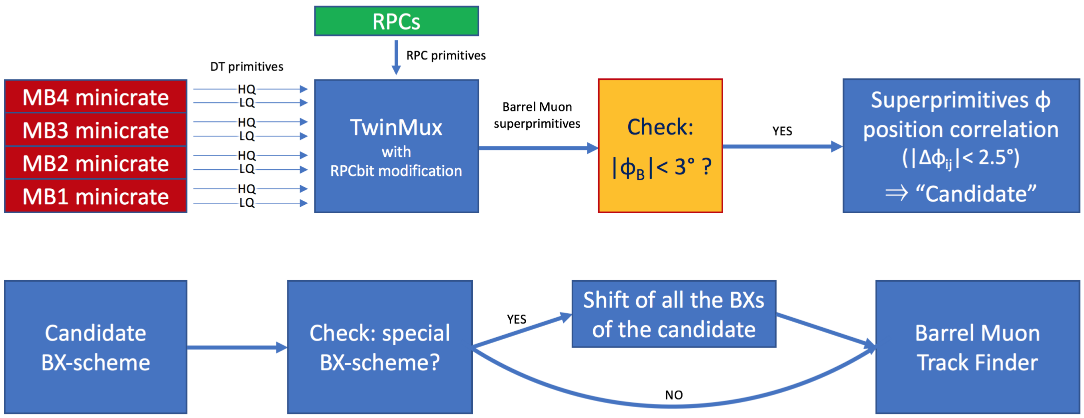


Figure 4.19: 2BX trigger algorithm implemented in the TwinMux emulator of a private version of CMSSW 8_0_21 software.

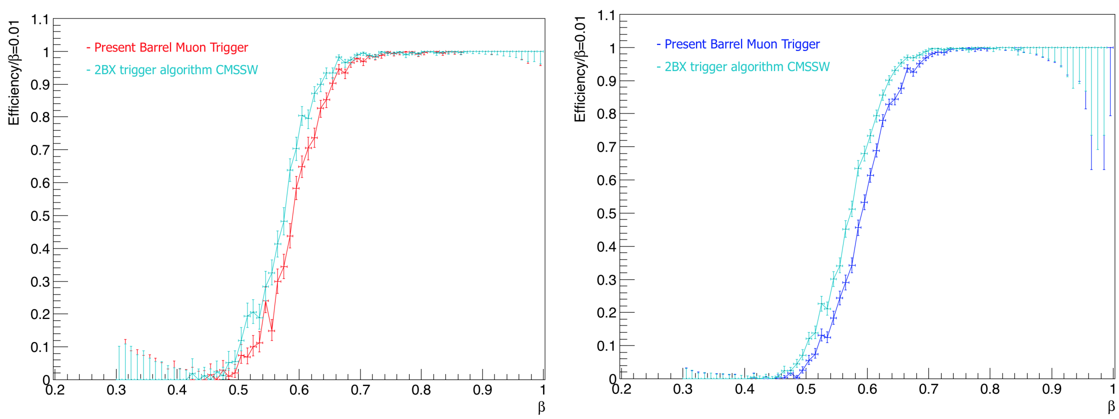


(a) M = 651 $GeV/c^2$ stau sample.

(b) M = 1599 $GeV/c^2$ stau sample.

Figure 4.20: Trigger efficiency as a function of $\beta$ for reconstructed tracks of simulated stau particles. Comparison between present L1 trigger efficiency and efficiency with the implementation in CMSSW of the new 2BX trigger algorithm for two different mass samples.

and $64.0 \pm 0.4\%$, giving absolute improvements of 2.5% and 4.8%. These values are in agreement with the ones obtained from the offline analysis.

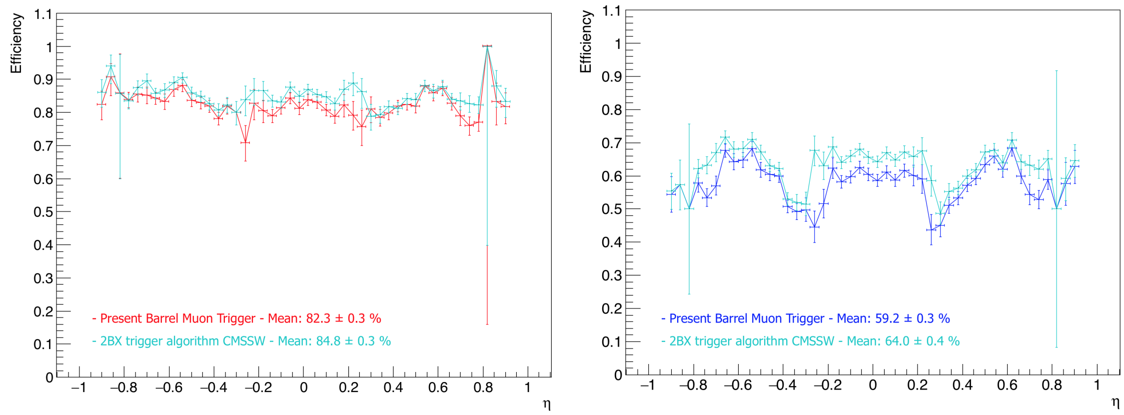


(a) M = 651 $GeV/c^2$ stau sample. (b) M = 1599 $GeV/c^2$ stau sample.

Figure 4.21: Trigger efficiency as a function of $\eta$ for reconstructed tracks of simulated stau particles. Comparison between present L1 trigger efficiency and efficiency with the implementation in CMSSW of the new 2BX trigger algorithm for two different mass samples.

## Potential drawbacks for prompt muons

The implementation of a 2BX trigger in the L1 muon barrel trigger chain would give considerable improvements in triggering slow-moving particles. However, it brings also small drawbacks for muons traveling at the speed of light. In figure 4.22 the action of the new algorithm is depicted, showing a shift of the candidate BX from 0, which is supposed to be the correct one, to $-1$ in presence of a pre-trigger that satisfies the requirements for the first superprimitive, leading to the loss of the muon track.

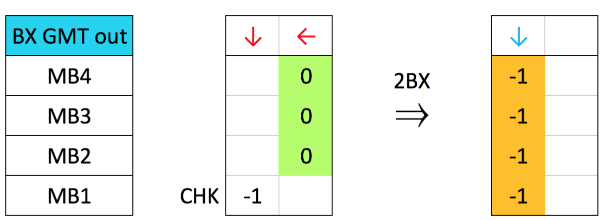


Figure 4.22: Examples of a muon superprimitive BX scheme with a pre-trigger in the first station. The required conditions (CHK) for the innermost superprimitive are an HH quality or a RPCbit = 1. The red arrows indicate the shift of all the superprimitives to BX = -1, leading to a $BX_{GMT} = -1$.

To compute the number of tracks that could be lost because of the activation of the 2BX trigger algorithm, the same 1 million events of the 2016 era H $Z^0 \rightarrow \mu\mu$ sample have been selected as for the initial study of the performance of the muon barrel system with muon particles. The results of the analysis, identical to the one conducted for the HSCPs, considering reconstructed tracks (offline point-of-view) and superprimitives (online point-of-view) are shown in figure 4.23.

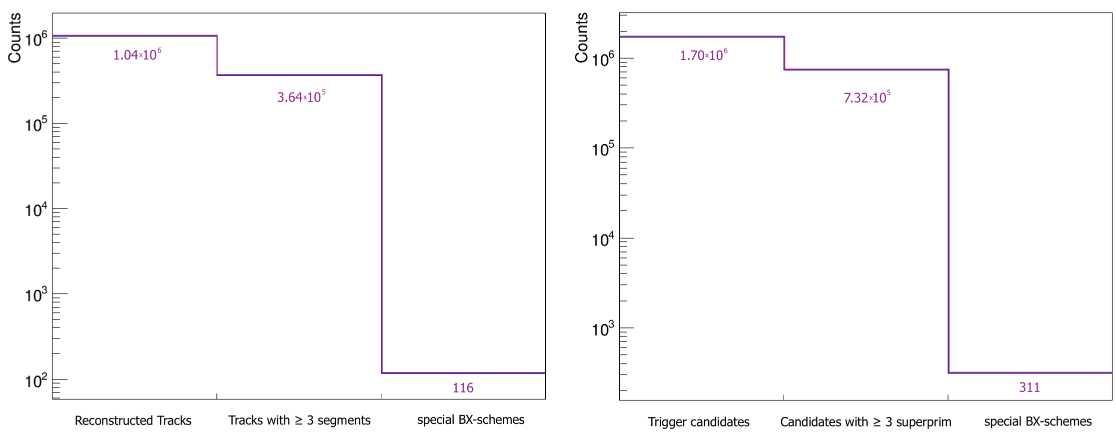


(a) Offline reconstructed muon tracks. (b) TwinMux superprimitives only.

Figure 4.23: Number of muon tracks (candidates) lost with the introduction of the 2BX trigger in the muon barrel system. The first bin represents the total number of valid reconstructed tracks (candidates), the second one contains the number of tracks (candidates) with at least 3 valid segments (superprimitives) and the last bin is the number of muons with a pre-trigger in the innernmost station that would activate the new algorithm.

The ratio between the number of reconstructed muon tracks shifted to $\mathrm{BX}_{GMT} = -1$, which can be lost in the trigger chain, and the number of tracks with at least 3 valid segments is 0.03%. Considering the total number of valid tracks the ratio becomes 0.01%. Only looking at the TwinMux superprimitives, the two percentages are 0.04% and 0.02% respectively.

All the results obtained in the analysis and simulations of the improvements and drawbacks of the 2BX L1 trigger for the muon barrel system have been summarized in figure 4.24.The percentages refer to the ratio between the number of tracks (candidates) activating the 2BX algorithm and the number of tracks (candidates) with at least 3 valid segments (superprimitives).

| | Improvements for HSCPs | | Drawbacks for muons |
|---|---|---|---|
| | staus M = 651 GeV/$c^2$ | staus M = 1599 GeV/$c^2$ | muons M = 105.7 MeV/$c^2$ |
| Analysis of offline reconstructed tracks | + 2.7 % | + 4.7 % | - 0.03 % |
| Analysis of TwinMux output: superprimitives | + 3 % | + 5 % | - 0.04 % |
| Implementation in TwinMux emulator of CMSSW | + 2.5 % | + 4.8 % | |

Figure 4.24: Summary table of the improvements and drawbacks for the implementation of the 2BX trigger in the L1 muon barrel trigger chain.

# Chapter 5

# Hardware implementation of the 2BX L1 Trigger

Once the performance of the L1 muon barrel trigger with the 2BX algorithm was evaluated and tested using the emulator software, the hardware implementation has been prepared and successfully executed during the Summer Student Programme at CERN. The most conservative and feasible operation to carry out in the L1 trigger chain is the implementation of the algorithm directly in the TwinMux board, adding the new instructions to the firmware of the FPGA. Even though this implementation has the disadvantages that the TwinMux works only with primitives received by one sector of one wheel and that it is impossible to have information on the $\eta$ position because the TwinMux operates separately for the $\phi$ and $\eta$ coordinates, it is convenient to begin modifying the behavior of this component (the improvements are shown in figure 5.1). The advantages are that it is relatively simple and it can be conducted on a spare board having zero impact on the rest of the CMS system. We can consider this an initial evaluation test of the algorithm implementation. A full implementation will have to be developed for the Barrel Muon Track Finder modules, that can build muon trigger candidates with all available stations also in cases where the muon trajectory crosses sector boundaries.

The first operation was to define the simplest algorithm to be implemented on the FPGA. Indeed, strict requirements in terms of execution time and complexity of operations are fixed for a pipeline mode trigger; every calculation must be carried out in less than 25 $ns$. To be considered by the 2BX trigger, the $i-th$ and $j-th$ superprimitives, coming from the $i$ and $j$ muon stations, have to fulfill the following conditions:

- Highest quality (HQ) superprimitive for each station
- $|\phi_B| < 3°$, corresponding to a value of $|\phi_B| < 27$ with a 10-bit precision on $\phi_B$
- $|\Delta\phi_{i,j}| < 2.5°$, corresponding to a value of $|\Delta\phi_{i,j}| < 140$ with a 12-bit precision on $\phi$
- Special BX-scheme, depicted in figure 4.14
- Innermost superprimitive with HH quality or BX confirmed by RPCs (RPBbit = 1)
- No other HQ superprimitives in the outer station at the first of the two BXs

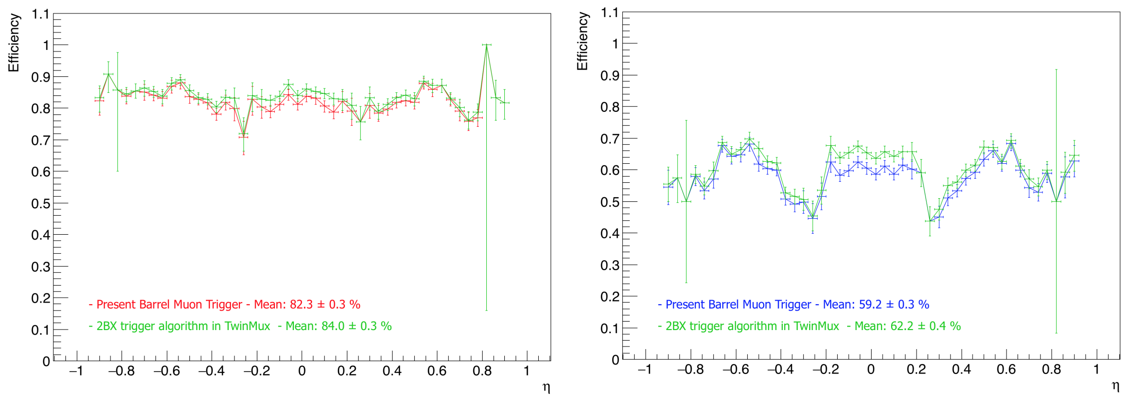


(a) M = 651 $GeV/c^2$ stau sample.

(b) M = 1599 $GeV/c^2$ stau sample.

Figure 5.1: Trigger efficiency as a function of $\eta$ for reconstructed tracks with $\geq$ 3 valid segments of simulated stau particles. Comparison between present L1 trigger efficiency and efficiency with the implementation of the new 2BX trigger algorithm on the TwinMux boards for two different mass samples.

If the superprimitives have the listed properties, all the incoming superprimitives are sent to the output at the BX of the first valid superprimitive, so that the ones from the outer stations are anticipated of 25 $ns$. This operation has to be signaled to the entire trigger chain and especially to the BMTF, possibly with a single bit set to 1 in case of activation of the algorithm.

## 5.1 TwinMux simulation and testbench

Once the suitable algorithm for the 2BX trigger was defined, it was written in the VHDL programming language and tested with the Vivado simulation software created by XILINX,

the FPGA producer. The setting selected for the simulation were "Virtex-7" for the product family and the product specific name "xc7vx330tffg1761-3".
Usually the testbenches for the TwinMux are done with a very limited number of ad-hoc created BX-schemes given to the input of the simulation. To test the new algorithm, it has been decided to produce the testbench input VHDL file with a C++ program in the ROOT framework. Analyzing the stau sample with a mass of 1599 $GeV/c^2$, 100 events have been selected in order to give as "input stimulus" to the simulation special BX-schemes alternated with BX-schemes not to be modified. The output of the simulation was written on a text file and analyzed with a different ROOT macro. An example of a typical Vivado simulation input and output graphical picture is given in figure 5.2.

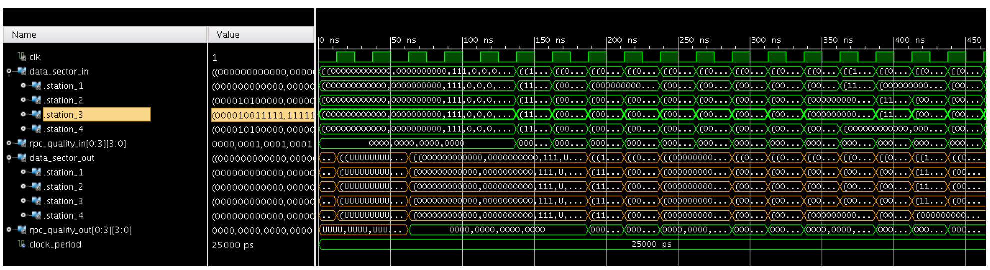


Figure 5.2: Typical Vivado simulation input and output graphical picture.

The correctness of the algorithm and of the code for the implementation has been proven and the results are shown in figure 5.3, where the alternate value of the distribution demonstrate that one out of two BX-schemes have been modified by the 2BX trigger, as it was given as input of the testbench.

If some characteristics are intentionally modified in the superprimitives of the special BX schemes in order not to respect the requirements, for example increasing the $\phi_B$ angle to be greater than 3° in the BX schemes with all 4 superprimitives, the algorithm behaves as expected, not changing the BX of the superprimitives with wrong properties. An example is give in the figure 5.4, where are also shown the details of some superprimitives that were not satisfying the 2BX trigger conditions.

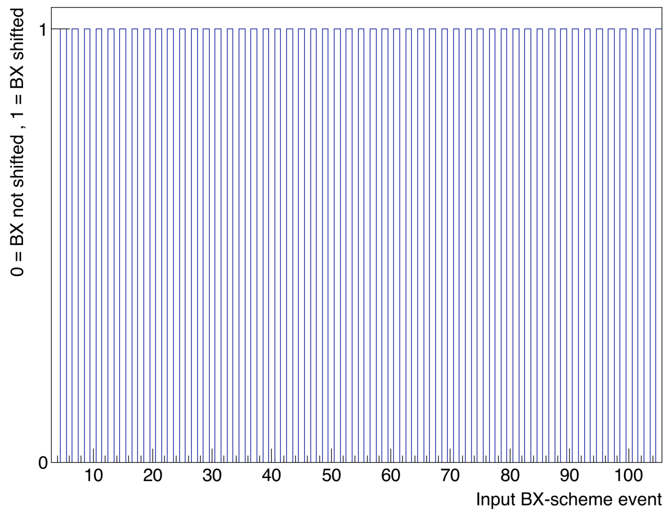


Figure 5.3: Results of the Vivado testbench for the new algorithm. The alternated values of the curve show that, as it was given to the input, one out of two superprimitive BX-schemes has been shifted to the BX of the innermost superprimitive by the 2BX trigger.

## 5.2 TwinMux hardware implementation and preliminary results

Finally, the new firmware including the 2BX trigger algorithm has been implemented into the spare TwinMux board. Due to the fact that it is used for tests mainly with cosmic rays, the 61-st TwinMux can be connected to the sector 9, 10 or 11 of the wheels $-1$ and $-2$. Those sectors are the ones with the highest rates because they are almost parallel to the ground and the cosmics have a $cos^2(\theta)$ angular distribution with respect to the vertical direction and the two wheels are under the access to CMS cavern so that muon rate is not reduced by the 100 meters of ground. Up to the end of August 2017, only DT signals have been split to be accessed also with the spare board, thus only the HH quality condition on the first valid DT primitive of the BX-schemes remains valid. Once also the RPC signals are available, the DT primitives will be corrected by the RPC ones and the requirement on the RPCbit $= 1$ will become effective.

Initially, data have been collected during the proton-proton interactions and in cosmic runs, while the LHC was stopped, monitoring the number of times the algorithm was activated when the spare TwinMux was connected to the sector 9 of wheel $-2$. In both

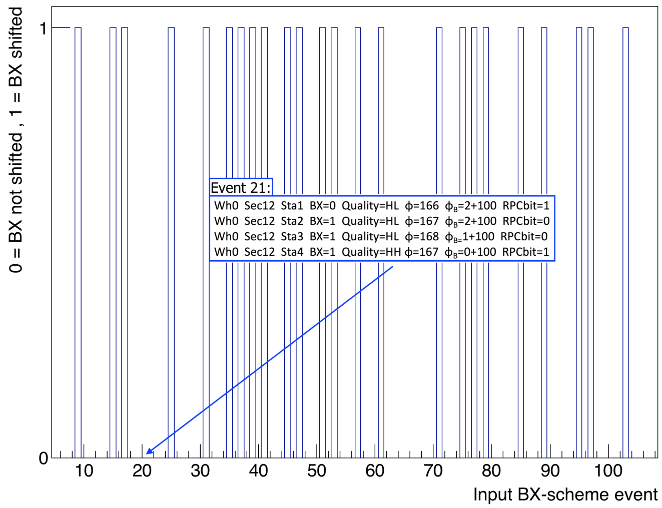


Figure 5.4: Results of the Vivado testbench for the new algorithm. The missing superprimitives BX modification is due to an intentional increase of the $\phi_B$ in order not so fulfill the requirements of the 2BX algorithm. An example of BX scheme with modified properties is given.

301142 and 301161 *pp* LHC runs, which lasted for almost 6 and 5 hours respectively, 9 events were registered. In figure 5.5, the distribution of the events as a function of the time is presented. For these runs, the data files of the reconstructed tracks for the muon system have been produced and analyzed, founding *zero* events corresponding to particles generated in the collision region. To explain the origin of the algorithm activations, the 7.5 hours long 301062 cosmic run has been analyzed. 5 special BX-schemes were found (figure 5.6), confirming that the cause are the cosmic muons crossing the detector during both proton-proton collisions and cosmic runs. Owing to the fact that offline analysis are affected by all the trigger and reconstruction selections, a number less or equal to the one registered during the online data taking is expected.
To check the difference in the rate of the algorithm activation when considering different sectors, the 61$t$-st TwinMux has been connected to the wheel $-1$ and $-2$ using the sector 10. The rate for both the lowest sectors was $1-2$ events per hour during pp and cosmic runs, as registered for the initial considered sector.

The most important result obtained for the hardware implementation is the confirmation

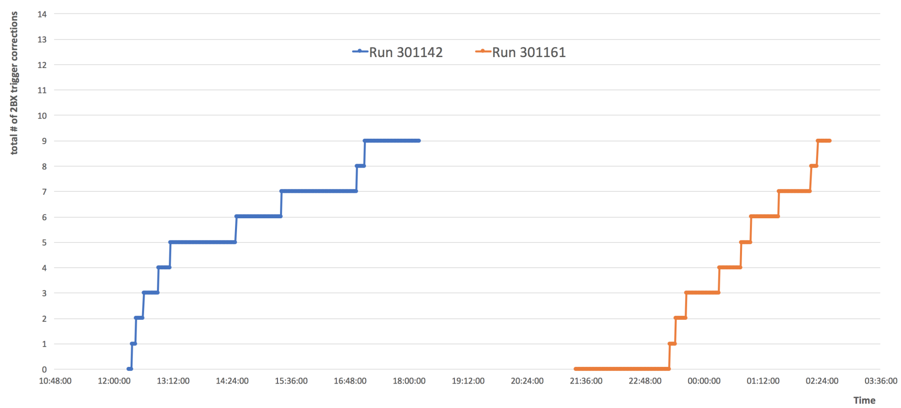


Figure 5.5: TwinMux spare board connected to the sector 9 of wheel −2. Total number of 2BX algorithm activation as a function of the time during the LHC pp collisions in runs 301142 and 301161. For both the runs, lasted for 6 and 5 hours respectively, 9 events were registered.

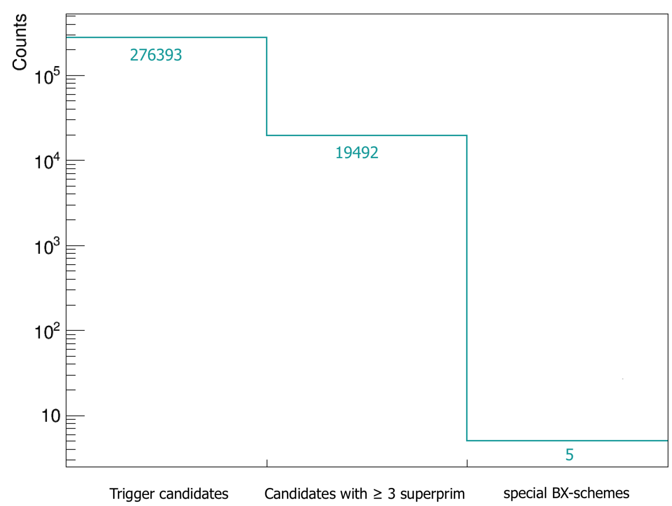


Figure 5.6: Number of trigger candidates corresponding to the properties required by the 2BX trigger algorithm for the cosmic muons detected in the 7.5 hours long 301062 cosmic run. The first bin represents the total number of candidates, the second one contains the number of candidates with at least 3 valid superprimitives and the last bin is the number of special BX-schemes that would activate the algorithm.

that the 2BX trigger algorithm is working properly when implemented on the spare TwinMux board connected to the four DT stations of the CMS detector.

# Chapter 6

# Conclusions on the 2BX L1 trigger and future perspectives

Inspired by the 2012 trigger for slow-moving particles, the idea of considering two consecutive BXs was applied to recover particle tracks which are rejected by the present L1 muon trigger chain. The 2BX algorithm, which consists in shifting the superprimitives to the first of the two BXs in the presence of special BX patterns of the candidates, has been tested and implemented. Given the present time resolution available for the superprimitives of 25 $ns$, it was the only possible modification applicable to the current trigger chain, which could lead to modest improvements in the trigger efficiency ($\sim 5\%$).
A drastic change of the performance can be introduced in the upgrade of LHC and CMS planned to begin in 2024. One of the most significative modifications foreseen for the Drift Tube chambers is the complete substitution of the present L1 trigger. The only component left in the on-board electronics (minicrates) will be the Time to Digital Converters (TDC), which will send the hit time information to a dedicated trigger chain based on FPGAs located outside the experiment cavern. The advantages of this upgrade will be the presence of simpler and more radiation hard electronics on the chambers, the reduction of the power consumption, and the possibility to perform parallel computation for the trigger primitives.
For what concerna the improvements on triggering the slow-moving particles considered in the thesis work, for the Phase 2 of LHC there will be the possibility to have a better resolution on the time assignment to the trigger primitives. A time resolution of BX/4 instead of the present 1 BX is under study; thus, from 25 $ns$ to 6.25 $ns$. The dramatic reduction on the time precision, will lead to a possible calculation of the $\beta$ of the particles at the L1

trigger level. The discrimination between slow-moving and ultra-relativistic particles could be done in the initial selection, maximizing the statistics for the interesting processes. To prove and show the feasibility of the computation of $\beta$ at a trigger level after the LS3 upgrade, the reconstructed tracks of the stau M = 1599 $GeV/c^2$ sample with at least 3 DT segments and their offline time information are considered. In figures 6.1, 6.2 and 6.3 are presented respectively the distributions of the difference between $1/\beta$ calculated with the offline resolution on $t_0$ ($\sim$ 2 $ns$) and $1/\beta$ truncating the $t_0$ information to a precision of 1BX (25 $ns$), BX/2 (12.5 $ns$) and BX/4 (6.25 $ns$).

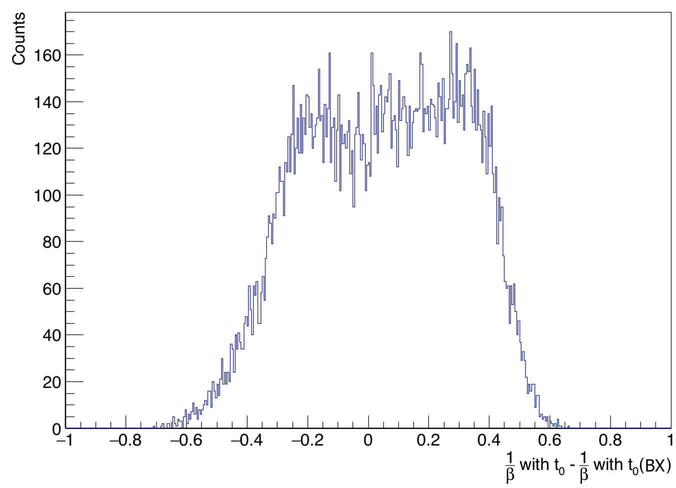


Figure 6.1: Distribution of the difference between $1/\beta$ calculated with the offline resolution on $t_0$ ($\sim$ 2 $ns$) and $1/\beta$ truncating the $t_0$ information to a precision of 1BX (25 $ns$) for the same track with at least 3 DT segments.

Comparing the standard deviations of the distributions with the resolution of $1/\beta$ obtained for the muons (0.0646), it results that even with a BX/2 truncation on $t_0$ the calculation is precise enough to give information about the velocity of the particle; although, reaching a BX/4 resolution on time assignment to the trigger primitives, the $1/\beta$ can be computed with a deviation with respect to the offline one less than the intrinsic resolution.

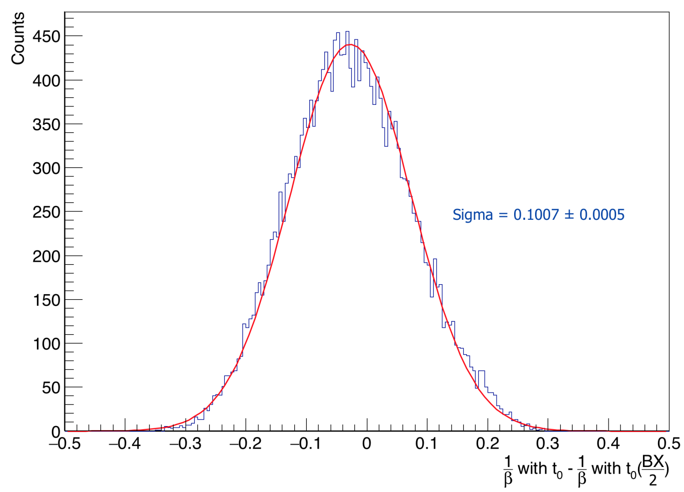


Figure 6.2: Distribution of the difference between $1/\beta$ calculated with the offline resolution on $t_0$ ($\sim 2\ ns$) and $1/\beta$ truncating the $t_0$ information to a precision of BX/2 (12.5 $ns$) for the same track with at least 3 DT segments.

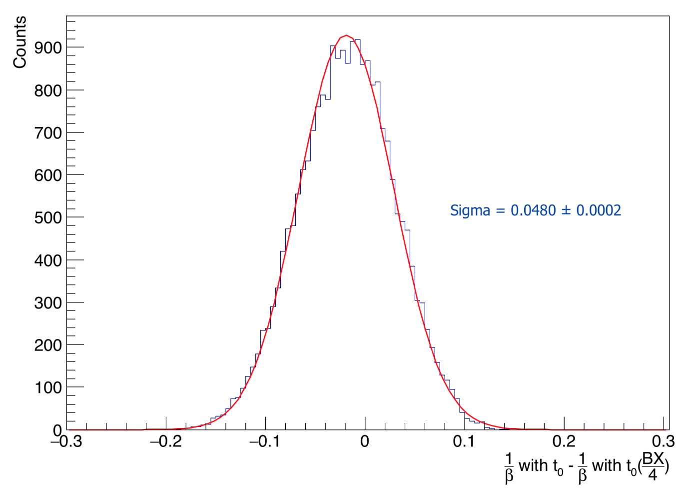


Figure 6.3: Distribution of the difference between $1/\beta$ calculated with the offline resolution on $t_0$ ($\sim 2\ ns$) and $1/\beta$ truncating the $t_0$ information to a precision of BX/4 (6.25 $ns$) for the same track with at least 3 DT segments.

# Chapter 7

# Aging studies for the DT chambers

After all the successes achieved by the LHC and its experiments in the past years, for instance in discovering the Higgs boson, a large variety of other searches has been performed to investigate the existence of Beyond Standard Model particles. No new physics has been found yet, however limits have been set on the masses and the cross sections.

To increase the sensitivity for the new physics searches, an upgrade for the LHC accelerator, the High Luminosity project, is planned during the Long Shutdown 3 (LS3) in the period $2024-2026$. The instantaneous luminosity, $\sim 2\times10^{34}\ cm^{-2}s^{-1}$ in 2017, will be increased to reach the value of $\sim 5\times10^{34}\ cm^{-2}s^{-1}$, providing to the experiment an integrated luminosity of 3000 $fb^{-1}$ at the end of LHC Phase 2 $(2026-2038)$. Combined with an energy increase to 14 $TeV$, it will make possible to extend the mass reach of at least one TeV for many proposed scenarios, including Supersymmetry, to measure with high precision the properties of the Higgs boson, allowing searches for new physics associated with the Higgs sector, and to improve the accuracy for SM tests.

With ten times the integrated luminosity for which the detectors were designed, the issues related to the total absorbed dose - the aging phenomena - must be studied to prevent and control a possible lowering of the performance. Indeed, for all the measurements that have been described in the previous chapters, such as the calculation of the velocity and the momentum, the trigger efficiency and others that were not mentioned in this thesis, it is essential to keep unaltered or, at least, as good as possible the efficiency and the characteristics of all the subdetectors.

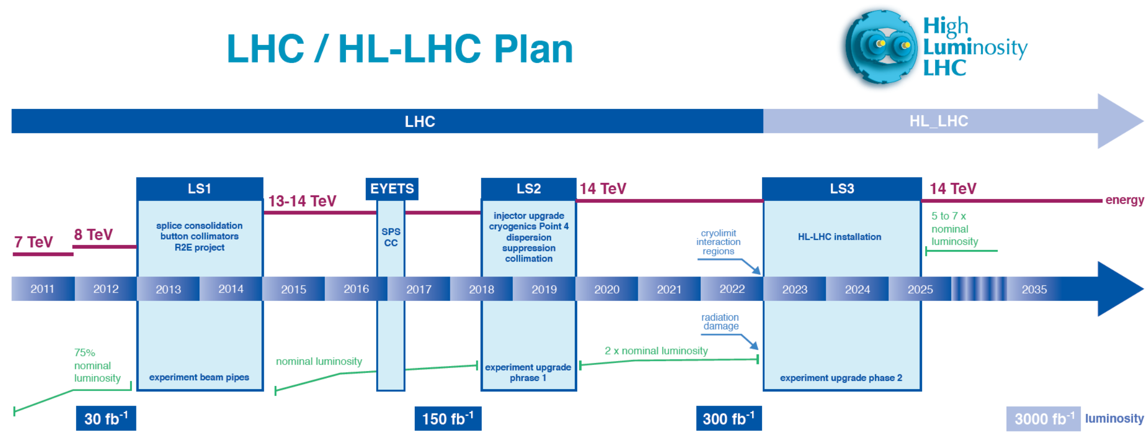


Figure 7.1: LHC and High Luminosity LHC project plan.

## 7.1 Aging: definition and issues in Drift Tube Chambers

The deterioration of performance under irradiation has been observed since the creation of gaseous wire detectors. It is caused mainly by the formation of polymeric material in the avalanche electron multiplication. Chemical and physical processes, also known as plasma chemistry, cause a degradation of the surface quality of the electrode materials due to a coating layer usually composed by silicon and carbon compounds. These effects have been largely studied in the past years for various gain, materials and gas compositions in different detectors. No solutions valid for all cases have been found, although some components have been classified as pollutants, for instance specific epoxy glues, silicon oils, organic quenchers and plastic o-rings. [25], [26]

Due to the fact that every system behaves in different ways under irradiation, it is necessary to investigate the consequences of aging on the performance of each detector as a function of the absorbed dose.

The DT chambers utilize a safe $Ar/CO_2$ mixture, which is recirculated with a fresh gas intake of 15%, taking about one day to replace the whole gas volume. The degradation of the system behavior can be caused by gas leakages, variations in the gas mixture, presence of humidity in the gas or contamination with oxygen or pollutants from outgassing materials. In proximity of the anode wires, the high voltage leads to the generation of a plasma which can polymerize the substances present in the gas and make them deposit on the surface of the wires, causing an increase of their thickness. Owing to the fact that the electric field, which is also responsible of the electron signal amplification, is inversely proportional to the radius of the wire, a reduction of the effective field results in a smaller amplitude of anodic signals. If the amplitude becomes smaller than the threshold used to filter the background signals, some hits can be lost.

Because of that, the possible tests that can be employed to monitor the presence of aging are:

- the online measurements of the current drawn by the wires
- the study of the detection efficiency as function of the voltages applied to the electrodes
- the direct or indirect investigation of the amplification on the wires
- the inspection of the wires, determining the actual conditions of their surface.

## 7.2 Present performance of the muon DT chambers

Up to 2017, the total integrated luminosity delivered by LHC to the CMS experiment has been $\sim 100\ fb^{-1}$ (figure 7.2).

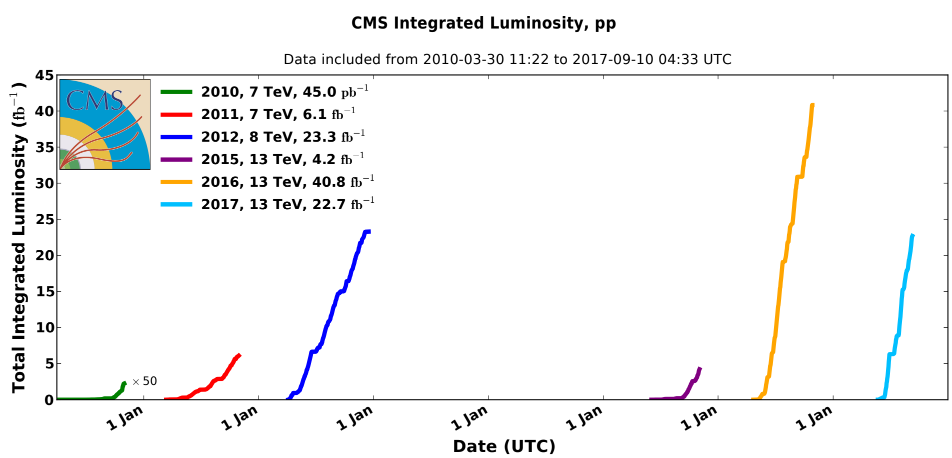


Figure 7.2: Integrated luminosity delivered by LHC to the CMS detector from 2010 to 2017.

To test the presebt conditions of the chambers installed in the CMS detector, a study of the efficiency as a function of the wire high voltage (HV) has been conducted, varying this parameter for one layer of the innermost $\phi$ superlayer and performing the reconstruction of the track segments without considering the specific layer with modified HV, obtaining unbiased measurements. These results have been compared to the ones obtained with a spare MB2 chambers which has never been used, so it is completely free from aging effects, and with the MB3 chambers installed with a telescope configuration at the Legnaro National Laboratories of the Istituto Nazionale di Fisica Nucleare (INFN LNL, Italy). The efficiency has been computed using the formula 7.1, considering the number of extrapolated tracks with hits in the cells of the layer with modified HV and the number of extrapolated tracks that have passed those the cells. The segments in the chamber have been reconstructed using only the hits of the $\phi$ layers with a standard HV. For the P5 chambers, the measurements have been performed with cosmic rays during the winter period when LHC was not available. The muon cosmic trigger required a muon in the lower sectors of CMS. The selected reference track had to have a reconstructed segment in the chamber under test with at lest 5 associated hits in the layers with the standard HV. For the MB2 spare chamber cosmic muon tracks were identified with the coincidence of a correlated trigger in 2 of the 3 superlayers of the chamber. For the MB3 at LNL the trigger was defined by a correlated trigger in the upper chamber of the telescope.
In figures 7.3 and 7.4, the efficiency curves are presented. It has to be taken into account that the atmospheric pressure is significantly different between Legnaro and the CMS cavern, because they are at different heights on the sea level, affecting the behavior of the system. However, even if the experimental conditions were dissimilar, some indications can be extracted for the performance of the chambers from the shape of the curves, which are identical but shifted along the x-axis.

$$efficiency\, of\, the\, cell = \frac{extrapolated\, tracks\, with\, hits\, in\, the\, cell}{extrapolated\, tracks\, in\, the\, cell} \tag{7.1}$$

The performance of the DT chambers is very similar in the efficiency plateau starting from 3600 $V$, while the curves can be distinguished in the turn-on region, near 3400 $V$. A higher degradation for the outer chambers of the wheel 0 and for the outer wheels is observed.

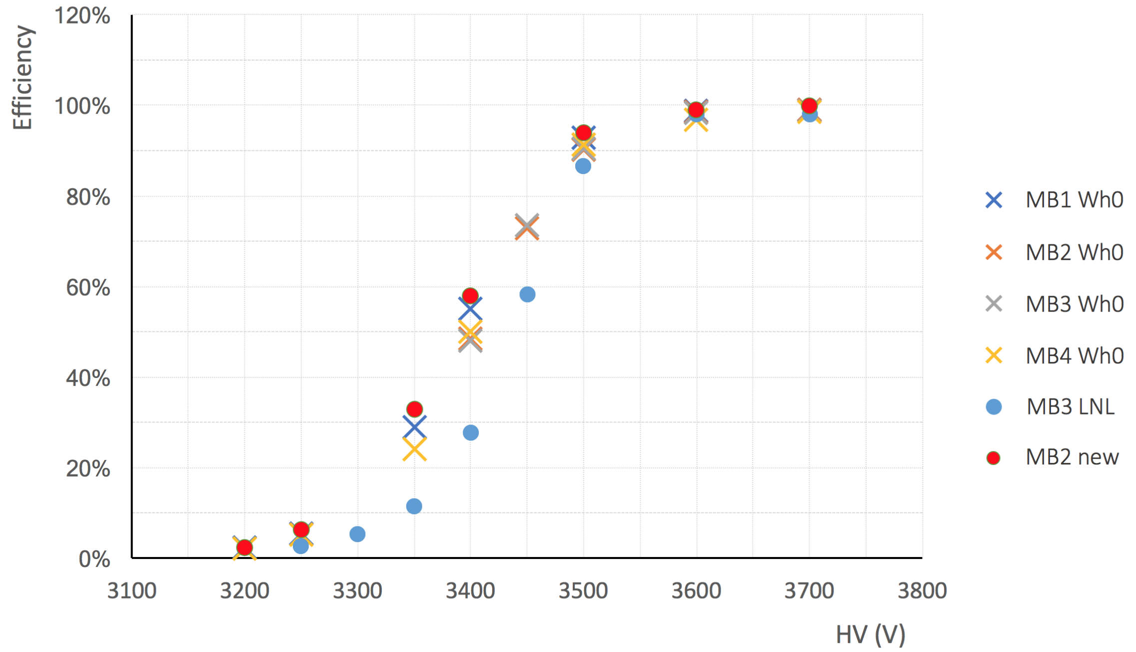


Figure 7.3: Efficiency vs wire HV curves for the DT chambers installed at P5 and LNL, and a spare MB2. The threshold for the signal is set to 30 $mV$.

## 7.3 Preliminary tests with a DT spare chamber

In fall 2015, some aging tests were performed on a spare MB1 chamber in the recent constructed GIF++ facility at CERN [27], where a radioactive $^{137}Cs$ source with an activity of 13.9 $TBq$ is installed.
Due to the care in selecting the materials at the time of the production and the encouraging absence of relevant aging effects after an equivalent integrated luminosity of 40 $fb^{-1}$ received by the DT chambers installed in CMS, optimistic predictions were made for the DTs behavior in presence of a higher dose.
At the beginning of the operations, the radiation emitted by the $^{137}Cs$ source and absorbed by the MB1 was not monitored, as well as the current drawn by the wires. Indeed, it was expected that in presence of a constant radiation flux and without aging effects, the current value had to be constant. When the instrumentation for the current measurements became available, a dramatic decreasing of the performance has been registered (exponential low-

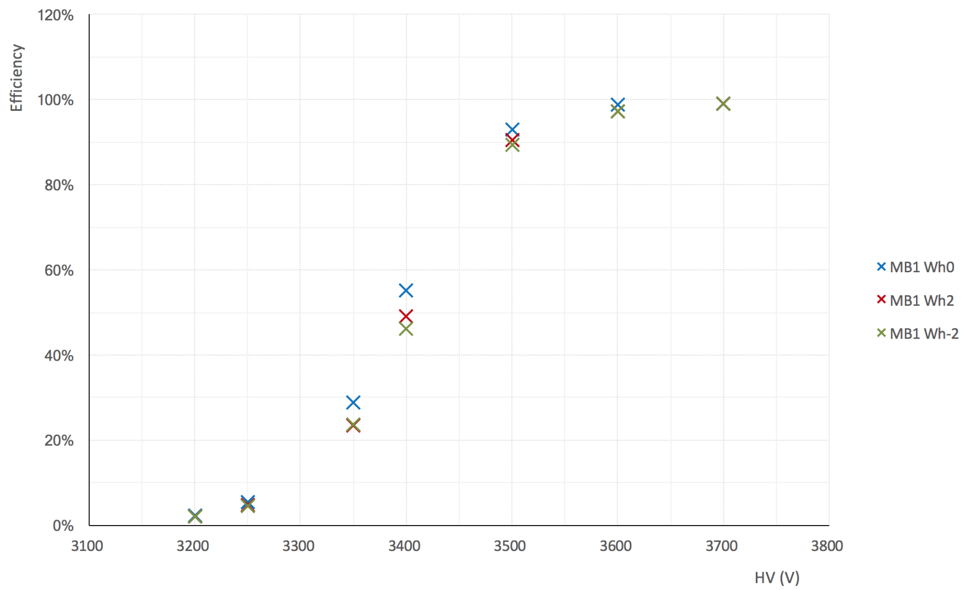


Figure 7.4: Efficiency vs wire HV curves for the MB1 chambers installed in the wheels −2, 0, +2 of the CMS barrel. The threshold for the signal is set to 30 $mV$.

ering of the current) and some investigations had to be performed searching for the causes. The effects on the wires of an equivalent dose of $\sim 10$ times the one foreseen for the HL-LHC project absorbed in one month of accelerated test are shown in the pictures in figure 7.5. The wire has been removed from the MB1 chamber and inspected with a Scanning Electron Microscope (SEM) in Legnaro, measuring an increasing of the diameter from 50 $\mu m$ to 70 $\mu m$.

Using the SEM, the layer coating the wire have been studied founding compounds of oxygen, carbon and silicon. The spectrum of the deposits is shown in figure 7.6, where the gold plating of the steel wire appears completely hidden by the pollutants.

## 7.4 Bicells: two paired DT cells

In order to be able to perform specific tests on the DT cells (such as for identifying the origin of such deposition or for measuring the rate of the aging as function of the integrated luminosity [26],[28]), it was decided to build small prototypes of DT chamber cells, the bicells. Designed as shown in figure 7.7, they are divided into three different zones: the

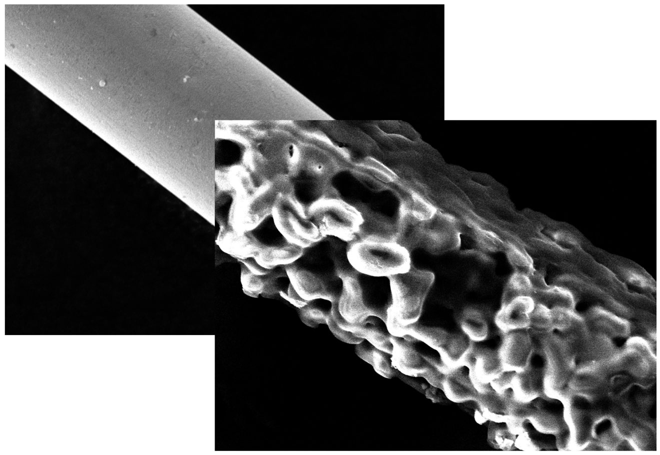

Figure 7.5: Comparison between a clean wire ad the aged wire of the MB1 chamber after the accelerated irradiation tests.

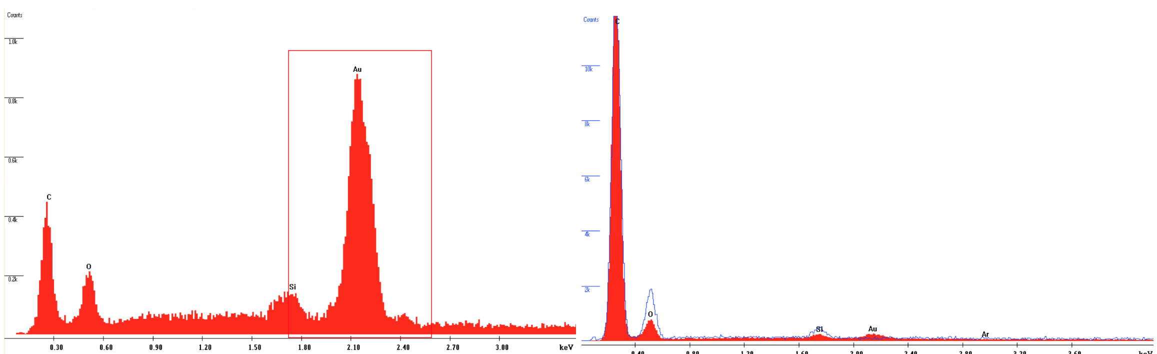


(a) Clean wire

(b) Aged MB1 wire

Figure 7.6: Spectra obtained with the SEM inspection of a clean wire and an aged wire of the MB1 after the accelerated irradiation tests. In blue and red are plotted two different regions of the wire.

main central one with the gas active volume, and two smaller ones at its sides, in which all the electronics for high voltage (HV) and signal processing are placed. Such a configuration allows to have the HV and the FE electronics not in contact with the gas fluxing inside the cells.

Aluminium slabs ($1,2m \times 12cm \times 2,5mm$) are used to delimit the entire volume on bottom and top. The top slab is divided into three parts (HV region, FE electronics region and sensitive wire region) which are fixed to the rest of the structure using screws in order to be independently removable. The removable covers allow to inspect the interior of the cells and to change the wires when needed.

The central zone is separated from the two ancillary parts by two aluminum blocks with several holes for gas pipes and for HV cables. These two blocks and the walls of the bicells are glued to the basis as well.

In the active parts the aluminum I-beams (85$cm$ long) are glued to the bottom slab, the gold coated steel anode wires (50$\mu m$ in diameter) are positioned in the center, and the aluminum strips sticked to the upper and the lower slabs in the middle of each cell. The I-beams are partially covered with Mylar tape for isolating the aluminum strips which serve as cathodes .

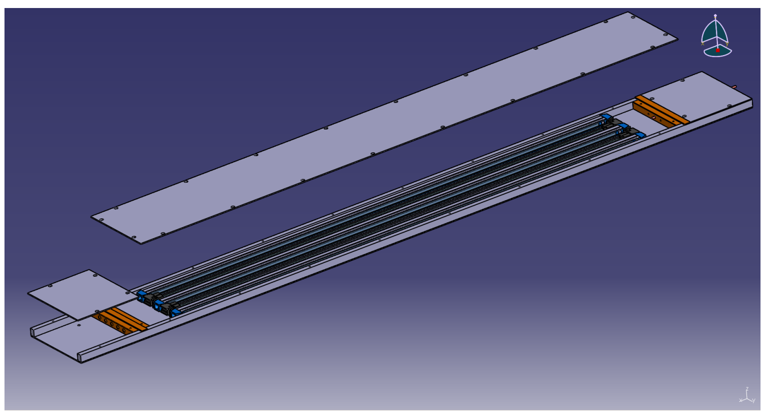

Figure 7.7: Design of the bicell

The electronic chain for each wire is shown in figure 7.8. The power supply is connected to a low-pass RC circuit to clean accidental voltage noise and to the anode wire. Between the wire and the electronics of the front end a high-pass RC circuit with a spark gap is placed. The electronics for the read out is composed by a MAD integrated circuit, with a charge pre-amplificator, a signal shaper, a comparator with a threshold, usually set to a voltage of 20mV, and an output stage [29].

The two bicells have been assembled in the INFN LNL with spare materials coming from several labs where DT chambers were built. This detail is of the highest importance because the goal is to reproduce exactly the cells of the DT chambers, with the same materials and

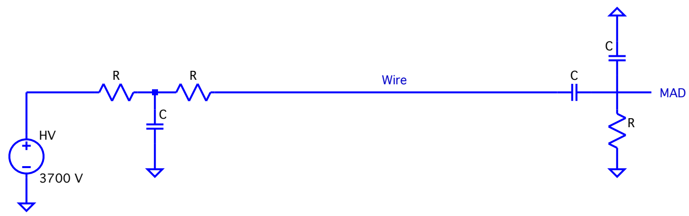


Figure 7.8: Wire electronical scheme

performance, in order to test their aging problems as if they were original cells.
While the DT chambers were constructed within a system of high accuracy alignment system (100 $\mu m$ in positioning the wires), the bicells were entirely hand-made build.
First, the walls and the I-beams (with cathodes pre-attached) were glued to the basis slab using Araldite at a distance of $4,2$ $cm$; than electronic cables and copper gas pipes were glued, using DP190, to the blocks which close, in the wire direction, the active region. Swagelok connectors have been used for the gas pipes lines. After the glue became dry, it was possible to stick with Araldite the blocks to the bottom aluminum slab at an approximate distance of 1 $m$ and to place the anode wires and their plastic supports at the ends of the I-beams.
In the last operation the wires were connected to the electronics and the electronic boards were fixed to the aluminum slab using screws and hex nuts.
Once every component of the cells was in place, the bicells were closed with the three covers using screws and aluminum tape to seal them.

### 7.4.1 Tests of the bicells

Once all the hardware was checked to work properly, it was possible to perform the tests. The behavior of a DT cell can be characterized with:

- the distribution of the first hit time (Timebox), whose shape gives information about the uniformity of the efficiency within the cell and of the electric field shape.
- the linearity of the distribution Time vs Track position, which gives information about the drift velocity of electrons in gas.

- the resolution of the reconstructed position.
- the detection efficiency as a function of the position of the track in the cell.
- the detection efficiency as a function of the wire voltage (the amplification gain).
- Electrons multiplication around the wire, which gives the signal gain between the ionization electrons created by the cosmic muon in gas and the signal on the wire.

Only the efficiency and the amplification studies of the bicells are discussed in the following sections, because of their relation with the aging effects. All the preliminary tests performed to check whether the bicells were working properly after the construction are reported in the appendix A.

### 7.4.2 Efficiency of the bicells

#### Experimental setup

As shown in figure 7.9, both the bicells were positioned upon the ch2 in the MB3 telescope installed in Legnaro.The wires of ch1 and ch2 are aligned with high accuracy and the two chambers are placed in two parallel planes [30]. In the following we will call $\phi$ and $\theta$ the position measured by the r-phi and r-z SLs of ch2; the z direction is normal to the plane of the ch2 plane (DT chamber local frame, figure 2.8). The two bicells have been placed with quite a high precision in a plane parallel to the ch2 plane with the wires of the bicells parallel to the $r-\phi$ wires of ch2 and in the same $r-\theta$ position of ch2, in order to simplify data analysis. HV was set to +3700 V for the wires, +1800 V for the strips, $-1200$ V for the cathodes, which are the same values of the ch1 and ch2 electrodes (standard values at LNL, see [30]); the threshold was set to 20 mV. As in the preliminary tests, the four wire output channels were plugged into four read-out channels (#0,#9,#6,#15).
The following results are based on a data collection run with a total 2 million events (around 2 hours) triggered by ch1. The number of events with just one track well reconstructed either in ch1 or in ch2 are 100K. Considering just the geometrical acceptance, the expected good events per cell should be $\sim 1800$.

#### Data analysis and results

Detection efficiency is defined as the number of events detected by the bicells related to the number of events triggered by the chambers and passing through the bicells (equation 7.2).

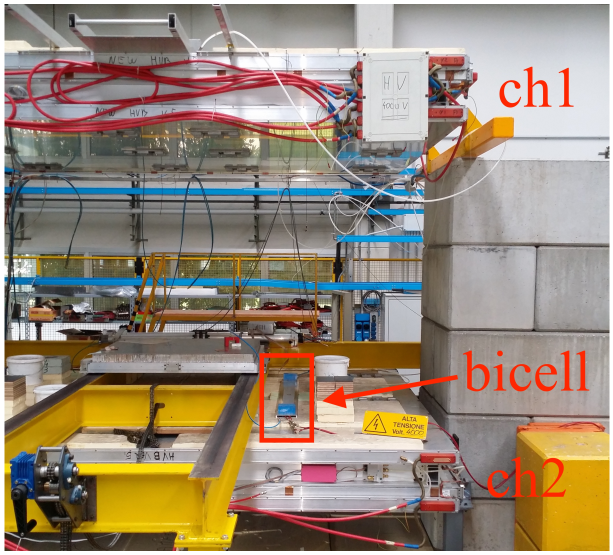


Figure 7.9: MB3 telescope available at LNL. The bicells have been positioned upon the lower chamber to test their performance.

$$Efficiency = \frac{counts_{bicells}}{counts_{chamber}} \tag{7.2}$$

It is possible to analyze the efficiency of the bicells as a function of the $\phi$-position (figures 7.10,7.11,7.12,7.13) at different voltage. The shape of the efficiency, with respect to the distance of the track from the wire, reflects the electric field shape of the cell (figure 2.8). Indeed, the primary electrons are uniformly distributed along the track path but only the ones which drift towards the wire will contribute to the avalanche. Where the track crosses the cell at a distance from the wire with a short path with lines ending on the wire, there will be a less probability to have enough primary electron to produce a detectable signal at a given HV, i.e. at a given amplification.
The average efficiency as a function of the voltage of the bicells wires is shown in figure 7.14. These plots show a wide efficiency plateau with a constant value of 98% from 3550 to 3900 Volt. The curves for the four cells are almost identical.

### 7.4.3 Amplification near the wire

One of the visible effect of aging on gas detectors is a lowering of the signal amplification as function of the integrated current. The bicells will be used to studies such effects, thus

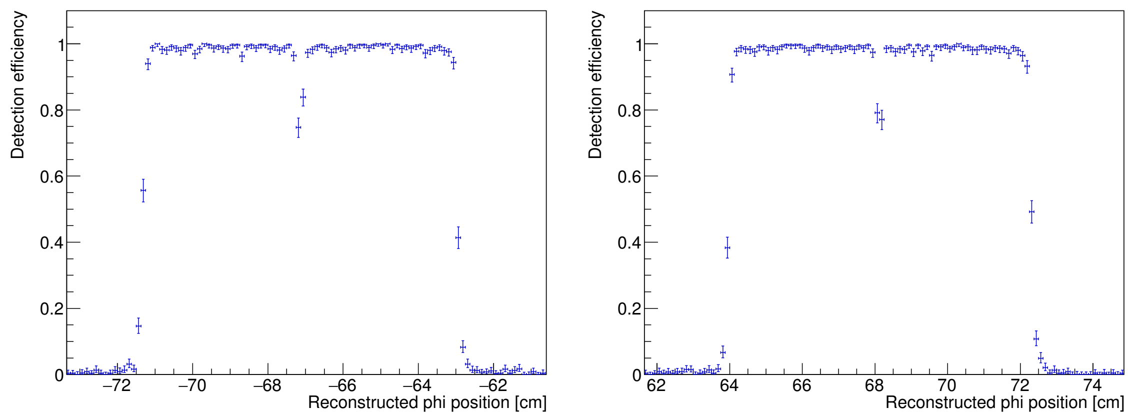


(a) Cells #6,#15 (b) Cells #0,#9

Figure 7.10: Efficiency of the bicells as a function of the $\phi-$position of the tracks (wire voltage 3700 V).

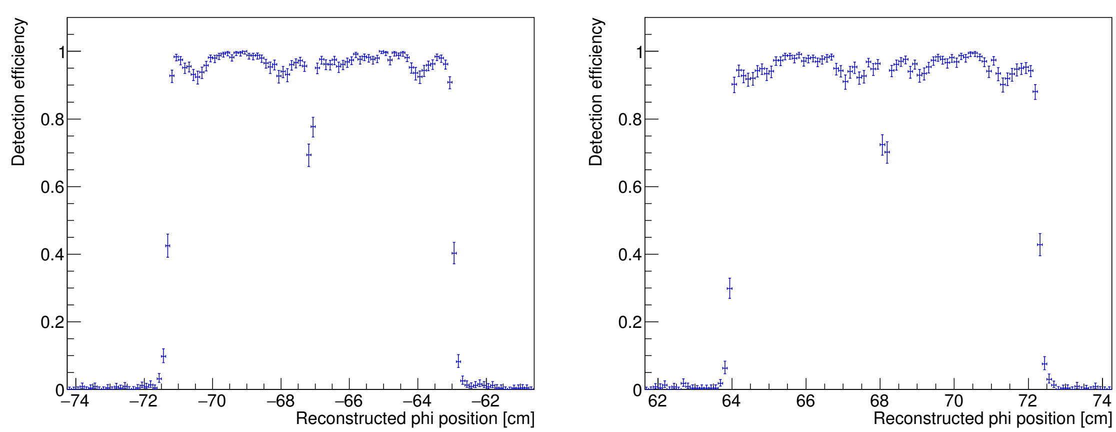


(a) Cells #6,#15 (b) Cells #0,#9

Figure 7.11: Efficiency of the bicells as a function of the $\phi-$position of the tracks (wire voltage 3550 V).

it is important to evaluate the amplification on the wire to a given release of energy in the cell as in the case of minimum ionizing particle or of gammas from radioactive sources. In these checks of the bicells, the total charge signal produced by a gamma source was measured for evaluating the amplification on the anode wires. These measurements with

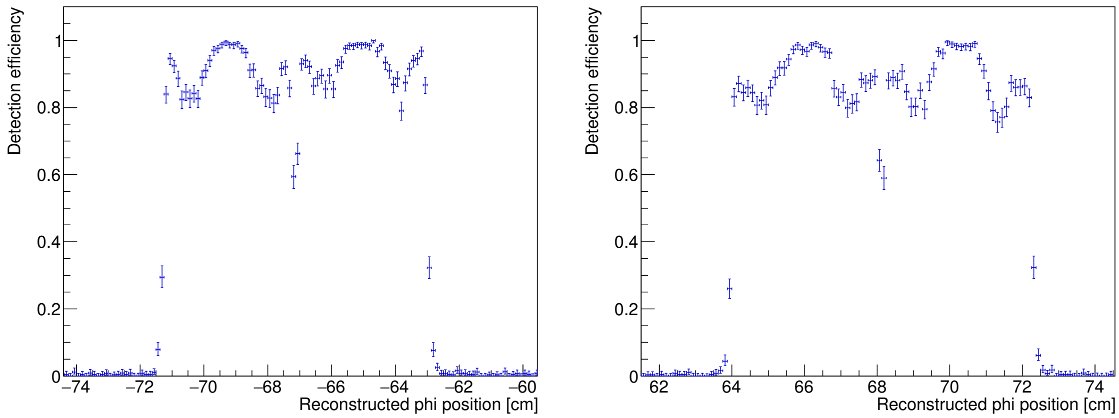


(a) Cells #6,#15 (b) Cells #0,#9

Figure 7.12: Efficiency of the bicells as a function of the $\phi-$position of the tracks (wire voltage 3500 V).

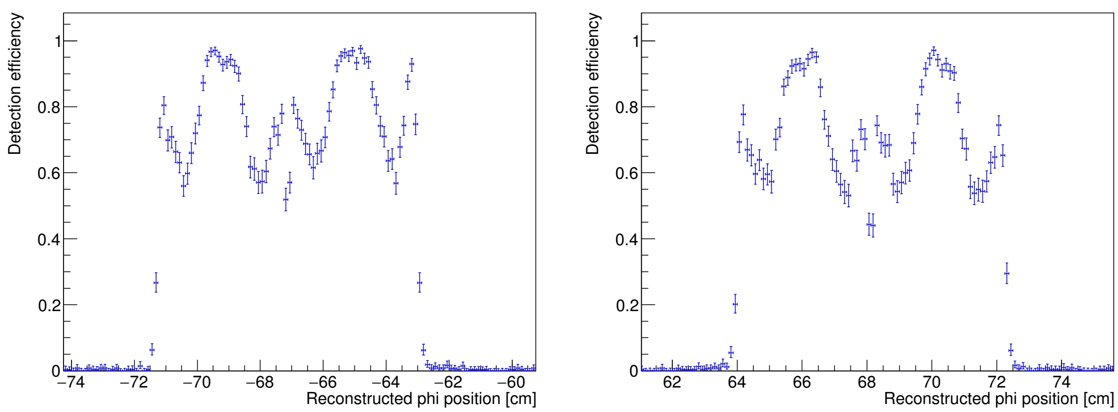


(a) Cells #6,#15 (b) Cells #0,#9

Figure 7.13: Efficiency of the bicells as a function of the $\phi-$position of the tracks (wire voltage 3450 V).

sources will be easily redone at any time later during aging tests. The important aspect will be the accuracy not on the absolute amplification but the accuracy on the variation of the amplification (before, during and after the aging tests).

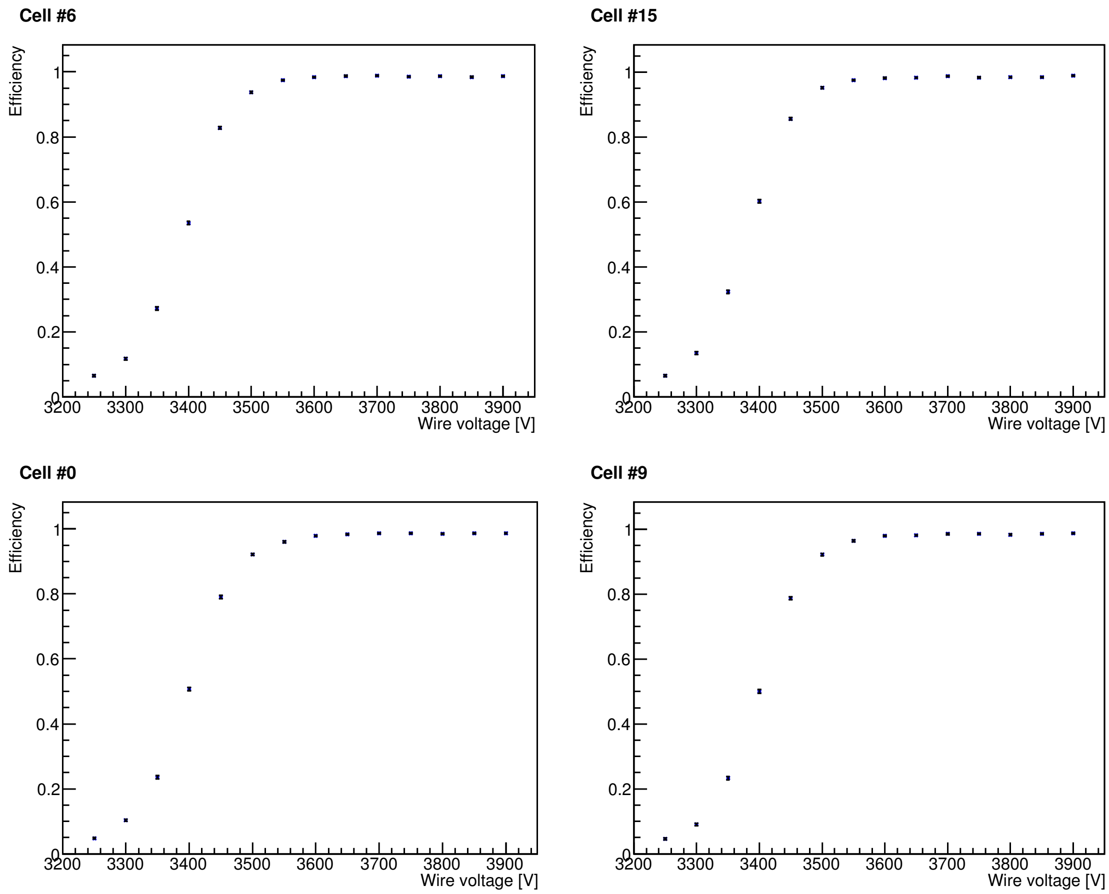


Figure 7.14: Average efficiency of the four cells as a function of wires HV.

### Experimental setup

A hole (1 $mm$ in diameter) was made in the upper central cover of the bicells and a collimated radioactive source of $^{109}$Cd with an activity of 419 kBq placed above. $^{109}$Cd has gamma decays and emits photons with energies of 22 keV (85%) and 24.9 keV (14%) [31]. The gas tightness was maintained covering the hole with Mylar tape.

Two different charge preamplifiers with feedback capacitors of 1pF and 7pF were used in order to cover the signals ranges at the different HV setting. The amplified signals were digitized using a 1024-channels Multichannel Analyzer (MCA).

### Data analysis and results

The weighted average of the energies of the photons emitted by the $^{109}$Cd is 22.41 keV. Through photoelectric effect (figure 7.15), photons give almost all their energy to an electron, which, in Ar/$CO_2$ gas (85/15%) has a range of 5.7 $mm$ and produces $\sim$ 830 ion-electron pairs (27.05 $eV$ each). However, the zone of the electric field, inside the cell, from which the electrons produced can drift to the wire, in the specific point of the hole done on the bicell's cover, is $\sim$ 4 $mm$ wide, thus $\sim$ 580 of the primary and secondary created photoelectrons drift toward the wire producing the amplification and then the detected signal [32].

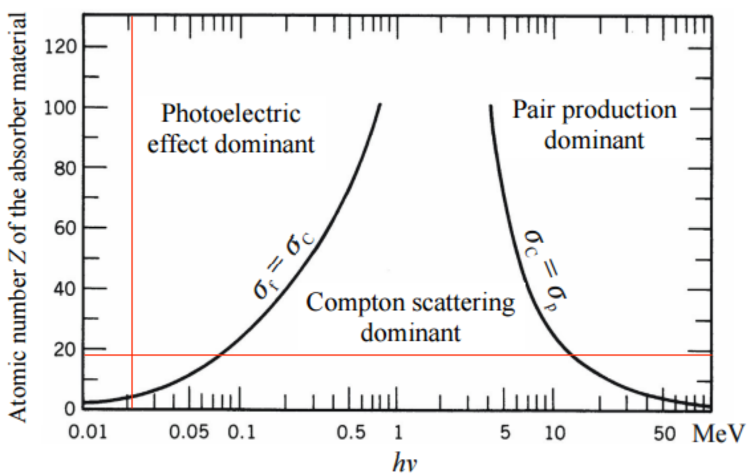


Figure 7.15: Photons interaction with matter.

The signal of the electrons, amplified near the wire, is formed and amplified with 1pF and 7pF pre-amps. After the calibration of the MCA spectra done with known input test voltage signals applied to a 2.2pF test capacitor of the pre-amps (figure 7.16), the charge spectra are obtained (example in figure 7.17). The photo-peak distributions, relative to spectra taken varying the wire voltage, are fitted with a Landau curve, and its most probable value represents the charge collected by the wire. In figure 7.18 is shown the exponential rising of the amplification, defined as the charge detected by the wire related to the charge of the 580 electrons, as a function of the wires' voltage. Fitting the plot with an exponential curve it is possible to extract the amplification at 3700 V[1], which corresponds to a value of

[1] It was not possible to have experimental data at HV value of 3700V because of the electronics

$1.0 \times 10^5$.

The above amplification factor has been computed assuming the zone of the electric field with lines converging to the wire to be constant; in fact, in the DT cell this zone changes as a function of the HV, being thinner at low HV. Assuming the thickness of this zone to be proportional to the efficiency in the whole region (at least above 3450 V, below of which threshold effects would appear), the amplification at 3700 V would be $0.9 \times 10^5$.

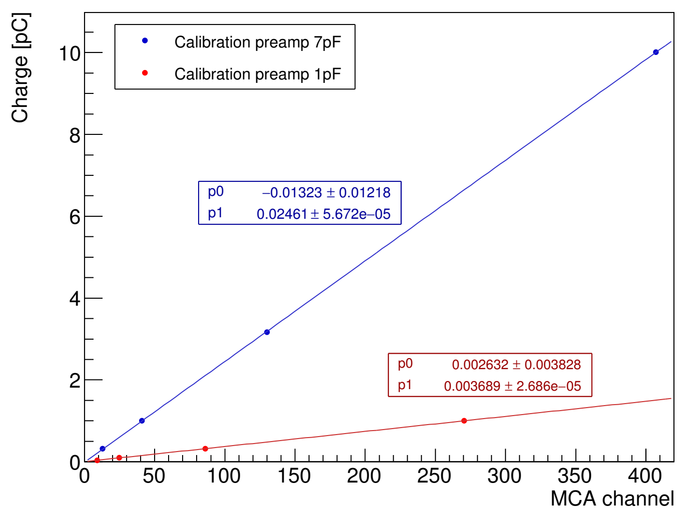


Figure 7.16: MCA calibration with 1pF and 7pF pre-amps.

### 7.4.4 Irradiation of the bicells and online analysis

The irradiation of one of the two bicells (Bicell 2) was performed at GIF++ delivering an equivalent dose to the one foreseen for the entire HL-LHC project in multiple steps. The online measurement of the current drawn by the wires is shown in figure 7.19. During the A period there was continuous irradiation of the bicell leading to an exponential reduction of the current (even though it was not always recorded). The other bicell (Bicell 1) was left outside the bunker of the GIF++, receiving no irradiation, and the measurement of its current was used to correct for systematics.

The exponential law followed by the current derives from the differential equation 7.3,

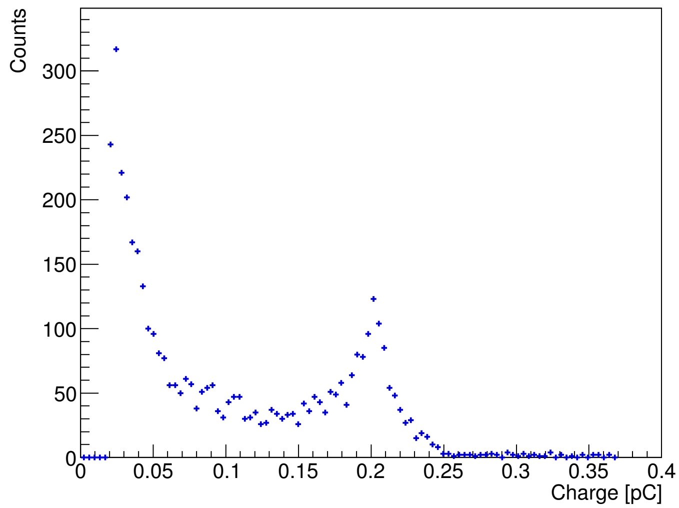


Figure 7.17: $^{109}$Cd charge spectrum, wire voltage set at 3250V.

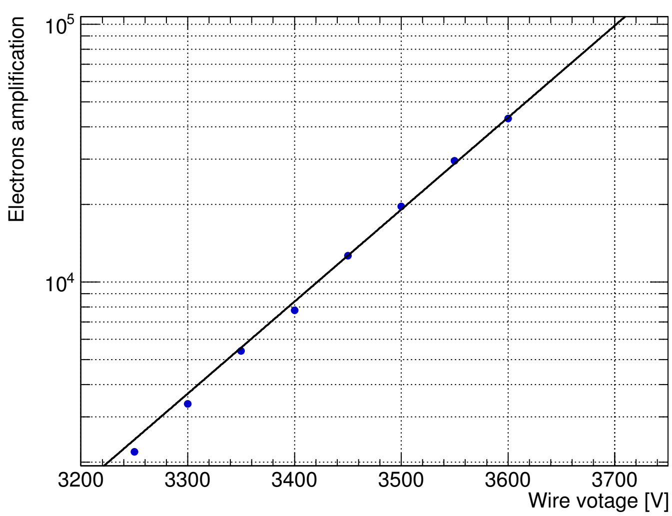


Figure 7.18: Amplification near the wire as a function of wire voltage.

$$\frac{dG}{G} \approx \frac{dI}{I} = -k \cdot Q_{coll} \tag{7.3}$$

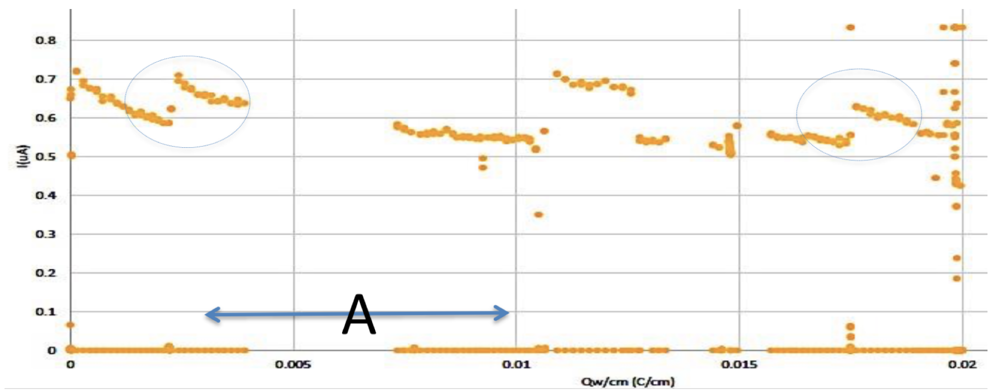


Figure 7.19: Online current test during the bicell irradiation at GIF++. Current draw by the wires as a function of the total collected charge. The period A is relative to a single continuous irradiation.

where the relation among the gain on the wire ($G$), the current ($I$) and the collected charge per centimeter ($Q_{coll}$) is shown. The constant k is measured in $(mC/cm)^{-1}$ and can be thought as the "half-life" of the gain. Higher is the constant, faster is the degradation of the system performance. In the period A, for the bicell it resulted $k = 3.95\,(mC/cm)^{-1}$, while for the MB1 chamber irradiated during the fall 2015 the constant was $k = 90\,(mC/cm)^{-1}$. This dissimilarity, which is also present in the aged wires inspection with SEM (figures 7.20, 7.5), depends on several factors, such as the different gas volume and gas flux, and the presence in the chamber of multiple elements, such as the electronics of the FE and the HV, which are installed outside the active region in the bicells.
For monitoring the different behavior varying the gas flux, 4 new bicells have been built with a slightly modified design in spring 2017 and the test at the GIF++ is still going on.

### 7.4.5 Tests and performance of the irradiated bicells

#### Detection efficiency before and after irradiation

Following the same procedure described in the previous sections to calculate detection efficiency, a comparison between the performance before and after the irradiation at the GIF++ facility is performed. In figures 7.21, 7.22 are presented the results for the average detection efficiency of the 4 cells of the 2 bicells; "Bicell 1" is the one which was kept outside the bunker of the GIF++ during the irradiation of the "Bicell 2". Standard voltages were

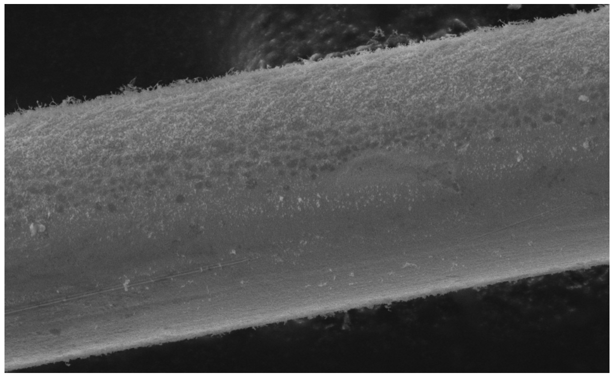

Figure 7.20: SEM inspection of the aged bicell wire.

applied to the cathodes and the strips, while the voltage of the wires was scanned in values ranging from 3250V to 3900V before the irradiation and from 3250V to 3800V after the irradiation with steps of 50V. Comparing the curves after and before the irradiation of each wire, there are noticeable differences only in the slope parts, while the efficiency plateau with a constant value $> 98\%$ from 3550 to 3900V remains unaltered within the errors. It is also clear from the figure 7.23, where it has been computed the loss of efficiency of the Bicell 2 after the irradiation with respect to the efficiency obtained when it was built.

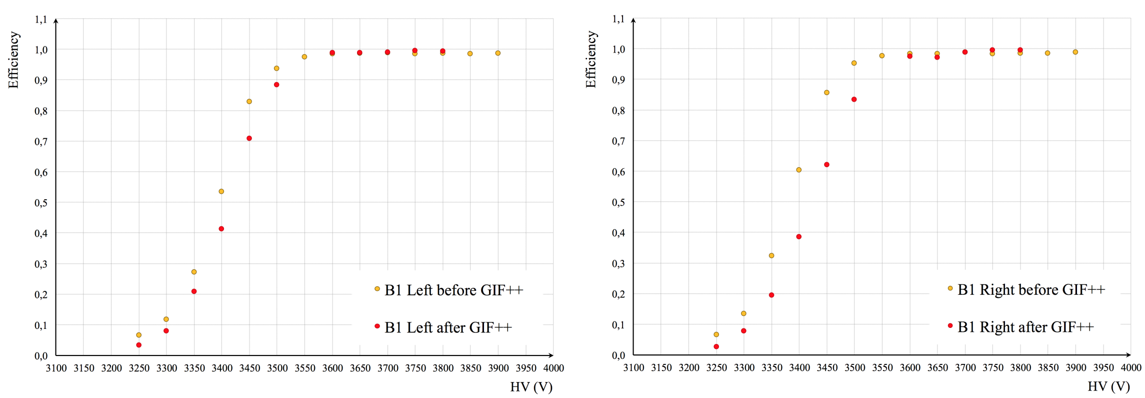


(a) Wire "Left" (b) Wire "Right"

Figure 7.21: Efficiency of each wire of the Bicell 1 as a function of the wires HV

In figure 7.24 is presented a comparison among the curves of the average efficiency of two bicells before and after the irradiation and the efficiency of the MB3 chambers installed at

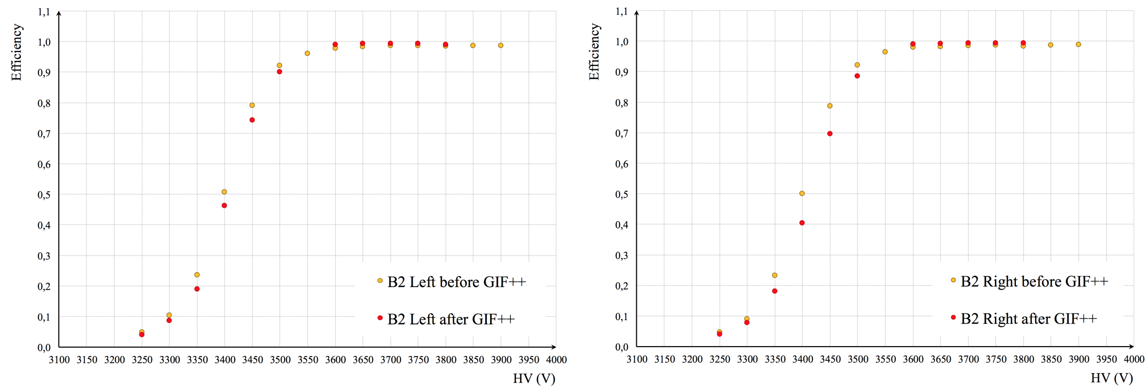


(a) Wire "Left" (b) Wire "Right"

Figure 7.22: Efficiency of each wire of the Bicell 2 as a function of the wires HV

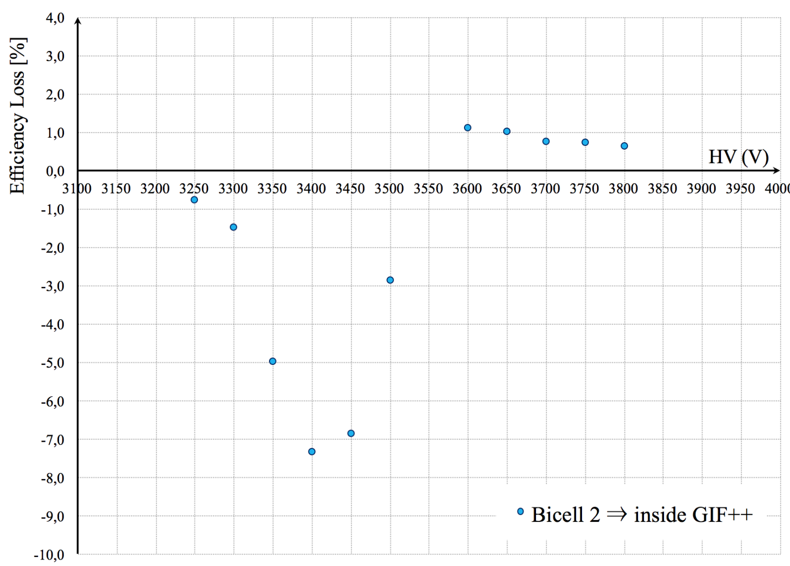


Figure 7.23: Efficiency loss of the Bicells 2 after the irradiation at GIF++ as a function of the wire HV

1326 LNL.

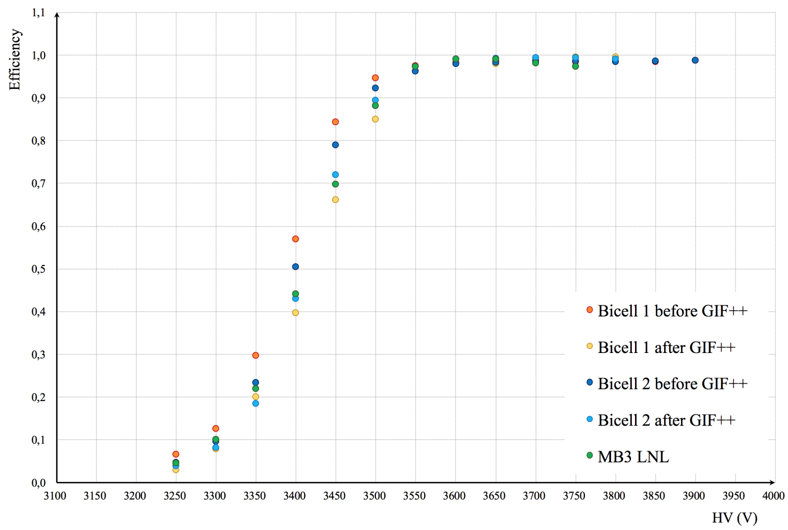


Figure 7.24: Comparison of the efficiency of bicells before and after the irradiation and of a layer of an MB3 chamber in Legnaro

## 7.5 Analysis of the cathode photo-peaks

One of the visible effect of aging on gas detectors is a lowering of the signal amplification as function of the integrated current. One of the ways to quantify the degradation of the performance of the wires is to study the number of events in the so-called cathode photo-peak.

The primary and secondary electrons created by the muon passing through the cells and ionizing the gas are amplified near the wire. During the avalanche effect, photons are produced and emitted in any direction. Electrons can be extracted from the surfaces of the cell by these photons and drift to the wire producing a secondary signal. The distributions of the time of the primary and secondary signals can be seen in the left and central plots of figure 7.25. The right plot has been obtained subtracting the time of the secondary signal by the time of the first one; it shows the approximate absolute drift time of the secondary electrons.

The most precise way to analyze signals from photo-extracted electrons is to identify the peak produced by electrons extracted from the cathodes, whose drift time is constant, $\sim 400$ $ns$ (which is also the width of the timebox of the first hit left plot of figure 7.25).

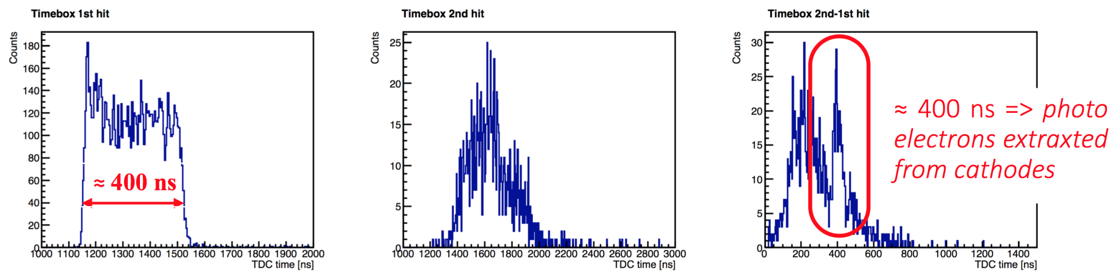


Figure 7.25: Timeboxes of the one of the cells of the bicells.

Data were taken at different wire voltages, keeping the strips and cathodes voltages at standard values. For each data sample, the number of signals in the cathode photo-peak was considered and normalized by the number of signals in the first hit timebox. The results obtained analyzing the cathode photo-peaks of the two bicells before and after the irradiation at GIF++ are shown in figure 7.26.

Comparing the normalized number of events in the cathode photo-peaks before and after theirradiation, no particular trend is found, neither for the Bicell 1 which was not irradiated in the GIF++, nor for the Bicell 2 which was inside the bunker (figure 7.27).

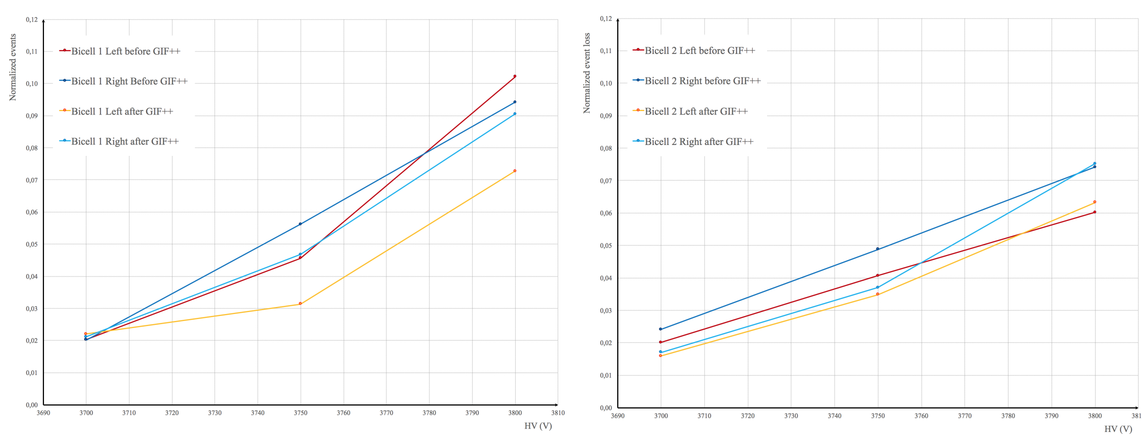


(a) Bicell 1 $\Longrightarrow$ outside GIF++ (b) Bicell 2 $\Longrightarrow$ inside GIF++

Figure 7.26: Cathode photo-peak events normalized by the number of the first hits for each wire of the two bicells as a function of the wire HV

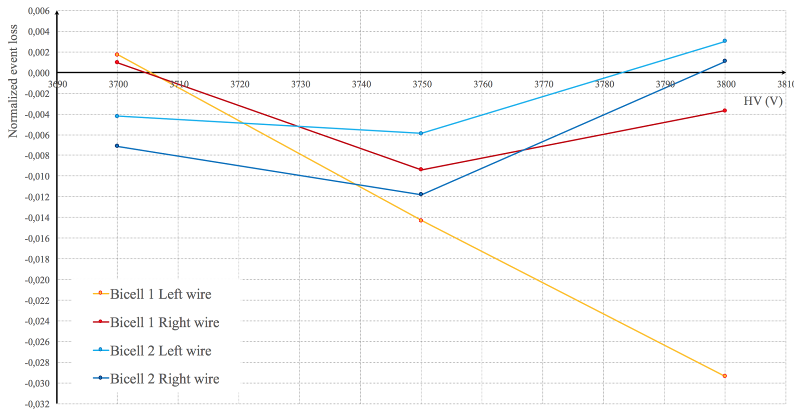


Figure 7.27: Normalized events loss in the cathode photo-peak after the irradiation as a function of the wire HV

## 7.6 Conclusions

The main results of these preliminary studies with the bicells are:

- The DT cell itself, without HV and FE electronics, contains some outgassing materials which contribute to aging effects that are not compatible with the ones of the first spare chamber used. Probably some dramatic unknown phenomena happened to the MB1 chamber during the first irradiation at GIF++
- Bicells can be used as monitor detectors for aging effects and indeed some studies are still going on at the GIF++ with the four bicells produced in the spring 2017
- Studies for specific outgassing materials are being performed in Legnaro and at GIF++

Up to the summer 2017, when the thesis has been redacted, the solution adopted to mitigate the aging effects on the DT chambers installed in the CMS detector at P5 are:

- The High Voltage has been lowered from the nominal 3600V value to 3550V, remaining in the plateau of the efficiency, but reducing the amplification and consequently the integrated charge
- The gas flux for the different wheels and for the MB1 of the external wheels has been separated

- A specific detector will be used as a monitor for the gas quality [33]
- Future periodic HV scans will be performed to obtain the efficiency curve

# Acknowledgements

First of all, I want to express my gratitude to my supervisor Prof. Anna Teresa Meneguzzo and to my co-supervisor Dr. Luigi Guiducci for helping me to learn how to behave and to use all the necessary tools to take part actively to the research. Besides, I would like to thank my Summer Student supervisor Dr. Andrea Triossi and Dr. Carlo Battilana for the patient teaching and the fundamental advices they gave me during the thesis. Last but not least, many thanks to my family and to all my friends for having supported and encouraged me during these five years of university.

# Appendices

# Appendix A

# Preliminary tests of the bicells

The first step was to check the gas tightness. After the use of a gas leak tester, in order to identify the leakages, the bicells were dipped in a vessel filled with water. Checking the gas pressure and inspecting the water, issues were found: some in the junction between the aluminium cover and the walls of the cells and some, smaller ones, caused by the electronics cables passthrough. The problems were fixed with more Araldite, aluminium tape and DP190. The final gas tightness of the bicells was checked with a differential barometer: the pressure inside the cells decreased 1 $mbar$ per hour.

Next step was the checks of the electronics. The bicells have been positioned inside the muon chamber telescope available at LNL. The LNL CMS telescope is composed by two MB3 muon chambers ($237.9cm \times 302.1cm \times 27cm$); the upper chamber is named ch1, the lower one ch2. As reported in [34], in the DT chamber the signals of all channels are hardware analyzed and a "DT Local Trigger segment" signal is output with position, direction and reference time of the crossing ionizing particles (within 25 $ns$ steps). The information of the ch1 and ch2, related to the muon events triggered by ch1 (within a window of the track direction), was recorded and analyzed offline [35] for the tracks reconstruction. Usual rates for the trigger was 330 $counts/sec$; the rate of each wire of the bicells was instead $\sim 6$ $counts/sec$, in agreement with their surface ratio.

The output signal of the four wires of the bicells were plugged into four unused channels of the ch1 readout (#0,#9 and #6,#15) and data were registered in the same data files of the chambers wires.

Voltages of cell's electrodes (bicells and chambers) were set as follow: $+3700$ V for anode wires (wire HV setting at the LNL atmospheric pressure), $+1800$ V for strips and $-1200$

V for cathodes. The pressure inside the cells was set to $\sim 10$ *mbar* above atmospheric pressure ($\sim 1010$ *mbar*).

After a preliminary data collection and analysis, comparing the rate of the second hit events of each cell[1], it was noticed that one cell detected half of the signals. Inspecting the reading electronics and checking the connections between wires and MAD and fixing the spark gap tinning, the problem was solved.

## A.1 Position of the bicells with respect to ch2

The efficiency of the bicells has been computed using the tracks identified in the ch2 chamber extrapolated to the bicells plane. The distance z of this plane from the z=0 plane of the ch2 chamber has been extracted selecting cosmic muon events with recorded TDC data in the channels associated to the two bicells wires. Selected only the ones with an angle less than 0.1 *rad* in $\phi$ and $\theta$ plane in ch2, the position in $\phi$ and $\theta$ of such tracks in the two chambers is shown in figure A.1; the distributions are broader in ch1 than in ch2 because of the slope acceptance and accuracy and the z distance of the two chambers planes ($\sim 2.5$ *m* for ch1 and $\sim 0.15$ *m* for ch2) from the bicell plane. The width of the $\phi$ distribution of the selected tracks in ch2 corresponds to the width of two near cells (about 8.4 *cm*).

To find the exact z-position of the bicells plane from the z=0 plane of ch2, given an arbitrary (but reasonable) z of the bicell plane, the extrapolated track position has been considered with respect to the bicells recorded TDC time[2]. In figure A.2, the distributions relative to different z of the bicells plane are shown. In the plot, for each z position considered, the TDC times have been shifted with common specific delays (values are reported in the legend). The spread of the distributions changes as function of the z of the bicells plane and reaches a minimum around z = 15.1 *cm*. The ranges of the TDC in the different positions show the drift time range; the "V" shape reflects the symmetry of the TDC time in the left and right position of the cell with respect to the wire. An accurate quantitative evaluation of the z of bicell plane has been obtained with a minimization process of the residuals of the extrapolated position at a given z plane with respect to the the linear fit in each branch of the 'W' distributions.

[1] This method is very sensitive and fast for identifying differences due to gas, electronic cross talk or noise.

[2] The extrapolated position is calculated as follows: $pos_{extrap} = pos_{ch2} + \phi slope_{ch2} * z$

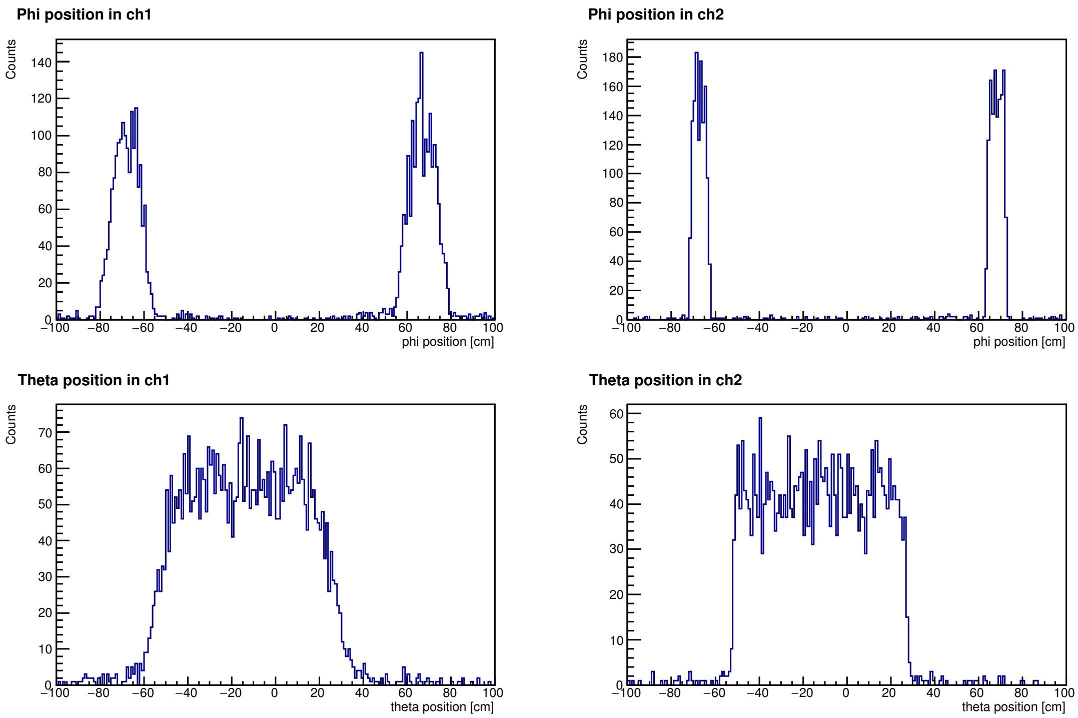


Figure A.1: $\phi$ and $\theta$ positions of the bicells: events detected in ch1 and ch2.

| | Bicell #0, #9 | Bicell #6, #15 |
|---|---|---|
| Position $\phi$ [cm] | $64 \div 72.2$ | $-71.4 \div -63$ |
| Position $\theta$ [cm] | $-52.5 \div 37.5$ | $-52.5 \div 37.5$ |
| Position z [cm] | 15.1 | 15.1 |

## A.2 Timeboxes

The "timebox" is the distribution of the TDC times recorded by a wire of a bicell or chamber. In figure A.3 timeboxes of cell #0, upper plots, and the ones of the ch2 cells, bottom plots, are compared. The bicells and the chambers have the almost same threshold (20 mV for the bicells and 30 mV for the chambers) and the same HV setting (see subsection 7.4.2).

From the "timebox" of the bicell there is almost null noise since no signals are recorded before a starting time and this starting time is almost equal in all the four wire channels.

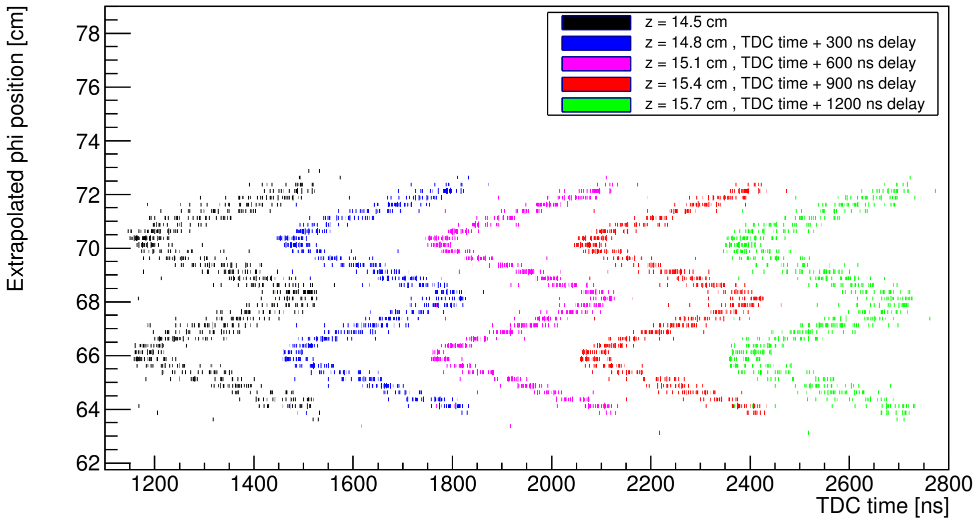


Figure A.2: $\phi$ position of the Ch2 track extrapolated at different z planes vs TDC time: cells $\#0$,$\#9$.

Considering the distribution of the first signal recorded, first hit timebox, the distribution is almost flat in a range of $\sim 400\ ns$ wide. It corresponds to the times of the signal of electrons produced by primary and secondary ionization of cosmic rays in the gas. Due to the fact that cosmic rays are uniformly distributed in space, the first hit timebox is expected to be flat within the full drift time distribution if the effective drift velocity is uniform. The peak after the rising edge of the distribution is due to $\delta$-electrons emitted by the ionizing track; $\delta$-electrons have 50% probability to arrive earlier than the ionization electrons. The rising edge ($\sim 25\ ns$) takes into account of the track time jitter with respect to trigger (ch1 trigger), being the trigger generated with a coincidence of a 40 $MHz$ clock.

Second hit candidate are $\delta$-electrons or electrons extracted from the cell's wall by photons produced in the electron multiplication near the wire. In the timebox $2^{nd} - 1^{st}$, the peak at $\sim 400\ ns$ identifies the photoelectrons extracted from the cathode strips. The FE dead-time of $\sim 60\ ns$ is visible in the "timebox" of the second hit.

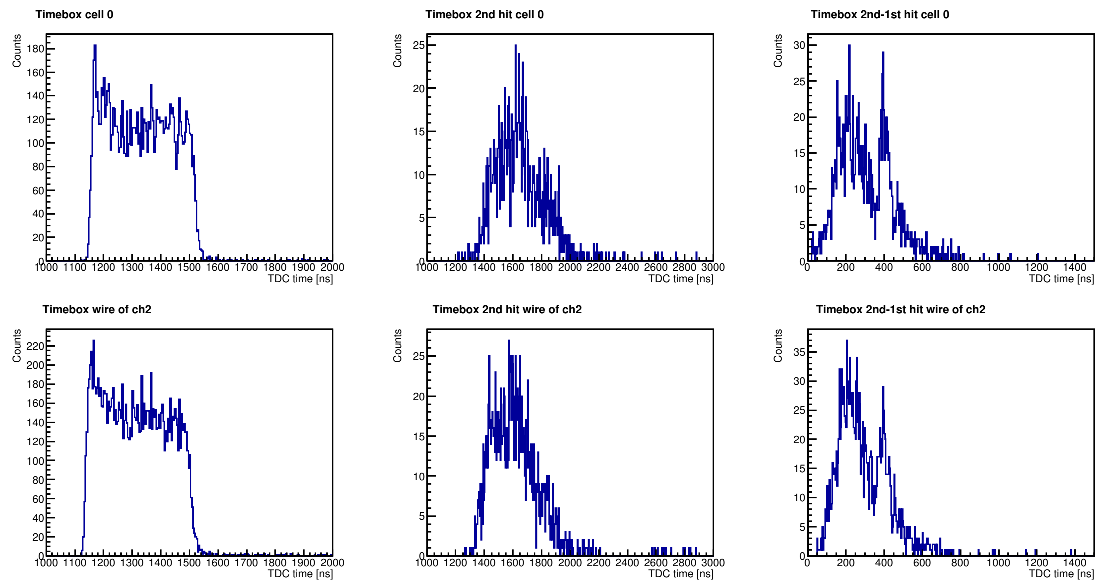


Figure A.3: Timeboxes of the cell #0 of the bicells and one of the cell of ch2.

## A.3 Parameters

The parameters for computing the position of the track in the plane of the bicell from the TDC times are the electrons drift velocity in the gas, the $\phi$-position of the wires and the TDC offset time ($t_{Trig}$). The tracks which cross a cell just on the wire position have almost null drift space, then their TDC recorded time is assumed as zero of the TDC time, or $t_{Trig}$. As can be seen it corresponds to the starting point of the rising of the timebox distribution. These parameters can all be extracted from the distribution of the " Extrapolated position vs TDC time", fitting with a linear regression each branch of the 'W' distribution and considering the weights of each extrapolated position. The absolute value of the slope represents the drift velocity of electrons ($v_{drift}$), the intersection between two near straight lines (belonging to the same 'V') gives the $\phi$-position of the wires (y-axis) and the $t_{Trig}$ (x-axis).
Alternatively, it is possible to obtain the $t_{Trig}$ time from the equation A.1, given $v_{drift}$ and $\phi-$position of the wires, plotting it as an histogram and fitting the distribution with a gaussian.

$$t_{Trig} = t_{TDC} + \left| \frac{\phi\, pos_{extrap} - \phi\, pos_{wire}}{v_{drift}} \right| \tag{A.1}$$

The weighted average of the drift velocity is $v_{drift} = 0.0056\ cm/ns$; the results of the parameters $\phi$-position of the wires and trigger time obtained are presented in table A.1.

| | $t_{Trig}$ centroid [ns] | $t_{Trig}$ FWHM [ns] | Wire's $\phi-$ position [cm] |
|---|---|---|---|
| #6 wire | 1158.5 | 25.05 | $-69.23$ |
| #15 wire | 1156.7 | 25.32 | $-65.03$ |
| #0 wire | 1150.8.5 | 24.89 | 66.03 |
| #9 wire | 1150.6 | 24.73 | 70.23 |

Table A.1: Parameters of the cells.

## A.4 Linearity in detecting positions of the tracks

To verify the linearity of the position with respect to the recorded drift time in the cells, the distribution 'reconstructed position by ch2 vs detected position by the bicells' has been used. An example is given in figure A.4, selecting the cell #15. Detected position is calculated with the equation: $pos_{det} = pos_{wire} \pm (t_{TDC} - t_{Trig})$. The distribution is as expected.

## A.5 Bicells position detection resolution

The spatial resolution is defined as the $\sigma$ of the distribution of the difference between the ch2 extrapolated position and the position measured by the bicells(figure A.5). Some systematic errors must be taken into account. One is the the track time delay with respect to the trigger time (which defines the start of the TDC): as reported previously the trigger time have a granularity of 25 $ns$, while the cosmic muon tracks have a uniform time distribution. This track delay, event by event is computed within the track reconstruction both in ch1 and in ch2. This track time correction can be applied to the bicells TDC time. Another systematic error is the delay due to the propagation of the signal along the wire. The position along the wire is computed extrapolating the reconstructed $\theta$ track in the ch2 and using the propagation velocity of 24 $cm/ns$ as a function of the track's distance from the front-end electronics [36],[10]. Moreover, the obtained new $\sigma$ is the convolution of the real resolution of the bicells, the error of the reconstructed position in ch2 extrapolated to the plane of the

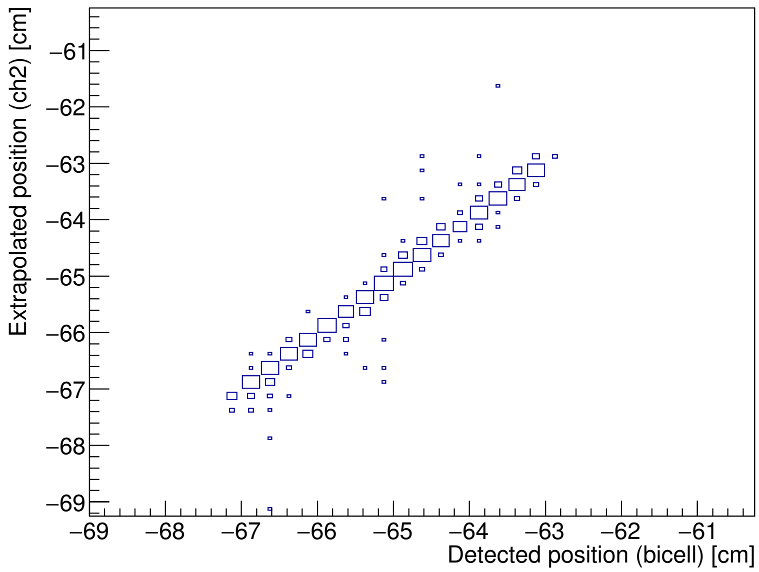


Figure A.4: Linearity of the cell #15.

bicells and the one due to multiple scattering, since cosmic muon have low momentum (see equation A.2).

$$\sigma_{tot}^2 = \sigma_{resol}^2 + \sigma_{extrap}^2 + \sigma_{mult-scatt}^2 \tag{A.2}$$

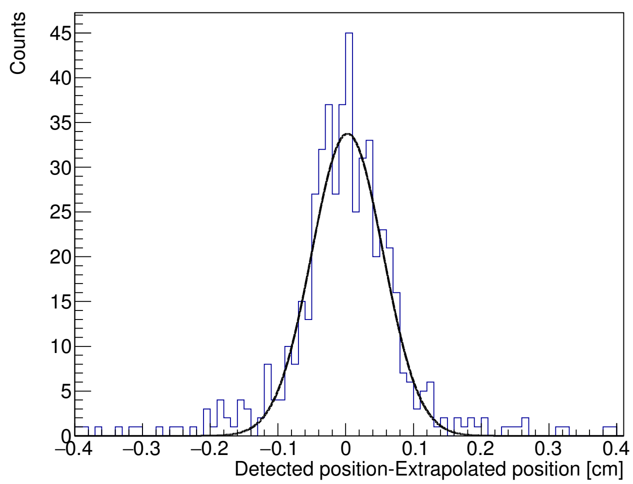


$$\sigma_{tot} = 400\mu m$$

$$\sqrt{\sigma^2_{extrap} + \sigma^2_{multi-scatt}} = 250\mu m$$

$$\sigma_{resol} = 300\mu m$$

Figure A.5: Spatial resolution of the bicells, example plot of cell #15.

# Bibliography


[1] **CERN-PH-EP/2012-220, 2013/01/29**, The CMS Collaboration, *"Observation of a new boson at a mass of 125 GeV with the CMS experiment at the LHC"*.

[2] **Springer Theses Recognizing Outstanding Ph.D. Research, 2016**, M. C. Thomas, *"Beyond Standard Model Collider Phenomenology of Higgs Physics and Supersymmetry"*.

[3] **Doctoral dissertation, Université catholique de Louvain, 2010**, L. Quertenmont, *"Search for Heavy Stable Charged Particles with the CMS detector at the LHC"*.

[4] **PhysicsReports 438(2007)1–63**, M. Fairbairn et al., *"Stable massive particles at colliders"*.

[5] **CERN Summer Student Lectures 2017**, V. Kain CERN BE-OP, *"Introduction to Accelerator Physics"*.

[6] **CERN Summer Student Lectures 2017**, M. Lamont, *"LHC status"*.

[7] **CERN/LHCC 2006-001, 2 February 2006**, The CMS Collaboration, *"CMS Physics, Technical Design Report, Volume I: Detector Performance and Software"*.

[8] **Nucl.Instrum.Meth. A480 (2002) 658-669, 12 pp**, M. Aguilar-Benitez et al., *" Construction and test of the final CMS Barrel Drift Tube Muon Chamber prototype"*.

[9] **2017 JINST 12 C01032**, G. Masetti on behalf of the CMS collaboration, *"Status and future prospects of the Muon Drift Tubes System of CMS"*.

[10] **JINST 5 (2010) T03015 arXiv:0911.4855 [physics.ins-det] CMS-CFT-09-012 CMS Paper CFT-09-012**, The CMS Collaboration, *"Performance of the CMS Drift Tube Chambers with Cosmic Rays"*.

[11] **JINST 8 (2013) P11002 DOI: 10.1088/1748-0221/8/11/P11002**, The CMS Collaboration, *"The performance of the CMS muon detector in proton-proton collisions at $\sqrt{s} = 7$ TeV at the LHC"*.

[12] **Nuclear Instruments and Methods in Physics Research A 845 (2017) 616–620**, F . Gasparini et al., *"Upgrade of the CMS muon trigger system in the barrel region"*.

[13] **CERN-PH-EP/2012-173 2013/03/21**, The CMS Collaboration, *"Performance of CMS muon reconstruction in pp collision events at $\sqrt{s}$=7 TeV"*.

[14] **Under publication in JINST**, The CMS Collaboration, *"Performance of CMS muon reconstruction in pp collision events at $\sqrt{s}$=13 TeV"*.

[15] **https://twiki.cern.ch/twiki/bin/view/CMSPublic/MuonDPGResults#Links_to_approv**

[16] **Nucl. Instrum. and Meth. A 579 (2007), 951-960, DOI: 10.1016**, M. Aldaya et al. *"Results of the first integration test of the CMS drift tubes muon trigger"*.

[17] **CMS Detector Performance Summary CMS-DP-2015-026, 2015**, The CMS Collaboration, *"Validation of the mean-timer algorithm for DT local reconstruction and muon time measurement, using* 2012 *data"*.

[18] **Nuclear Instruments and Methods in Physics Research A 336 (1993) 91-97**, The CMS Collaboration, *"Bunch crossing identification at LHC using a mean-timer technique"*.

[19] **Nuclear Instruments and Methods in Physics Research A 845 (2017) 616–620**, D. Rabady et al., *"Upgrade of the CMS muon trigger system in the barrel region"*.

[20] **2017 JINST 12 C01095**, A. Triossi et al., *"The CMS Barrel Muon trigger upgrade"*.

[21] **2016 JINST 11 C03038**, J. Ero et al., *"The CMS Level-1Trigger Barrel Track Finder"*.

[22] **https://twiki.cern.ch/twiki/bin/view/CMSPublic/DTDPGResults201120154**

[23] **CMS AN-16-201**, A. Ackert et al., *"Searches for Heavy Stable Charged Particles with 2016 Data"*.

[24] **https://twiki.cern.ch/twiki/bin/viewauth/CMS/GlassRPC**

[25] **Computer Physics Communications, 2001**, F. Sauli, *"Fundamental understanding of aging processes: review of the workshop results"*.

[26] **International workshop on Aging Phenomena in Gaseous Detectors, 2-5/10/2001, DESY, Hamburg**, M. Capeans, *"Materials and gases: Lessons for detectors and gas systems"*.

[27] **DT Gif++ meeting 18-Aug-2016**, D.Dattola, D.Fasanella, F.Gasparini, F.Gonella, A.T.Meneguzzo, J.Pazzini, I.Redondo, *"GIF++ STUDIES"*.

[28] **ECFA High Luminosity LHC Experiments Workshop, 22/10/2014**, G. Graziani, *"Wire detectors @ HL-LHC"*.

[29] **LHC electronics workshop,2001**, F. Gonella and M. Pegoraro, *"The MAD", a Full Custom ASIC for the CMS Barrel Muon Chambers Front End Electronics"*.

[30] **CMS NOTE 2007/000**, M. Benettoni, F. Gasparini, F. Gonella, A. Meneguzzo, S. Vanini, G. Zumerle, G. Bonomi, *"CMS DT Chambers: Optimized Measurement of Cosmic Rays Crossing Time in absence of Magnetic Field"*.

[31] **http://www.spectrumtechniques.com/radioisotopes2.htm**

[32] **Lectures given in the Academic Training Programme of CERN 1975-1976, CERN-77-09**, F. Sauli, *"Principles of operation of multiwire proportional and drift chambers"*.

[33] **CMS NOTE -2017/007**, Georg Altenhöfer et al., *"The drift velocity monitoring system of the CMS barrel muon chambers"*.

[34] **JINST 5 (2010) T03003 CMS-CFT-09-022 DOI: 10.1088/1748-0221/5/03/T03003**, The CMS Collaboration, *"Performance of the CMS Drift Tube Local Trigger with Cosmic Rays"*.

[35] **CERN-PH-EP/2012-173 2013/03/21**, The CMS Collaboration, *"Performance of CMS muon reconstruction in pp collision events at* $\sqrt{s} = 7\ TeV$*"*.

[36] **JINST 5 (2010) T03016 CMS-CFT-09-023**, The CMS Collaboration, *"Calibration of the CMS Drift Tube Chambers and Measurement of the Drift Velocity with Cosmic Rays"*.

[37] **Chin. Phys. C, 2015**, Particle Data Group, *"The Review of Particle Physics"*.